Poly-phase structural evolution of the northeastern Alxa Block, China: Constraining the Paleozoic-Recent history of the southern Central Asian Orogenic Belt

Jin Zhang[1], Cunningham Dickson[2], Junfeng Qu[1], Beihang Zhang[1], Jinyi Li[1], Heng Zhao[1], Pengfei Niu[1], Jie Hui[3], Long Yun[4], Shuo Zhao[1], Rongguo Zheng[1], Yiping Zhang[5]

1. Key Laboratory of Deep-Earth Dynamics of Ministry of Natural Resources, Institute of Geology, Chinese Academy of Geological Sciences, Beijing, 100037, China; 2. Department of Environmental Earth Science, Eastern Connecticut State University, Willimantic, CT, USA; 3. University of Chinese Academy of Sciences, Beijing, 100049, China; 4. Beijing Research Institute of Uranium Geology, Beijing, 100029, China; 5. Chinese Academy of Geological Sciences, Beijing, 100037, China

Abstract: The Alxa Block is a significant tectonic unit in the middle part of the southern Central Asian Orogenic Belt that was affected by multiple Paleozoic and Meso-Cenozoic deformation events. In this study, the results from detailed mapping and structural analysis coupled with new U-Pb zircon ages indicate that the northeastern Alxa Block has experienced ten deformation events since the late Paleozoic. Four separate structural domains are identified in the study area, and these domains contain intrusive and structural crosscutting relationships that allow the complex deformational history to be determined. Each deformation phase can be related to regional tectonic events associated with the consolidation of Central Asia's crust and subsequent intraplate reactivation. The first three events are tied to convergence between the Alxa Block, the North China and the Yangtze Cratons prior to and during closure of the Paleo-Asian Ocean in the Mid-Late Permian. Subsequently, sinistral displacement occurred between the Alxa Block and the North China Craton during the Triassic. Since the late Mesozoic, reactivation of the northeastern Alxa Block occurred repeatedly as an intraplate response to the subduction of the Paleo-Pacific Plate, the closure of the Mongol-Okhotsk Ocean, the collision between the Qiangtang and Lhasa blocks and the later collision between India and Eurasia. The Alxa Block provides a superb case study of how continental interior regions that evolve from plate boundaries to intraplate settings may remain susceptible to reactivation in different kinematic modes in response to distant plate margin-derived forces and internal gravitational forces that evolve through time.

Keywords: Alxa Block, Central Asian Orogenic Belt, polyphase deformation, intraplate tectonism, crustal reactivation.

1. Introduction

The Central Asian Orogenic Belt (CAOB) is one of the largest and longest-lived accretionary orogens in the world, with terrane amalgamation and seaway closure occurring from the Neoproterozoic to the end-Paleozoic – early Mesozoic (Şengör et al., 1993, 2018; Şengör and Natal'in, 1996; John et al., 2004; Windley et al., 2007; Wilhem et al., 2012; Kröner et al., 2014; Xiao et al., 2010, 2015). More precise timing of final closure of the Paleo-Asian Ocean between the converging plates or terranes within the CAOB remains debated, especially in the central-eastern CAOB where conflicting geological and geochronological evidence suggest final consolidation occurred during the Devonian, Permian, or Triassic (Xiao et al., 2003; Feng et al., 2013; Song et al., 2015; Zheng et al., 2014; Miao et al., 2008; Jian et al., 2010; Xu et al., 2013; Zhao et al., 2013; Shi et al., 2016; Liu et al., 2017). Following CAOB terrane amalgamation and consolidation of Central Asia's continental interior, the central-eastern CAOB was affected by multiple tectonic events during the Mesozoic and Cenozoic within an intraplate setting (De Grave et al., 2007; Guy et al., 2014; Gillespie et al., 2017). Understanding the polyphase deformational evolution of the central-eastern CAOB raises important questions that bear on the tectonic evolution of all continents such as: 1) Why did the central-eastern CAOB continue to deform after final terrane consolidation and what lithospheric factors controlled the spatial distribution and kinematics of deformation? 2) Is the intraplate reactivation of the central-eastern CAOB typical of accretionary orogens? 3) If non-cratonized continental interiors remain susceptible to episodic crustal reactivation, then which fault systems are most likely to be reactivated and pose a potential earthquake threat?

In this study, we examine the tectonic evolution of the Alxa Block, a major component of the central part of southern CAOB and a key region connecting the Beishan, Qilian Shan, North China Craton (NCC) and CAOB terrane collage in northern China and southern Mongolia (Fig. 1). Due to the relatively inaccessible, hyper-arid and remote, rugged terrain, the Alxa Block, has received limited previous tectonic study. Important questions concerning the exact number of separate deformation events that have affected the region, the timing and kinematics of these events and their spatial distribution have remained unresolved (Shi et al., 2016; Zhang et al., 2013; Wang et al., 1994a; Feng et al., 2013; Zheng et al., 2014; Song et al., 2018a). Importantly, the Alxa Block can be regarded as a core tectonic domain within the huge Meso-Cenozoic intraplate deformation field of central and eastern Asia, because it connects the North Tibetan-Qilian Shan-Hexi Corridor deforming belts with the Gobi Corridor region of Mongolia and the modern rift basins of the western Ordos region (Fig. 1; Molnar and Tapponnier, 1975; Yue and Liu, 1999; Lamb et al., 1999; Yue et al., 2001a; Darby and

Ritts, 2002; Darby et al., 2005; Webb and Johnson, 2006; Cunningham et al., 2003, 2016; Cunningham, 2013, 2017; Zhang et al., 1998, 2009, 2010, 2013a, 2015, 2016a; Yuan and Yang, 2015; Yu et al., 2016; Heumann et al., 2014, 2018). Correlating the multiple intraplate deformation events recorded in exposed bedrock in the Alxa region with the deformation record in surrounding regions and connecting these events to distant plate margin or intraplate driving forces is a fundamental problem in central Asian tectonics research.

Therefore, to better understand the geological evolution of the Alxa Block and what it reveals about the tectonic evolution of surrounding regions in Central Asia, we conducted a 5-year field-based interdisciplinary investigation in the Langshan region(Figs. 1, 2), which contains the largest area of Precambrian basement and cover lithologies in the Alxa Block (Fig. 1). The key results relevant to the questions posed above are discussed and summarized in this report.

2. Regional geological setting

Traditionally, the Alxa Block has been treated as a part of the NCC (Fig. 1; Huang, 1945). It is debated whether the Alxa Block (also known as the Yinshan Block) collided with the Ordos Block during the late Paleoproterozoic (1.9-1.8 Ga; Zhao et al., 2005) or was an independent block that docked with the NCC during the early Paleozoic or early Mesozoic (Zhang et al., 2013a, 2016a; Dan et al., 2012, 2014b, 2016; Yuan and Yang, 2015; Zhao et al., 2018). Late Archean metamorphic basement is reported from the western Alxa Block (Zhang et al., 2013b), and Neoproterozoic intrusions occur in the central and eastern Alxa Block (Geng and Zhou, 2010; Dan et al., 2014a).

In the early Paleozoic, the NCC and/or the Alxa Block were continental blocks within the Paleo-Asian Ocean that gradually converged with Beishan terrane and the central and eastern Mongolian terrane collage (Badarch et al., 2002; Xiao et al., 2015). The Alxa Block connects the NCC and Tarim Craton, occupying a transitional region between the Paleo-Asian Ocean regime to the north and the Tethyan regime to the south (Fig. 1; Zhang et al., 2008; Xiao et al., 2009, 2010). During the Permian, the central-eastern CAOB consolidated via ocean closure along the Engeerwusu zone that bounds the north side of the Alxa Block (Wang et al., 1994a, 1994b, 1998; Wu et al., 1998; Zheng et al., 2014). The zone is composed of imbricated top-to-the-north thrust sheets comprising intensely sheared ultramafic, mafic and deep-sea sedimentary assemblages with block-in-matrix characteristics typical of ophiolitic assemblages. Gabbro samples from the ophiolite yield a zircon U-Pb age of 278 Ma (Zheng et al., 2014).

Multiple Mesozoic deformation events in the Langshan region have been previously reported, including a major Triassic northeast-trending ductile shearing event in the Langshan-Bayanwulashan region, a Triassic top-to-the-south thrusting event in the

Weiningbeishan (Fig. 1, Zhang et al., 2013a, 2014); a Late Jurassic top-to-the-east thrusting event in the Helanshan (Fig. 2; Darby and Ritts, 2002), and Early Cretaceous low-angle detachment faulting in the Langshan (Darby and Ritts, 2007; Zhang et al., 2013a, 2014). Previous studies have suggested that the reactivation of the Alxa Block by the Indo-Eurasian collision in the Cenozoic occurred largely within fault systems and thrust-bounded ranges along the Hexi Corridor in the southwestern Alxa Block (Yue and Liu, 1999; Yue et al., 2001a, 2001b; Darby et al., 2005; Cunningham et al., 2016). Furthermore, the possibility that the Altyn Tagh Fault system extends into and through the Alxa Block into southeastern Mongolia is a subject of continued debate (Yue and Liou, 1999; Yue et al., 2001a, 2001b; Darby et al., 2005; Webb and Johnson, 2006).

A series of Cenozoic rift basins is developed along the western and northwestern margin of the Ordos Block and the eastern margin of the Alxa Block (Figs. 1, 2), such as the Hetao Basin to the north and the Yinchuan Basin to the south (Zhang et al., 1997). Seismic data indicate that the basement of the Hetao Basin is approximately 10-13 km below surface (TRGAFSOM, SSB, 1988). Elevated footwall block mountain ranges bounded by high-angle normal faults are developed along the western basin margins; the bounding normal faults are seismically active. Historical earthquakes have occurred along all of the active rift systems that surround the Ordos Plateau, including at least 15 recorded M≥5 events in the Langshan and Helanshan regions (Fig. 1; Liu et al., 2016; Rao et al., 2016). GPS data from the NE Alxa Block region reveal very low extensional fault slip rates along the Langshan frontal fault on the order of 0.5 - 1.6 mm/yr (Fig. 1b; Zhao et al., 2017). Previous geological mapping in the NE Alxa Block indicates that a phase of Miocene strike-slip faulting and thrust faulting preceded Late Cenozoic-Recent rift basin development (Zhang et al., 2014).

3. Bedrock geology of the northeastern Alxa Block study area

The study region is located in the northeastern Alxa Block (Figs. 1, 2, 3). In addition to regional fieldwork and compilation of previous published work, a 420 km^2 region of the central-eastern Langshan was mapped in detail at a scale of 1:25,000 to document the poly-deformational history of the exposed bedrock terrain (Fig. 3). Tectonic structures in the eastern Alxa Block mainly strike north-northeast or nearly north-south. Paleoproterozoic to Mesoproterozoic metamorphic rocks crop out in the Langshan (i.e., the Diebusige Complex) and the Bayanwulashan (i.e., the Bayanwulashan Group), and record metamorphic events during 1.9-1.8 Ga (Dan et al., 2012). The Diebusige Complex experienced two metamorphic events at 1.93-1.89 Ga and 1.84-1.79 Ga, and is considered the oldest basement of the Alxa Block (Dan et al., 2012). The complex was metamorphosed to amphibolite and granulite grade and contains garnet-bearing amphibolite, migmatized amphibolite, diopsidic marble, garnet quartzite, magnetite-

bearing quartzite and sillimanite-biotite gneiss (Shen et al., 2005).

The Mesoproterozoic Baoyintu Group is distributed in the northwestern corner of the region shown in Fig. 3 and is composed of mica-quartz schist and quartzite, most of the group has experienced extensive ductile deformation. The deposition of the Baoyintu Group sedimentary protoliths occurred after ca. 1400 Ma, as constrained by detrital zircon dating (Sun et al., 2013). The provenance of the Baoyintu Group is likely to be the North China Craton (NCC) and the basement rocks that the Baoyintu Group was deposited upon were either part of the NCC (Shen et al., 2004; Sun et al., 2013) or a separate and independent terrane in the Paleo-Asian Ocean during the Paleozoic (i.e., the Baoyintu Block; Zhang and Su, 2002; Zhang, 2004).

The Neoproterozoic Langshan Group is a low-grade metamorphic assemblage divided into four formations comprising meta-sediments and interbedded meta-volcanic rocks whose protoliths were likely deposited in a rift succession (Fig. 3; Hu et al., 2014). The lowermost First Formation mainly consists of gray to dark gray phyllite, thin-bedded conglomerates, thin-bedded marlstone, marble, and quartzose sandstone. The Second Formation is mainly composed of brown or gray marble, gray thin- to medium-bedded quartzose sandstone and chlorite-quartz schist. The Third Formation consists of thick-bedded gray to dark gray quartzite and medium- to thick-bedded quartzose sandstone interlayered with marble. The Fourth Formation is composed of brown-yellow mica-bearing calcareous sandstone, carbonaceous slate, marble, and extensively deformed mica-quartz schist and mylonite. Among these formations, the Second and Third Formations are weakly metamorphosed, and many sedimentary structures are preserved that can be used to determine the original way-up direction of the strata. Many dikes of granite, diorite and gabbro crosscut or are intruded parallel to layers of the Langshan Group. The Langshan Group was folded into a series of southeast-verging anticlines and synclines with recumbent folds developed in the southeastern part of the study region.

Numerous intrusions are present in the study region (Figs. 2, 3, 4), most of which are late Paleozoic monzonitic granite, biotite granite, syeno-granite, diorite and Neoproterozoic gabbro. Mesozoic and Cenozoic non-marine strata that are separated by unconformities also occur in the mapped region including Middle Jurassic thin-bedded black carbonaceous shale and thick-bedded conglomerates, Lower Cretaceous brick-red thick-bedded conglomerates, and Eocene orange thick-bedded pebbly sandstones. Late Paleozoic pillow lavas occur in one location (red star in Fig. 3).

4. Field methods

Geological mapping using a World-View 2 satellite image (0.5 m resolution) as a base map was carried out at a scale of 1:25,000 between 2012 and 2017 (Figs. 3, 4). The Langshan mapping area is approximately 400 km^2 in area and contains elevations

ranging from 1000-1700 m with moderate-low relief (typically <300 m). Prior to fieldwork, preliminary satellite image interpretation was carried out to identify contacts, traces of folded layers, fold hinges, fault/fabric/bedding strike and dip directions, and visible fault offsets. Because of limited desert vegetation and excellent rock exposure, the image analysis provided a wealth of preliminary geological information that was subsequently field validated.

Data on the orientations of fault planes (dip direction and angle), slickenlines (trend and plunge) and bedding/foliations/lineations were collected at approximately 3000 locations in the map area (Fig.3). Where possible, multiple measurements of structural elements were collected at each location. Fault data were collected from nearly 1000 widely distributed locations (Fig. 5). Fault kinematics in most rocks at these locations (where discernible) are indicated by calcite slickenfiber steps, small Riedel shear fractures and small-scale offset of bedding, veins or dikes. Fault data were used to calculate fault plane solutions where slickenlines were recorded (Fig. 5). The analysis of the fault-slip data in this study was performed according to the kinematic approach of Marrett and Allmendinger (1990) to assess incremental shortening and extension directions (P- and T-axes). FaultKin (5.2) and Stereonet 8 (R. W. Allmendinger of Cornell University) were used to calculate the fault plane solutions and to visualize and analyze the structural data, respectively.

5. Lithotectonic domains and main lithologies

Based on different bedrock lithologies and deformation styles, the study region can be divided into four structural domains from northwest to southeast that are separated by four regional northeast-southwest-trending faults and shear zones (Fig. 4). The domains are 1) the Neoproterozoic Langshan Group (Domain I), 2) Permian biotite granite (Domain II), 3) the Paleoproterozoic Diebusige Complex (Domain III), and 4) Carboniferous monzonitic granite (Domain IV).

In Domain I, the outcropping rocks are mainly the Neoproterozoic Langshan Group, Neoproterozoic diorite intrusions and late Paleozoic muscovite granite, with a small patch of the Mesoproterozoic Baoyintu Group in the northwesternmost region. The main structures in Domain I are nearly northeast-southwest-striking isoclinal folds, whose trends locally shift to the northeast and east (Fig. 4b, d).

In Domain II, the main rocks are Permian biotite granite, granitic dikes, Triassic syenogranite, and a narrow belt of the First Formation of the Langshan Group in the southeastern part of the domain (Fig. 3). There are also small bodies of diorite and pillow lava intruded by Permian biotite granite (Fig. 3). The main structural trend in this domain is northeast-southwest.

The Diebusige Complex in Domain III has experienced a multistage tectonic history,

including deformation during Paleoproterozoic metamorphism. The complex includes garnet-bearing amphibolite, marble, garnet quartzite, and magnetite-bearing quartzite. The metamorphic basement rocks are also intruded by porphyritic K-feldspar granite, Carboniferous granite and Permian granite. In the southeastern part of the domain, marble, thin-bedded conglomerates and siltstones of the First Formation of the Langshan Group are present and strike northeast-southwest. An Early Cretaceous supra-detachment basin is located in the northeastern part of Domain III (Fig. 3). Generally, the Diebusige Complex is deformed by three sets of folds that are northeast-southwest-trending, east-west-trending and nearly north-south-trending folds (Fig. 4f). The east-west-trending folds are Precambrian in age and precede the tectonic history described in this study (Niu et al., 2019). A major northeast-southwest-striking ductile shear zone is also present in the complex (Fig. 3).

The main rock in Domain IV is Carboniferous monzonitic granite, with U-Pb zircon ages between 348±4 and 329±1.5 Ma (Zhang et al., 2013a; Dan et al., 2016). Small patches of unconformably overlying Oligocene red conglomerates of the Wulanbulage Formation are distributed on hilltops. The main structures in this domain are a wide, penetratively developed, northeast-southwest-trending ductile shear zone and younger, similarly oriented strike-slip faults. To the southeast, a top-to-the-northwest thrust and the active high-angle normal fault array that defines the SE Langshan (Dabashan) range front are also prominent structures (Fig. 3).

6. Zircon U-Pb geochronology

To further constrain the timing of Paleozoic-early Mesozoic deformation in the Langshan region, zircon U-Pb dating was performed on key lithologies. Samples were collected mainly from various deformed and undeformed diorite, gabbro and granite dikes intruding the Langshan Group and Diebusige Complex; granitic/felsic mylonite; and undeformed granite plutons. Sample locations, lithologies, geological units, and dating methods are listed in Table 1.

6.1 Laser ablation inductively coupled plasma mass spectrometry (LA-ICP-MS) U-Pb zircon dating

Zircons were separated from all samples by conventional magnetic and density techniques and were then mounted in epoxy resin and polished to expose the grain centers. The samples were prepared for U-Pb dating after photographing them under reflected and transmitted light. Cathodoluminescence (CL) imaging was performed at Beijing GeoAnalysis Co., Ltd., to observe the origin and structure of the zircons and to select target points for U-Pb dating.

Laser ablation inductively coupled plasma mass spectrometry (LA-ICP-MS) zircon U-

Pb analyses were performed at three laboratories during different periods. Most samples were dated at the Key Laboratory of Mineral Resources Evaluation in Northeast Asia, Ministry of Land and Resources of China, Jilin University. Sample LS-16-3 was analyzed at the State Key Laboratory for Mineral Deposits Research, Nanjing University. The respective dating methods of the two laboratories are described in Data Repository 1.

Concordia ages and diagrams were obtained using the ISOPLOT program (Ludwig, 2003). The isotopic ratios and element concentrations of zircons were calculated using Glitter. The common lead correction was made using the LA-ICP-MS common lead correction (ver. 3.15) following the method of Andersen et al. (2002). Most zircon grains are euhedral to subhedral and show oscillatory zoning with high Th/U ratios (0.10–2.95; STable 1, openly available in figshare at http://doi.org/10.6084/m9.figshare.12127176), suggesting a magmatic origin. The ages are the weighted means at the 95% confidence level (Ludwig, 2003). The analytical data are presented on U-Pb concordia plots and weighted mean age diagrams with 1σ errors, except sample LS-16-3, which is presented with 2σ errors. The concordia and weighted mean age diagrams are shown in Fig. 6, and the representative images of the dated zircons from all samples are shown in SFig. 1.

6.2 Analytical results

The U-Pb zircon ages are presented below according to the domains from which the samples were collected. The sample locations, lithologies, geological domains, dated minerals, dating methods and LA-ICP-MS zircon U-Pb dating results are listed in Table 1.

Domain I

In this domain, four samples were dated (LS-16-3, D1148-1, D15719-2, and D15109-1). A total of 90 analyses of zircon grains from the granite that intrudes the Second Formation of the Langshan Group (sample LS-16-3) yielded an age of 258 ± 1.6 Ma (mean square weighted deviation, MSWD = 0.31, n = 46) and inherited zircon ages ranging from 2402 Ma to 350 Ma.

Thirty analyses of zircon grains from the diorite that intrudes the Third Formation of the Langshan Group (sample D1148-1) yielded an age of 840 ± 8 Ma (MSWD = 0.018, n = 18; Fig. 6) and inherited zircon ages ranging from 1887 Ma to 1152 Ma. Twenty-eight analyses of zircon grains from the granitic mylonite sample D15719-2 yielded an age of 258.9±1.3 Ma (MSWD = 0.23, n=22; Fig. 6), with 5 grains yielding ages of ca. 270 Ma. Twenty-eight analyses of zircon grains from the boudinaged sample D15109-1 yielded an age of 257.6±1.1 Ma (MSWD = 0.44, n=23; Fig. 6).

Domain II

In this domain, four samples were dated (D15090-1, D15040-1, D15041-1, and D15729-1). Twenty-eight analyses of zircon grains from diorite sample D15090-1 yielded an age of 263.7±1.9 Ma (MSWD = 0.037, n=28; Fig. 6). Twenty-eight analyses of zircon grains from the folded granite sample D15040-1 yielded an age of 259.4±1.3 Ma

(MSWD=1.06, n=20; Fig. 6). Seven grains yielded younger ages of ca. 241 Ma. A total of 28 analyses of zircon grains from the granite sample D15041-1 yielded an age of 257.8±1.5 Ma (MSWD = 0.54, n=21; Fig. 6). Twenty-eight analyses of zircon grains from the granite sample D15729-1 yielded an age of 272.2±2.3 Ma (MSWD = 0.022, n=11; Fig. 6), with a few grains yielding ages from 257-242 Ma.

Domain III

Two samples were dated from this domain (LS-14-3 and D15739-1). Thirty analyses of zircon grains from the K-feldspar granite sample LS-14-3 yielded an age of 1834±17 Ma (MSWD = 3, n=29; Fig. 6). A total of 28 analyses of zircon grains from the granite sample D15739-1 yielded an age of 259.6±1.3 Ma (MSWD = 0.017, n=25; Fig. 6).

Domain IV

One sample was dated from this domain (LS-14-1). Sixty analyses of zircon grains from the granite sample LS-14-1 were analyzed and yielded 2 groups of concordant ages of 344.7±1.2 Ma (MSWD = 0.3, n=38; Fig. 6) and 331.3±2.2 Ma (MSWD = 0.3, n=9).

7. Sequence of deformation events

Structural mapping of the southwestern Langshan region indicates that all four litho-tectonic domains experienced multiphase deformation histories (Figs. 2-5). Different sets of bedrock structures, kinematic indicators and cross-cutting relationships in the four domains allow for determination of the deformation sequence. In this study, the deformation sequence in Domain I is referred to as **DI-n** (n=1, 2, 3…, from oldest to youngest); the sequence in Domain II is referred to as **DII-n**; the sequence in Domain III during and since the Paleozoic is referred to as **DIII-n**; and the sequence in Domain IV is referred to as **DIV-n**. Because the Paleoproterozoic deformation in Domain III precedes the tectonic history of CAOB assembly, we refer to the Precambrian deformation of the Diebusige Complex in Domain III as **DIII-PЄ** and omit it from further analysis in this study. Not every deformation event is represented in each of the four domains because some lithologies formed after specific events. For example, the oldest identified deformation event in one domain may actually represent the third deformation event (D3) in the wider region.

The first deformation - D1

The earliest distinguishable event in the study region is represented by only a north-south-trending ductile shear zone with variable thickness (up to 250 m-wide) involving thick-bedded quartzite in the Fourth Formation of the Langshan Group and the mica-quartz schist and muscovite quartzite of the Baoyintu Group in the northwestern part of Domain I (**D_{I-1}**; Figs. 3, 4). The shear zone forms the boundary between the Langshan and Baoyintu Groups. The quartzite in the shear zone is extensively mylonitized. Well-

developed foliation generally strikes north-northeast with subhorizontal quartz stretching lineations plunging shallowly to the northeast or southwest (Fig. 4a). The foliation is mainly defined by fine-grained muscovite. Quartz in the mylonite exhibits undulose extinction and dynamic recrystallization (Fig. 7B). The occurrence of grain boundary migration (GBM) in the quartz indicates a temperature during deformation of more than 500°C.

Asymmetric σ-type quartz vein boudins (Fig. 7A) and abundant muscovite fish (Fig. 7B) indicate sinistral shearing. However, due to later folding, the mylonite has been deformed into southeast-vergent overturned isoclinal folds. Typical muscovite S-C fabrics were also observed in overturned limbs of the folded shear zone, but indicate dextral shear, indicating that bulk sinistral ductile shearing (**Dl-1**) occurred before the folding of the Langshan Group (**Dl-2**). The overturned folds of the mylonite are rotated so that their axial surfaces are near-horizontal and this is likely due to overthrusting of the Mesoproterozoic Baoyintu Group to the NW. Gong et al. (2017) reported two muscovite $^{40}Ar/^{39}Ar$ plateau ages (379±4 Ma and 356±2 Ma) from this shear zone and interpreted these ages as the ages of the ductile shearing.

The second deformation - D2

Evidence of the second deformation event occurs in Domains I, II and III. In Domain I, northeast-southwest-trending isoclinal folds of various scales developed in every formation of the Langshan Group (**Dl-2**; Figs. 3, 8). The bedding of the Langshan Group dips towards 290-340° at 40-78° and comprises the upright limb of a large northeast-southwest-trending overturned anticline verging to the southeast (Fig. 3). The π axis of the folded bedding of the Langshan Group indicates a larger, first-order northeast-plunging fold (Fig. 4g). Most of the fold core and the overturned limb are cut by a younger east-west-trending dextral strike-slip fault in the eastern part of Domain I (Fig. 3). The outcropping minor folds mostly verge to the southeast, with axial surfaces dipping to the northwest (Fig. 8B). Fold-transecting cleavage is parallel to the axial surface, especially in the Fourth Formation (Fig. 8C). Bedding in the Fourth Formation succession is transposed into bedding-parallel cleavage, except in the thick-bedded quartzite. Slickenlines perpendicular to fold hinges were observed on both limbs of minor folds due to flexural slip and cleavages caused by interlayer shearing also developed (Fig. 8D). We dated diorite and granite dikes that intrude the Langshan Group to constrain the deformation age of the Langshan Group (Table 1). Among the samples, LS-16-3 was collected from a folded granite dike (Fig. 8A, 258 ±1 Ma), and D1148-1 was collected from diorite that intrudes the Langshan Group (840±8 Ma). The D2 event therefore postdates 258 ±1 Ma.

Northeast-southwest-trending D2 folds with horizontal hinges also deform the First

Formation in Domain II (**DII-1**). Thin bedding-parallel granite dikes intruding the Langshan Group are also folded (Fig. 9A), and the deformation style is similar to that of granite dikes intruding in the Langshan Group in Domain I (Fig. 8A). The thin-bedded sandstones of the Second Formation of the Langshan Group were folded into a series of southeast-verging isoclinal to recumbent anticlines and synclines (Fig. 9B). All these deformation characteristics are similar to those of the Langshan Group in Domain I. Sample D15040-1 was collected from the granite dikes for zircon U-Pb dating and yielded an age of 259 Ma (Fig. 9A, Table 1).

In Domain III, D2 deformation is the first recognized tectonic event and is characterized by southeast-verging isoclinal folds of the First Formation in the southeastern part (**DIII-1**). The deformation shows some ductile characteristics: quartz stretching lineations and stretched pebbles on or near bedding planes plunge northwest (Fig. 10B), perpendicular to the fold hinges and crenulation lineations of the Langshan Group (Fig. 10A). In contrast, the interbedded thick-bedded limestone was folded into a recumbent anticline verging southeast (Fig. 3). Many small southeast-verging folds are also present in thin-layered sandstones, limestone and siltstone (Figs. 10C-D); In the XZ plane of the strain ellipsoid (i.e., parallel to the lineations and perpendicular to the foliations), asymmetric structures/fabrics indicate that these folds are flexural-slip folds, similar to the folds in the Langshan Group in Domain I. Note that the refolded fold shown in Fig. 10A may have formed in a continuous process or in two different deformation events. Because the fold in Fig. 10A is located close to the Triassic ductile shear zone in Domain IV, the two-stage deformation interpretation is preferred here. The similarities in geometry and deformation style of the D2 folds in the Langshan Group in Domain I, II and III (**DI-2**, **DII-1**, **DIII-1**) suggest that they formed during the same period.

The third deformation - D3

Evidence of the D3 deformation occurs in Domains I, II and III. A large east-west-trending valley is developed along the boundary between Domains I and II (Fig. 11A). Ductile dextral shearing occurred between the Permian biotite granite in Domain II (**DII-2**; inset in Fig. 11A, ca. 260 Ma) and the Langshan Group **(DI-3)** of Domain I (Figs. 3, 11). The granite and Langshan Group quartzites adjacent to the contact are mylonitized (inset in Fig. 11A). In the mylonitized granitie, quartz stretching lineations are well developed (inset in Fig. 11A), and S-C fabrics and δ-type feldspar porphyroclasts (Fig. 11B) indicate dextral shearing. The thickness of the mylonitized granite changes along strike from tens of meters to 300 m. The east-west-trending mylonitic foliations are well developed and steep-to-vertical. Quartz in the mylonite exhibits strong undulose extinction and dynamically recrystallized grain aggregates. The occurrence of grain boundary bulging in quartz indicates a deformation temperature of more than 300°C. The zircon U-Pb age of the coarse-grained biotite granite in this domain is ca. 270-260 Ma (e.g., D15719-2 in Fig.

11A and D610-1 in Table 1). In addition, the entire zone is cut by younger north-south-trending sinistral faults (Fig. 3).

East-west-trending shear zones with the same characteristics are also distributed in the interior of Domains I, II and III. These east-west-trending shear zones are cut by the northeast-southwest-striking sinistral ductile shear zone in the eastern part of Domain III (Fig. 3). The deformed rocks are mainly mylonitized granite dikes intruding into the Diebusige Complex and feature well-developed quartz stretching lineations. Quartz in the mylonite is dynamically recrystallized, and locally, ultramylonite is present. In the XZ plane of the strain ellipsoid, asymmetric structures indicate dextral shearing (Fig. 12A). All ductile dextral faults are cut by the northeast-southwest-trending sinistral ductile shear zone in Domain IV and by nearly north-south-trending sinistral faults in Domain II (Fig. 3). Therefore, we argue that the deformation in the Diebusige Complex **(DIII-$_2$)** was coeval with the **DI-$_3$** event in Domain I and the **DII-$_2$** event in Domain II.

The fourth deformation - D4

Evidence of the D4 deformation occurs in Domains I, III and IV. In Domain I, the main folds in the Langshan Group strike northeast-southwest (Figs. 3, 4b). However, in the northwestern part of the mapped region, the main folds are refolded, forming northwest-southeast-trending open folds plunging to the northwest (**DI-$_4$**; Fig. 4b). Bedding-parallel dikes that intrude the Langshan Group typically exhibit cleavage associated with the first folding event (Fig. 13A), that is also folded. Younger crenulation cleavage fold hinges generally trend SE or NW with steep dip angles (Fig. 13B), parallel to the large northwest-southeast-trending open folds of the Langshan Group. Because the folds of this stage are mainly distributed in the northwestern part of the study region and are cut by brittle Jurassic thrusts, we assign them to a fourth deformation event.

In Domain III, D4 deformation is represented by ductile deformation of the magnetite-rich quartzite and amphibolite gneiss of the Diebusige Complex and the Paleozoic granite that intrudes this complex **(DIII-$_3$)**. The deformation of this stage occurred in the region close to the northwestern margin of the Diebusige Complex where felsic mylonites (comprising both granite and quartzite) developed (Fig. 3). Quartz stretching lineations are well developed and mostly plunge to the northeast (Fig. 14A). Typical overturned antiforms of the diopside-rich marble and magnetite-bearing quartzite of the Diebusige Complex are present and mainly strike northeast-southwest (Figs. 4f, 14B). In the southeastern part of Domain III, the Diebusige Complex was folded into a series of northwest-trending closed antiforms or synforms (Fig. 14C), which are parallel to quartz stretching lineations (Fig. 14C). The mylonitic foliations mainly strike northeast-southeast, but northwest-southeast-striking foliations are also present (Fig. 14A).

To the southeast of Domain III, ductile deformation of the Diebusige Complex is more intense; several northeast-southwest-trending ductile sinistral shear zones occur in the

Carboniferous granite (LS-14-1, 344.7±1.2 Ma, Table 1) and felsic dikes that intrude the Diebusige Complex. The mylonitic foliations are parallel to the gneissosity of the Diebusige Complex. D3 deformation is the first recognized structural event in Domain IV and is represented by well-developed and widely distributed ductile sinistral fabrics in the Carboniferous granite (**DIV-1**). This wide zone of shear narrows to the northeast to approximately 800 m wide, whereas it is nearly 3 km wide at the southwestern end (Fig. 3). Quartz stretching lineations mainly plunge to the northeast (Fig. 4i), and the mylonitic foliation dominantly strikes northeast-southwest (Fig. 4i). The foliation is folded, resulting in many antiforms of various scales plunging to the northeast (Figs. 3, 4j), which are covered by the Oligocene Wulanbulage Formation. The hinges of the antiforms are parallel to the quartz stretching lineations (Fig. 4i). Various kinematic indicators, such as S-C fabrics, σ-type structures, mica fish, and asymmetric folds, all indicate sinistral shearing on both limbs of the folds; all the above phenomena indicate that these antiforms are likely A-type folds. Previously, Zhang et al. (2013a) concluded that the sinistral shearing occurred at ca. 250±2 Ma based on a $^{40}Ar/^{39}Ar$ plateau age for muscovite that grew during mylonitization.

The fifth deformation - D5

Evidence of the fifth deformation can be found in Domains I, II and III. In Domain I, a large top-to-the-southeast thrust and linked back-thrust occurs between the Second and Third Formations of the Langshan Group (**DI-5**) (Figs. 3, 15A). The main fault dips 30-60° to the northwest and exhibits a duplex geometry. It is localized along medium- to thick-bedded carbonaceous shale at the top of the Second Formation (Fig. 15A). The thrust stack contains many minor thrust faults and displaces the Third Formation of the Langshan Group and bedding-parallel diorite intrusions (Fig. 15A). A sample from the deformed granite (D1151-1) yielded no good weighted mean age; however, the youngest single-grained zircon ages are approximately 250-240 Ma (Fig. 15A).

Similar to Domain I, Domain II also features a set of top-to-the-southeast thrust faults (**DII-3**) (Fig. 3). Generally, the cores of these thrust faults are 2-5 m wide. The fault throw is unknown due to the lack of markers in the granite. The thrust faults cut the Permian granite (D15729-1, 272.2±2.3 Ma) and diorite (D15090-1, 263.7±1.9 Ma, Table 1). Along these thrust faults, some outcrops of deformed pillow lava occur. Previous zircon U-Pb dating of the pillow lavas indicates that they formed in the Late Permian (ca. 255 Ma; Zhang et al., 2013c).

In Domain III, a series of similar thrust faults developed in the Diebusige Complex **(DIII-4)** (Figs. 3, 15B-C). These faults cut overlying Middle Jurassic conglomerates and carbonaceous shale (Fig. 15B-C) and resulted in the formation of an anticline composed of Middle Jurassic strata. In addition, regionally extensive contractional deformation is documented elsewhere along the western and northern Ordos Block margins during the

Late Jurassic (Darby et al., 2001; Darby and Ritts, 2002). Therefore, we suggest that these top-to-the-southeast thrust faults most likely developed in the Late Jurassic.

In addition to the above brittle thrust faults, there are many east-west-trending brittle dextral strike-slip faults in Domains I, II, and III. Most of these strike-slip faults are superimposed on pre-existing east-west-trending ductile dextral shear zones, such as the boundary between Domains I and II (Fig. 11C), where the metamorphosed limestone and quartzose sandstones of the Langshan Group in the hanging wall are cut by many minor faults (Fig. 11C) that are parallel to the early mylonitic foliations (Fig. 11B). Fine-grained discolored fault breccias developed within the fault zone. The slickenlines on the fault plane are parallel to the quartz stretching lineations (Fig. 11B), which may indicate that brittle dextral faulting was a younger overprint on the ductile fabrics. These faults are cut by younger north-south-trending sinistral faults (Fig. 3). Younger, brittle dextral faults with similar orientations overprinting the granitic mylonites were also found in Domain III. The faults are usually planar and associated with pink or white fault breccias up to 1-2.5 m thick (Fig. 12B). These dextral faults are extensively developed in the western part of Domain III.

Some of the above east-west-trending brittle dextral strike-slip faults change into top-to-the-southeast thrust faults along strike, especially in the Permian granite in Domain III (Fig. 3). We conclude that these two sets of kinematically linked faults are coeval and formed in the Late Jurassic. The east-west-trending dextral brittle strike-slip faults are interpreted as lateral ramps for coeval top-to-the southeast thrust faults.

The sixth deformation - D6

Evidence of the D6 deformation only occurs in Domain III, where a small Early Cretaceous basin overlies crystalline basement (**DIII-5**) (Fig. 3). A low-angle detachment fault defines the boundary between the basin units and the underlying Paleoproterozoic Diebusige Complex and Carboniferous granites (Fig. 3). The basin contains red, thick-bedded, NW-dipping conglomerates with poorly sorted angular pebbles. The Lower Cretaceous conglomerates are unconformably covered by Oligocene conglomerates of the Wulanbulage Formation. The basal low-angle detachment fault (Fig. 16A) dips less than 30° to the southeast, and slickenlines on the fault plane indicate ESE directed extension (Fig. 16A). The thickness of the fault breccias varies from 10 cm to more than 3 m. Generally, the fault breccias are green or light red (Fig. 16A). The attitude of the Lower Cretaceous strata and their relationship with the low-angle detachment fault indicates that the basin is a supra-detachment depocenter controlled by the detachment fault (Fig. 3). The westward dip of the Lower Cretaceous strata near the fault is consistent with syn-tectonic rotation of the hanging wall during SE-directed slip on the detachment fault (Fig. 4a-a') (**DIII-5**). The detachment fault and Lower Cretaceous strata are separated from the overlying horizontal Oligocene Wulanbulage Formation by an angular unconformity (Fig.

16B).

The seventh deformation - D7

The seventh deformation occurred in all domains. In Domain I, the main structures of this stage are brittle north-south-trending strike-slip faults that cut the entire study area (Figs. 3, 17). These faults cut not only the early folds, thrust faults, and mylonitic fabrics in the Langshan Group but also the Neoproterozoic diorite and late Paleozoic gabbro and granite that intrude the Langshan Group. Narrow linear canyons and valleys and thick fault breccias are common along the faults (*e.g.*, **DI-6**) (Fig. 17). The strike-slip displacement of individual faults ranges from 50 to 100 m, gradually decreasing along fault strike to the north. These faults commonly cut southwards into the Permian biotite granite in Domain II (**DII-4**; Fig. 3), where they exhibit greater displacement (200-250 m) and become wider. In addition, in Domain II, some faults of this type transition into top-to-the-southeast thrust faults at their southern ends, and some of these faults are late Jurassic, **DII-3** generation thrusts. Thick light-colored fault breccias (5-20 m) occur at fault junctions.

In the mapped region, the cumulative displacement of these north-south-trending sinistral faults may be up to 10 km, if an approximately east-west-striking boundary originally separated the Permian granite to the south in Domain II and the Langshan Group to the north in Domain I. The fault plane solutions for these faults indicate that the shortening direction was oriented northwest-southeast when they formed (Figs. 5, 17A). Because these faults cut the Permian granite (ca. 260 Ma) in the south, they must have formed after ca. 260 Ma. These north-south-trending faults also cut Late Jurassic thrust faults but are cut by Cenozoic thrust faults in the Diebusige Basin in Domain III (Fig. 3).

In Domain II, in addition to north-south-trending strike-slip faults, D7 deformation is also represented by brittle deformation along the boundary fault between the Permian granite in Domain II and the Diebusige Complex in Domain III **(DIII-6)**. The fault zone forms a long valley and spring line up to approximately 220 m wide with thick fault breccias and local pseudotachylite (Fig. 18A). Sinistral strike-slip faults within the fault zone strike northeast-southwest, dip to the northwest at 60-80° (Fig. 18A) and are superimposed on mylonites developed in the Diebusige Complex. These brittle sinistral faults were subsequently overprinted by later dextral strike-slip faults, which cut an early Cretaceous diabase dike (Fig. 18B).

In Domain III, two other vertical northeast-southwest-striking sinistral strike-slip faults (Figs. 19A, 19C) developed farther to the southeast; one is the boundary fault between Domains III and IV (Fig. 19A), and the other cuts Lower Cretaceous sediments in the Diebusige Basin (Figs. 3, 19C). Nearly horizontal slickenlines are present on the fault planes, and the faults are nearly vertical or dip to the northwest at 60-80° (Fig. 19B). In

the western part of Domain III, many north-south-trending faults cut the east-west-trending dextral faults in the complex and extend southwards into the Carboniferous monzonitic granite of Domain IV (Fig. 3). The north-south-trending faults do not cut the northeast-southwest-trending sinistral strike-slip faults between Domains II and III (Fig. 3), and the northeast-southwest-trending sinistral strike-slip faults disappear to the southwest (Fig. 3), where they are replaced by north-south-striking sinistral strike-slip faults (Fig. 4). In addition, the northeast-southwest-trending sinistral fault between Domains III and IV limits the nearly north-south-trending sinistral faults (Fig. 3), but no crosscutting relationships between these two classes of faults have been found. Therefore, we suggest that these two fault sets may be coeval. The northeast-southwest-trending faults also cut the Lower Cretaceous sediments in the Diebusige Basin in Domain III (Fig. 19C), and a north-south-trending sinistral fault cutting Lower Cretaceous rocksoccurs in northeastern Domain III (Fig. 17C); hence, these faults must have formed during or after the Late Cretaceous and are assigned to D7. In addition, Darby and Ritts (2002, 2007) reported similar Late Cretaceous north-south-trending sinistral strike-slip faults to the north and south of the mapped region that also cut Lower Cretaceous sediments, but are cut by Cenozoic structures.

In Domain IV, many similar northeast-southwest-trending sinistral strike-slip faults developed in the granitic mylonite **(DIV-2)** (Figs. 3, 4). These faults are very clear in satellite images and dip 70-80° to the northwest or southeast and have fault breccia thicknesses of 0.5 to 3 m. The boundary between the Diebusige Complex and the Carboniferous granite is one of these brittle sinistral faults (Fig. 3). All these faults are parallel to the mylonitic foliation in the Carboniferous granite and Diebusige Complex, indicating that their formation and orientation were strongly influenced by the inherited basement fabric.

The eighth deformation - D8

The eighth deformation occurred in Domains II, III and IV. In Domain II, D8 deformation occurred along the boundary fault between Domains II and III (**DII-5**). This fault has a history of multiple phases of activity. In addition to sinistral strike-slip movements, later dextral oblique normal faulting also occurred. The fault cuts Early Cretaceous diabase dikes (Fig. 18B), and many minor P and R shear fractures are developed in the fault breccias. The fault plane solution indicates approximately horizontal north-northeast/south-southwest extension (Figs. 5, 18B), which is similar to the dextral oblique normal faults with the same attitudes in Domains III and IV. Because dextral fault offsets the Early Cretaceous diabase, it must have occurred after the Early Cretaceous. Additionally, in Domains III and IV, faults with the same attitudes present a similar 2-phase kinematic history between early sinistral (**DIII-6**) and later dextral shearing **(DIII-7)**.

In Domain IV, in the mylonitic granite, several dextral strike-slip faults are present and are all superimposed on earlier sinistral faults **(DIV-3;** inset in Fig. 20A). These faults were later covered by red conglomerate of the Oligocene Wulanbulage Formation, indicating that their development occurred before the Oligocene (Fig. 20B). The Wulanbulage Formation onlaps westwards, and its unsorted and angular pebbles indicate an alluvial origin with clasts derived from the underlying granitic mylonite. This indicates that the southeastern Langshan range (i.e., the Dabashan) was exhumed and eroded during the early Cenozoic. Apatite fission track (AFT) dating indicates that the activation of the dextral faults may have occurred at 60-40 Ma (Cui et al., 2018). Therefore, the northeast-southwest-trending dextral faults in Domain IV may be coeval with the dextral faults with similar attitudes in Domain III and were likely formed in the early Cenozoic; therefore, they are assigned to D8.

The ninth deformation - D9

The ninth deformation occurred in Domains III and IV. In the southeastern part of Domain III, a set of thrust faults dips to the southeast towards the Hetao Basin (**DIII-8**). These faults cut the overlying Oligocene conglomerates of the Wulanbulage Formation (Figs. 3, 21) and thus developed after the Oligocene. The fault plane solutions of these thrust faults indicate northwest-southeast shortening (Figs. 5, 21).

In Domain IV, similar Cenozoic top-to-the-northwest thrust faults also developed in the southeastern part of Domain IV **(DIV-4)** (Figs. 22, 23A). The thrust fault hanging wall is mainly composed of undeformed Carboniferous monzonitic granite (344.7±1.2 Ma, sample LS-14-1, Table 1). However, the footwall consists of granitic mylonite and Oligocene Wulanbulage Formation conglomerates (Figs. 22A, 23A) and Lower Cretaceous conglomerates (Figs. 22B-C). In the northern part of Domain IV, the hanging wall has been eroded or disrupted by later high-angle normal faults, leaving only a layer of fault breccia approximately 1.5-3 m thick between the basement uplift and Cenozoic basin. The fault plane solutions of these thrust faults indicate northwest-southeast shortening (Figs. 5, 22A). In the northeastern corner of Domain IV, small klippes of Carboniferous granite overlie the granite mylonite. This fault thrusts Carboniferous granite over the Oligocene Wulanbulage Formation, and AFT dating of the Carboniferous granite in the study region also identified a cooling event that occurred at ca. 20 Ma (Cui et al., 2018), supporting the existence of a Miocene contractional event (uplift with concomitant erosion) in the Langshan region.

The tenth deformation - D10

The tenth deformation can be found both in Domains III and IV. In the southeastern part of Domain III, a Cenozoic high-angle (70-80°) west-dipping normal fault developed to the west of the Dabashan range (**DIII-9**; Fig. 19B). This fault strikes northeast with its fault plane parallel to the metamorphic fabrics of the Diebusige Complex and reactivated the

pre-existing northeast-southwest-trending faults (Fig. 19B). The normal fault cuts not only the Diebusige Complex, Carboniferous granite, and Lower Cretaceous conglomerates but also the Oligocene Wulanbulage Formation (Fig. 19B).

In Domain IV, a high-angle normal fault system defines the southeastern Langshan (Dabashan) range front **(DIV-5**; Fig. 23). The present southeastern slope of the range front is an impressive normal fault plane that strikes northeast-southwest, dips to the southeast at more than 75° and is parallel to the mylonitic foliation within the Carboniferous granite footwall. These range-bounding normal faults are still active, cut the Pleistocene lacustrine sediments of the Jilantai Formation and Holocene alluvium (Fig. 23B) and have controlled the development of the Hetao Basin to the SE. Relief across the mountain front locally exceeds 600 m, and considerable late Cenozoic throw on the range-bounding fault is required to account for the 10-13 km depth of the modern Hetao rift. The fault plane solutions of the range-bounding normal fault system indicate that the orientation of shortening is nearly east-west and the major normal faults are sinistral transtensional (Figs. 5, 23B).

8. Synthesis of tectonic history

8.1 Summary of deformation events and age constraints in the Langshan region

Many structures of various ages have formed in each domain in the mapped region. Because the ages of the rocks differ, different rocks or units underwent and recorded different deformation events. Several important deformation events since the Paleozoic are recorded in all domains in the study area. Based on the above field observations and new and published age data, a summary of major deformation events recorded in the Langshan region is provided in Table 2. Key structures and age constraints for each distinguished event and the interpreted tectonic driving force are also indicated.

The earliest deformation (**D1**) in the mapped region during the Paleozoic was the 379-356 Ma ductile deformation (**DI-1**) between the Langshan Group and the Baoyintu Group. The younger Carboniferous-Permian granites in Domains II and IV post-date **D1** deformation. The second deformation (**D2**) in the mapped region was the folding of the Langshan Group during the late Paleozoic to Early Triassic (**DI-2, DII-1** and **DIII-1**). Isoclinal folding of diorite and granite dikes indicates that this event occurred in the Late Permian. Similar deformation also occurred in the First Formation of the Langshan Group in Domain II (**DII-1**). The third deformation (**D3**) involved east-west-trending ductile dextral strike-slip shearing (**DI-3**, **DII-2** and **DIII-2**), which may have occurred at the end of the Permian-Early Triassic. The fourth deformation (**D4**) involved the Triassic northeast-southwest-striking ductile shearing (**DI-4**, **DIII-3** and **DIV-1**) and its related structures, such as the northwest-trending folds in the Langshan Group (**DI-4**). The deformation in this stage was intense and affected all domains, resulting in the basic structural framework of

682 the mapped region. The fifth deformation (**D5**) involved top-to-the-southeast thrusting
683 during the Late Jurassic (**DI-5**, **DII-3** and **DIII-4**). This deformation mainly occurred in
684 Domains I, II and III and is represented by nearly east-west-trending brittle dextral strike-
685 slip faults that likely served as lateral ramps for the coeval top-to-the-southeast thrust
686 faults that are mainly found along the boundary between Domains I and II and within
687 Domain III. The sixth deformation (**D6**) was the Early Cretaceous low-angle detachment
688 faulting and formation of the supra-detachment basin controlled by this fault, which
689 mainly developed in Domain III (**DIII-5**). The seventh deformation (**D7**) was the
690 development of a series of nearly north-south-trending sinistral strike-slip faults.
691 Additionally, northeast-southwest-striking sinistral strike-slip faults developed across the
692 entire map area during this stage (**DI-6**, **DII-4**, **DIII-6** and **DIV-2**). The structures associated
693 with this stage cut across many other bedrock structures and likely formed in the Late
694 Cretaceous. The eighth deformation (**D8**) was tectonic inversion of the early northeast-
695 southwest-trending sinistral strike-slip faults (**D7**) during the early Cenozoic (**DII-5**, **DIII-7**
696 and **DIV-3**). The ninth deformation (**D9**) mainly occurred in Domains III and IV and
697 involved a series of thrust faults that developed due to northwest-southeast compression
698 in the mid- to late Cenozoic (**DIII-8** and **DIV-4**). The youngest deformation event in the
699 mapped region (**D10**) was the active high-angle normal fault system bounding the
700 southeastern mountain front, which has unloaded and isostatically elevated the footwall
701 Dabashan block (**DIII-9** and **DIV-5**).
702
703 **8.2 Interaction between crustal blocks in the Paleo-Asian Ocean (D1; Fig. 24 A, B)**
704 The earliest identifiable Paleozoic deformation in the northeastern Alxa Block is the
705 northeast-trending ductile sinistral shearing between the Langshan Group and Baoyintu
706 Group. The shear zone consists of parallel felsic mylonite belts and was later deformed
707 into SE-vergent folds. Yuan and Yang (2015) proposed that the Alxa Block rotated
708 counterclockwise by 32° after the Early-Middle Triassic based on paleomagnetic studies
709 of Carboniferous and Permian sedimentary rocks, and this rotation would have reoriented
710 the mylonite belts from an original more E-W trend. Two muscovite $^{40}Ar/^{39}Ar$ plateau ages
711 (379±4 Ma and 356±2 Ma) for these ductile shear zones were obtained by Gong et al.
712 (2017) and are interpreted as the timing of mylonitization.
713 Late Paleozoic nearly east-west-oriented compression and north-south-trending
714 ductile thrust zones are interpreted from the Bayanwulashan in the eastern Alxa Block
715 (351 ±9 Ma, biotite $^{40}Ar/^{39}Ar$ plateau age, Zhang et al., 2013a) and the Xiangshan in the
716 southern part of the eastern block (locations in Fig. 1; Zhang et al., 2016a). East-west
717 compression in the late Paleozoic may have been the result of amalgamation of the NCC
718 and the Alxa Block or by pre-collision convergence between these blocks (Zhang et al.,
719 2013a, 2016a). Late Paleozoic east-west compression is also reported from

southwestern Mongolia, due to westward subduction of the Mongol-Okhotsk oceanic plate (Lehmann et al., 2010; Edel et al., 2014). It is speculated that the Late Paleozoic originally east-west-trending sinistral strike-slip shear zone in the NW mapped region may have been caused by east-west relative movements between the Baoyintu and Alxa blocks to the north and south.

The Alxa Block and the Mongol-Tuva Block have Neoproterozoic granites and are interpreted to have rifted from the Gondwanan continent during the early Paleozoic (Wang et al., 2001; Geng and Zhou, 2010; Dan et al., 2014a; Zhang et al., 2016b; Buslov et al., 2004; Zhang et al., 2014, 2016a; Yuan and Yang, 2015). During their northward drift from eastern Gondwana, these blocks, including the NCC, may have converged along an active plate boundary. However, most of this boundary is complexly overprinted or covered by Quaternary sediments. Thus, this interpretation is open to question, and more work is needed.

8.3 Closure of the Paleo-Asian Ocean (D2; Fig. 24 C, D)

The timing of the closure of the Paleo-Asian Ocean remains controversial. In the western segment of the CAOB, most studies suggest that closure occurred in the Late Devonian to Early Carboniferous (Charvet et al., 2007) or Late Carboniferous (Gao et al., 2009). In addition, most ophiolites in the western CAOB are dated as Ordovician-Devonian (Ye et al., 2017; Shen et al., 2018), although some ophiolites in the Tienshan give Carboniferous ages (Xu et al., 2006; Jiang et al., 2014). Also, strong intracontinental deformation occurred in the western CAOB during the Permian-Triassic (Laurent-Charvet et al., 2003; Choulet et al., 2011). In contrast, most ophiolites in the eastern CAOB (i.e., Xing'an-Mongolian Orogenic Belt) formed during the Carboniferous-Permian (Miao et al., 2007, 2008; Jian et al., 2010; Zheng et al., 2014; Song et al., 2015). Geochronological evidence suggests that the final remnant of the paleo-Asian Ocean (Solonker Seaway) closed diachronously from west to east during the Carboniferous-Permo-Triassic (Xiao et al., 2003; Li, 2006; Windley et al., 2007; Jian et al., 2010; Zheng et al., 2014; Wilde, 2015; Liu et al., 2017).However, some studies argue that the eastern segment of the Paleo-Asian Ocean closed in the Late Devonian (Xu et al., 2013; Zhao et al., 2013, 2016);

In the central CAOB, the closure of the Paleo-Asian Ocean is suggested to have occurred in the Permian (Wu et al., 1998; Li, 2006), the Late Permian (Wang et al., 1994a, 1994b, 1998; Feng et al., 2013; Xie et al., 2014; Zheng et al., 2014, 2018), or the Early Permian (Zhang et al., 2013). However, no classic ophiolites exist in the northern Alxa region (Shi et al., 2016), so the northern boundary of the Alxa Block in the context of CAOB evolution and final suturing is controversial. Our unpublished mapping of ophiolitic mélange assemblages in the Engeerwusu region (Fig. 1) shows that it is composed of blocks of carbonated mafic–ultramafic rocks, serpentinites, pillow lava, massive basalts,

limestone, and red cherts in a matrix of andesites and tuffs. The matrix is intensely sheared, indicating top-to-the-north thrusting. Thus, it is likely that during the late Paleozoic, the Paleo-Asian Ocean subducted southwards under the Alxa Block along the Engeerwusu zone which we suggest is an imbricated accretionary prism complex that marks the suture (Fig. 1; Feng et al., 2013; Zheng et al., 2014; Lin et al., 2014).

The second major class of tectonic structures in the Langshan Group includes southeast-vergent, overturned isoclinal folds (Fig. 3). The ages of bedding-parallel diorite and granite dikes in the folded Langshan Group range from ca. 840 to 250 Ma; The geological map shows that the orientation of the folds changes from northeast-southwest to north-south (Fig. 3), or to east-west further west and east of the mapped region (Shi et al., 2016), which may indicate that the folds in the Langshan Group were reoriented by younger Mesozoic deformation in the eastern Alxa Block (Fig. 3). For example, reported cumulative Mesozoic sinistral displacement of at least 180-200 km in the Alxa region (Lamb et al., 1999; Webb and Johnson, 2006; Zhang et al., 2013a; Heumann et al., 2014) may have reoriented the northeast-southwest-trending folds in the Langshan Group.

Because the northeastern Alxa Block may have rotated counterclockwise by as much as 32° due to Triassic ductile shearing (Yuan and Yang, 2015), by removing possible vertical axis rotations, the folds would have formed originally as a nearly east-west-trending compressive fold belt with vergence towards the south. Because a folded diorite dike intruding into the Langshan Group yielded a zircon U-Pb age of ca. 257 Ma (D15109-1, Fig. 6), the D2 structures in the Langshan Group must have developed after 257 Ma. If the second deformation in the Langshan Group was caused by closure of the Paleo-Asian Ocean, the closure of the ocean occurred during or after 257 Ma, which is similar to published ages constrained by radiolarian fossils in cherts (i.e., the Late Permian; Xie et al., 2014). Furthermore, this age is similar to the reported timing of terminal seaway closure along the Solonker suture zone to the east (Xiao et al., 2015).

8.4 Formation of late Paleozoic ductile shear zones along the southern margin of the CAOB (D3; Fig. 24E)

Regional strike-slip faults may cause lateral overlap of orogenic elements in accretionary orogens and this may have been an important process in the central-eastern CAOB including the Alxa Block (Şengör, et al., 1993, 2018; Şengör, and Natal'in, 1996; Laurent-Charvet et al., 2003; Buslov et al., 2004). In the western part of the CAOB, the North Tienshan shear zone experienced dextral strike-slip during 270-240 Ma (Shu et al., 1998, 1999; Lauren-Charvet et al., 2003; Jong et al., 2009; Cai et al., 2012; Wang et al., 2010). In the Beishan region, dextral ductile deformation at 323-209 Ma is reported (Song et al., 2018b). To the east of the Alxa Block, the Xar Moron Fault in the eastern CAOB underwent dextral shear between 227-209 Ma (Zhao et al., 2015). Wang et al. (2014)

also reported large-scale dextral ductile deformation along the northern margin of the NCC during 255-241 Ma. The east-west-trending ductile dextral shear belt in the Langshan region documented in this study may thus have greater regional significance (Wang et al., 1994b; Zhang, 2019) and be part of a postulated 3000-km-long Late Permian-Early Triassic dextral strike-slip system extending from Kazakhstan in the west to the Tienshan, Alxa Block, and northern margin of the NCC (Shu et al., 1998, 1999; Laurent-Charvet et al., 2003; Jong et al., 2009; Wang et al., 2010; Wu et al., 2012; Wang et al., 2014; Zhao et al., 2015; Song et al., 2018b).

Tectonic drivers for late Paleozoic dextral shear in the western CAOB is attributed to intracontinental adjustment in the North Tianshan after the collision between the Siberian Craton and the Tarim Craton in the late Paleozoic (Shu et al.,1998, 1999), including anticlockwise rotation of the Junggar Block (Laurent-Charvet et al., 2002, 2003), and WNW-ESE-oriented post-collisional extrusion of the CAOB eastward between the Tarim Craton and the Siberian Craton (Wang et al., 2010). In addition, dextral shearing in the Beishan area was driven by block rotations between the Siberian, Tarim and Junggar Blocks (Cai et al., 2012) and oblique convergence during collisional assembly of the southern CAOB (Song et al., 2018b). The tectonic driver for the latest Paleozoic deformation in and around the Alxa Block and eastern CAOB is uncertain, but published paleomagnetic data support: 1) a model of dextral ductile shearing during collision between the NCC and the Mongolian terrane collage and eastward extrusion of eastern-central Asia (Wang et al., 2014; Zhao et al., 2015) and 2) eastward displacement of the Yili-Junggar Block further west as a tectonic wedge bound by strike-slip shear zones between the Siberian and Tarim Cratons (Wang et al., 2007)**.**

8.5 Far-field effects of the collision between the NCC and Yangtze Craton (D4; Fig. 24F)

The northeast-trending ductile sinistral strike-slip system is the most noticeable and penetratively developed structure in the Langshan study area. The shear zone cuts or deforms all earlier structures and generated the present-day northeast-striking tectonic framework (‘structural grain’) in the study region.

The mylonite resulting from the shearing during this period developed mainly in the Carboniferous granite and coeval granitic dikes intruding the Diebusige Complex in the southwestern segment of the Langshan. The emplacement age of the granite is between 348±1 and 329±1 Ma (Zhang et al., 2013a; Dan et al., 2016; this study). In the eastern Alxa Block, Carboniferous granite plutons are only distributed in the study region and the southwestern end of the Bayanwulashan to the southwest (Fig. 2). This sinistral strike-slip shear zone cuts the Engeerwusu-Solonker suture zone and has a two-phase history of D4 ductile shear and later brittle reactivation with cumulative sinistral displacement

equal to180~200 km (Zhang et al., 2013a). This shear zone was previously interpreted to be an important intraplate boundary between the Alxa and Ordos blocks in the Late Triassic reactivated by collision or compression between the NCC and the Yangtze Craton farther south (Meng and Zhang, 1999; Zhang et al., 2013a; Huang et al., 2018; Zhao et al., 2018). This shear zone connects to the Bayanwulashan shear zone to the southwest and extends northeastwards into southern Mongolia. A significant NE-trending sinistral shearing event has also been documented in southern Mongolian between 250 and 209 Ma (Lamb et al., 1999; Hendrix et al., 2001; Webb et al., 2010; Webb and Johnson, 2006). Within the study region, approximately north-south-trending sinistral shearing is also documented along the boundary between the Permian granite and the Langshan Group, which happened in the Late Cretaceous (see descriptions of Domains I-III; Figs. 1, 2; Darby and Ritts, 2002).

8.6 Late Jurassic crustal reactivation (D5; Fig. 25A)

Late Jurassic thrusting along the eastern Alxa Block was synchronous with a deformation event that developed in southern and central Mongolia and the northern NCC (Fig. 25A). The driving mechanism for this widespread event is debated (Liu, 1998; Darby and Ritts, 2002; Faure et al., 2012; Dong et al., 2015; Cunningham, 2017; Gillespie et al., 2017). The main hypotheses include (1) closure of the Mongol-Okhotsk Ocean to the north (Zorin, 1999; Vassallo et al., 2007; Yang et al., 2015; Cunningham, 2017); (2) subduction of the Paleo-Pacific Plate (Darby and Ritts, 2002; Faure et al., 2012); and (3) collision of the Qiangtang and Lhasa blocks (Liu,1998). The Jurassic closure of the Mongol-Okhotsk Ocean is interpreted to be the driver for the development of east-west folds and thrusts in southernmost Mongolia (Jolivet et al., 2007; Yang et al., 2015; Cunningham, 2017). However, 300 km to the SE, the north-south-trending thrust belt in the eastern Alxa Block, including the Langshan and the Helanshan (Fig. 1), is perpendicular to the E-W-trending fold-thrust belt in southern Mongolia (Cunningham, 2017). Therefore, we suggest that west-dipping low-angle subduction of the Paleo-Pacific Plate was the most likely driver for northwest-southeast contractional deformation in the northeastern Alxa Block (Darby and Ritts, 2002; Faure et al., 2012; Zhang et al., 2020; Figs. 5, 25). Low-angle subduction may have also caused intraplate deformation within the NCC (Faure et al., 2012).

In the mapped region, east-west-trending dextral strike-slip faults developed in almost all domains (Fig. 3). Because these faults and the northeast-southwest-trending thrust faults mutually cross-cut or change continuously along the strike, these two sets of faults are interpreted to be coeval and Late Jurassic in age. The east-west-trending dextral faults appear to have acted as lateral ramps to accommodate different displacements between thrust sheets. One of the east-west-trending faults extends

westwards from the mapped region along the northern boundary of outcropping late Paleozoic granite and Neoproterozoic sedimentary rocks (i.e., the Langshan Group; Fig. 2). Along this fault to the west, the Second Formation of the Langshan Group trends nearly east-west (Fig. 2).

Similar Late Jurassic east-west-trending strike-slip faults are reported in regions to the west of the Alxa Block, such as in the Beishan orogenic belt (Zheng et al., 1996; Zhang and Cunningham, 2012), the Hexi Corridor and the southern Alxa Block (Vincent and Allen, 1999). In the Helanshan to the south of the mapped region, a large Late Jurassic east-west-trending dextral strike-slip fault cuts across the northern Helanshan fold-and-thrust belt (i.e., the Zhengyiguan Fault, Fig. 2; Darby and Ritts, 2002). The north-south-trending Helanshan fold-and-thrust belt and east-west-trending dextral slip faults along the northern boundary of the NCC were likely formed during westward subduction of the Paleo-Pacific Plate under the NCC during the Late Jurassic (Faure et al., 2012). Although compressional stress from the East Asian convergent margin is considered the key driver for Late Jurassic deformation in the NCC (Faure et al., 2012; Zhang et al., 2020), contemporaneous closure of the Mongol-Okhotsk Ocean to the N and collision between the Qiangtang and the Lhasa blocks to the SW may have generated a complex stress field with reactivation of older structures in different kinematic modes, based on their pre-existing orientations.

8.7 Early Cretaceous tectonism (D6; Fig. 25B)

The eastern Alxa Block experienced regional WNW-ESE extension and widespread eruption of basalts in the Early Cretaceous (Fig. 5, Darby and Ritts, 2007; Hui et al., 2020). A low-angle detachment fault and a supra-detachment basin controlled by the fault developed in the study region. Early Cretaceous crustal extension created low-angle detachment faults and metamorphic core complexes (MCCs) over a wide region including the northern NCC, southern Mongolian borderland region, Gobi Altai, eastern Mongolia and Alxa Block (Davis et al., 2002; Meng et al., 2003; Johnson, 2004; Wang et al., 2011; Lin et al., 2013; Lin and Wei, 2018). It is widely believed that this regional extensional event was due to terminal closure of the Mongol-Okhotsk seaway and a change in the regional stress field within Central Asia as the final convergent plate boundary within the CAOB was closed and the slab pull driving force for inter- and intraplate compression was eliminated. This allowed widespread extension to occur in regions of overthickened crust with stored gravitational potential energy and possibly high geothermal gradients (Meng, 2003, Cunningham, 2010, 2017). Alternatively, and/or perhaps synchronously, early Cretaceous ESE extension in the Alxa Block may have been caused by eastward rollback of the Paleo-Pacific Ocean plate and subsequent eastward flow of the mantle lithosphere of the upper Eurasian Plate driving upper-crustal thinning (Hui et al., 2020,

Fig. 25B). This may have contributed to the proposed foundering of the upper Eurasian plate's lower mantle lithosphere (Lin et al., 2013; Lin and Wei, 2018).

8.8 Late Cretaceous inversion (D7; Fig. 25C)

During the Late Cretaceous, almost all Early Cretaceous extensional basins in the NCC and Alxa Block stopped subsiding and were tectonically inverted (Ren et al., 2002). However, the reasons for this inversion are unknown. AFT dating indicates that Late Cretaceous deformation, uplift and exhumation in and around the study region occurred during 100-70 Ma (Feng et al., 2017; Cui et al., 2018). The northeast-southwest-trending sinistral strike-slip faults that cut Lower Cretaceous strata in the study area are covered by conglomerates of the Oligocene Wulanbulage Formation, indicating that they may have formed in the Late Cretaceous.

In the Late Cretaceous, a major plate reconfiguration occurred both to the southwest and to the east of China. The Neo-Tethys oceanic plate experienced flat subduction northwards beneath the Lhasa Block (Wen et al., 2008), generating compression between the Lhasa Block and the Qiangtang Block to the north. This compression led to ~50% crustal shortening in the northern Lhasa Block and the development of compressive basins in the Lhasa Block (Pullen et al., 2008). A rapid cooling event occurred in the northern Qinghai-Tibetan Plateau and eastern Kunlun Mountains during ~115-70 Ma (Jolivet et al., 2001). A Late Cretaceous tectonic event indicated by a widespread unconformity has been documented in the Hexi Corridor to the north of the Qinghai-Tibetan Plateau (Zhang et al., 2017), and in SE Mongolia, Late Jurassic-Early Cretaceous rift basins experienced a transpressional inversion event during the mid-Cretaceous (Graham et al., 2001). During the same period, the Izanagi Plate to the east of the Eurasian Plate was subducting rapidly towards the north-northwest at 120-140 mm/y (Northrup et al., 1995), which drove sinistral shearing in the eastern Eurasian Plate (Maruyama et al., 1997). The oblique collision of a microcontinent/oceanic plateau, such as the western Philippine Block or Palawan Block (Faure, 1989; Niu et al., 2015; Ratschbacher et al., 2003) or the Okhotsk Block (Yang et al., 2015), along the Eurasian Plate's eastern margin may also have driven the Late Cretaceous inversion of Early Cretaceous basins in the continental interior of eastern Central Asia. The shortening direction of this period in the study region is generally northwest-southeast (Fig. 5), which may also indicate a driving from the southeast direction.

Darby and Ritts (2002) identified a major nearly north-south-trending sinistral strike-slip fault east of the Helanshan, which formed in the Late Cretaceous. This fault extends northwards into the study region, where a series of nearly north-south-trending sinistral strike-slip faults are developed (Fig. 3). Using the boundary between the Permian granite and the Langshan Group as a marker (i.e., the east-west-trending shear zone), the

cumulative sinistral displacement of these north-south-trending faults in the mapped region is up to 10 km (Figs. 2, 3) or up to 20 km if the region to the south of the mapped area is included (Fig. 2). There are also similar faults to the north of the mapped region, which cut across the entire Langshan block (Fig. 2), so the ca. 20 km of estimated offset in this study is considered a minimum displacement. The nearly north-south-trending faults in the study region and the eastern Helanshan sinistral fault may belong to a larger fault system. If so, the north-south-trending faults likely developed in the Late Cretaceous. The nearly north-south-trending sinistral faults in the eastern Alxa Block suggest that the Ordos Block moved to the north during the Late Cretaceous, perhaps due to collisional stresses derived from the convergent southeastern margin of the Eurasian Plate during the Late Cretaceous (Fig. 25C), which would explain NW-SE shortening derived from fault plane solutions in the study region.

8.9 Paleogene deformation (ca. 60-40 Ma) (D8; Fig. 25D)

During the Paleogene, the main Late Cretaceous northeast-southwest-trending sinistral strike-slip fault system was reactivated in dextral strike-slip mode within the Dabashan in Domain IV. The timing of this dextral shearing ranged from 60 to 40 Ma, as constrained by AFT dating (Cui et al., 2018). The age of Hetao Basin stratigraphy also indicate basin development started in the Oligocene (TRGAFSOM, SSB, 1988). We therefore argue that the northeastern Alxa Block experienced deformation and uplift in the Paleogene.

The onset of the Indo-Eurasian collision was in the Paleogene (Hu et al., 2016), and regions within and around the Qinghai-Tibetan Plateau began to experience the ongoing far-field effects of the collision, such as the exhumation of the Qiangtang Block and the Gangdese belt (Ding et al., 2014), crustal thickening of the Qilianshan (Zhuang et al., 2011), thrusting in the western Qinling region (Duvall et al., 2011), and top-to-the-south thrusting in the southern Qilianshan (Yin et al., 2002). Many workers have argued that crustal reactivation along the northeastern plateau began in the late Cenozoic (Zheng et al., 2006 and reference therein). However, Oligocene strike-slip fault displacements are documented in southern Mongolia north of the study region and are thought to be linked to early phases of motion along the Altyn Tagh Fault (Webb and Johnson, 2006; Heumann et al., 2014). At the same time, the eastern NCC experienced regional deformation caused by back-arc extension (Ren et al., 2002), which was apparently kinematically unrelated to dextral shear on northeast-trending faults in the study area. AFT dating in the study region reveals a Paleogene cooling event between ~50-45 Ma (Cui et al., 2018). We thus cautiously suggest that mid- to late Paleogene nearly east-west shortening in the study region may have been an early and distant far-field effect of the Indo-Eurasian collision (Figs. 5, 25D).

8.10 Miocene deformation (D9)

In the study region, top-to-the-southeast or northwest thrust faults are distributed along the southeastern foothills of the Langshan range and in the Diebusige Basin to the northwest of the mountain range (Figs. 3, 21, 22). A mid- to late Cenozoic nearly E-W compressive event is also documented in the southern Helanshan farther south (Zhang et al., 2010). In the central Helanshan, there is a top-to-the-east thrust fault that cuts Lower Cretaceous conglomerates (Zhao et al., 2020).

In the Miocene, many tectonic events occurred in and around the Chinese portion of the Asian continent beyond the progressive development of the Himalayan-Tibetan deformation field, including the inversion of the Red River shear zone, the opening of the South China and Japan Sea oceanic basins (Jolivet et al., 1994; Leloup et al., 2001; Ritts et al., 1998; Yue and Liou, 1999; Zhang et al., 2008, 2010) and the transition in tectonic regime from extrusion to distributed shortening in northern Tibet (Lu et al., 2016). During this period, rapid northward subduction of the Philippine Sea Plate may have also influenced the stress field in the Alxa Block region (Hall, 2002).

Miocene thrusts in the eastern Alxa Block indicate northwest-southeast crustal compression (Fig. 5). The wedge-shaped Alxa Block moved southeastward presumably as a distant response to continued NE-directed compressive stress from the Indo-Eurasian collision to the south as the Tibetan Plateau was uplifted and expanded northeastwards. We suggest that obstruction by the rigid Ordos Block directly to the east and compressive stresses derived from SE Asian plate convergence caused localized thrust faulting in the eastern Alxa Block. Eastward displacement of the Alxa Block that drove top-to-the-west or east Miocene thrusting may also have been kinematically linked to early movement along the Altyn Tagh Fault (Yue et al., 2001b).

8.11 Pliocene-Recent tectonic activity (D10)

Crustal exhumation since ~10 Ma has occurred in the interior of the Qinghai-Tibetan Plateau and in regions around the plateau, including the NE Alxa Block region and western Ordos (i.e., Liupanshan and Helanshan; Molnar et al., 1993; Métivier et al., 1998; Tapponnier et al., 2001; Zheng et al., 2006; Liu et al., 2010). Low-temperature thermochronological dating also indicates that the Langshan experienced rapid exhumation at ~10 Ma (Cui et al., 2018). Since the Pliocene, significant multi-kilometer extensional fault displacements have occurred in the western Ordos region to the south of the Langshan range (i.e., Yinchuan Graben, Fig. 1).

Along the eastern foothills of the Langshan range (i.e., Dabashan), large active high-angle normal faults have generated a tectonically active rift margin landscape with prominent fault scarps (Fig. 23A) that cut sediments of the Late Pleistocene Jilantai

Formation and Holocene alluvium (Fig. 23B). The Holocene earthquake recurrence intervals of these faults are estimated to be approximately 2500 years (Rao et al., 2016). In addition, the Hetao Basin also began to subside rapidly at the same time (TRGAFSOM, SSB, 1988). The Dabashan footwall block is minimally eroded and is a world-class example of a normal-faulted high-relief footwall block bound by triangular and trapezoidal facets and multiple-event Holocene fault scarps (Fig. 23).

9. Conclusions

The Alxa Block is remarkable in that it is a structural archive of 10 Paleozoic to Recent tectonic events that can be distinguished in time and space. It thus stands as an outstanding example of a continental interior region that has experienced repeated crustal activation in an interplate and then intraplate setting. The tectonic position of the Alxa Block in eastern Central Asia must be considered a critical factor in its deformational history. This is because progressive changes in the stress field in Central Asia determined the kinematics of different deformation regimes over time. The changing stress field in Central Asia's crust must have reflected the complex balance of forces imposed by the surrounding evolving plate boundaries, in addition to internal gravitational effects due to lateral density variations in the Central Asian lithosphere. During the Alxa Block's Phanerozoic evolution, it was subjected to 1) compressional stresses derived from terrane or block amalgamation during southern CAOB consolidation and terminal Paleo-Asian Ocean closure; 2) far-field Triassic-Jurassic compressional plate boundary forces related to terminal closure of the Mongol-Okhotsk seaway to the north, the collision between the NCC and the Yangtze Craton to the south, and subduction of the Paleo-Pacific Ocean Plate to the east; 3) compressional and later extensional forces related to long-lived subduction and later back-arc extension to the east and southeast in response to plate convergence along Eurasia's Triassic-Recent paleo- and modern Pacific margin; 4) Cretaceous-Recent NE-directed compressional stress derived from Lhasa Block and Indian Plate convergence and collision; and 5) the gravitational potential energy stored in the elevated Tibetan Plateau contributed to NE-directed compressive stress in regions to the N and E of Tibet in the mid- to late Cenozoic. Thus, the resolved crustal stress field in and around the Alxa Block must have been highly variable since 250 Ma, as surrounding plate boundaries have kinematically evolved and changed to the north, east and south. In addition, the approximately N-S-trending eastern margin of the Alxa Block may be a long-lived crustal strength boundary along which multiple stages of reactivation have been focused. Today, this boundary forms the modern, tectonically active western portion of the rifted margin of the Ordos Block.

As a part of the southern CAOB, the northeastern Alxa Block has experienced multiple tectonic events with variable kinematics, including contractional, extensional,

oblique and strike-slip regimes since the late Paleozoic in a plate margin and later intraplate setting. Our study demonstrates that continental interior regions may be susceptible to repeated phases of reactivation throughout Earth history as distant plate margins evolve and change their dynamic character. Only detailed structural and lithological fieldwork combined with reliable age constraints for crosscutting rock units and tectonic structures can fully resolve the crustal complexity and polyphase structural evolution. The results of this study invite comparisons with the late Paleozoic-Recent tectonic evolution of adjoining regions, especially the lesser-studied Beishan region to the west and remote areas of southern and eastern Mongolia to the northwest and north.

Acknowledgments

We thank Profs. Jinyi Li, Songnian Lu, and Tao Wang from the China Geological Survey for their zealous encouragement. Additional thanks are also given to Prof. Qinglong Zhang, Prof. Guoai Xie, Mr. Amirdin Arkin, Dr. Rongsong Tian and Mr. Fahao Li from Nanjing University for their hard working during the mapping. We also thank Prof. Michel Faure and an anonymous reviewer for their thoughtful comments and constructive suggestions. This research was funded by the National Key Research and Development Program of China from the Ministry of Science and Technology of China (No. 2017YFC0601301), the National Natural Science Foundation of China (No. 41972224), and the China Geological Survey (DD20190004). The data that support the findings of this study are openly available in figshare at http://doi.org/10.6084/m9.figshare.12127176.

References

Badarch, G., Cunningham, W.D., & Windley, B.F. (2002). A new terrane subdivision for Mongolia: Implications for the Phanerozoic crustal growth of Central Asia. Journal of Asian Earth Sciences, 21, 87-110.

Buslov, M.M., Watanabe, T., Fujiwara, Y., Iwata, K., Smirnova, L.V., Safonova, Y.I., Semakov, N.N., & Kiryanova, A.P. (2004). Late Paleozoic faults of the Altai region, central Asia: tectonic pattern and model of formation. Journal of Asian Earth Sciences, 23, 655-671.

Cai, Z.H., Xu, Z.Q., He, B.Z., & Wang, R.R. (2012). Age and tectonic evolution of ductile shear zones in the eastern Tianshan-Beishan orogenic belt. Acta Petrologica Sinica, 28, 1875-1895 (in Chinese with English abstract).

Charvet, J., Shu, L., & Laurent-Charvet, S. (2007). Paleozoic structural and geodynamic evolution of eastern Tianshan (NW China): Welding of the Tarim and Junggar plates. Episodes, 30, 162-186.

Choulet, F., Chen, Y., Wang, B., Faure, M., Cluzel, D., Charvet, J., Lin, W., & Xu, B. (2011). Late Paleozoic palegeographic reconstruction of western Central Asia based upon paleomagnetic data and its geodynamic implications. Journal of Asian Earth Sciences, 42, 867-884.

Cui, X.Y., Zhao, Q.H., Zhang, J., Wang, Y.N., Zhao, H., Nie, F.J., Qu, J.F., & Zhang, B.H. (2018). Late Cretaceous-Cenozoic Multi-stage Denudation at the Western Ordos Block: constraints by the Apatite Fission Track Dating on the Langshan. Acta Geologica Sinica (English Edition), 92, 536-555.

Cunningham. D., Dijkstra, A., Howard, J., Quarles, A., & Badarch, G. (2003). Active interpolate strike-slip faulting and transpressional uplift in the Mongolian Altai. In: Intraplate strike-slip deformation belts, edited by Storti F, Holdsworth R E, Salvini F, Geological Society Special Publication, 210, 63-87.

Cunningham, D. (2010). Tectonic setting and structural evolution of the Late Cenozoic Gobi Altai orogen. Geological Society, London, Special Publications, 338, 361-387.

Cunningham, D. (2013). Mountain building processes in intracontinental oblique deformation belts: Lessons from the Gobi Corridor, Central Asia. Journal of Structural Geology, 46, 255-282.

Cunningham, D., Zhang, J., & Li, Y.F. (2016). Late Cenozoic structural evolution of the Sanweishan and Nanjieshan, western China: Sinistraltranspressionalreactivation of Archean basement directly north of the Altyn Tagh Fault along Tibet's evolving northern boundary. Tectonophysics, 687, 111-128.

Cunningham, D. (2017). Folded Basinal Compartments of the Southern Mongolian Borderland: A Structural Archive of the Final Consolidation of the Central Asian Orogenic Belt. Geosciences, 7, 1-23.

Dan, W., Li, X.H., Guo, J.H., Liu, Y., & Wang, X.C. (2012). Paleoproterozoic evolution of the eastern Alxa Block, westernmost North China: evidence from in situ zircon U–Pb dating and Hf–O isotopes. Gondwana Research, 21, 838-864.

Dan, W., Li, X.H., Wang, Q., Wang, X.C., & Liu, Y. (2014a). Neoproterozoic S-type granites in the Alxa Block, westernmost North China and tectonic implications: in situ zircon U-Pb-Hf-O isotopic and geochemical constraints. American Journal of Science, 314, 110-153.

Dan, W., Li, X.H.,Wang, Q., Tang, G.J., & Liu, Y. (2014b). The Early Permian (ca. 280 Ma) silicicigneous province in Alxa Block, NW China: a magmatic flare-up triggered by amantle-plume? Lithos, 204, 144-158.

Dan, W., Li, X.H., Wang, Q., Wang, X.C., Wyman, Derek A., & Liu, Y. (2016). Phanerozoic amalgamation of the Alxa Block and North China Craton: Evidence from Paleozoic granitoids, U-Pb geochronology and Sr-Nd-Pb-Hf-O isotope geochemistry. Gondwana Research, 32, 105-121.

Darby, B.J., Davis, G.A., & Zheng, Y.D. (2001). Structural evolution of the southwestern Daqing Shan, Yinshan belt, Inner Mongolia, China. Geological Society of America Memoirs, 194, 199–214.

Darby, B.J., & Ritts, B.D. (2002). Mesozoic contractional deformation in the middle of the Asian tectonic collage: the intraplate Western Ordos fold thrust belt, China. Earth and Planetary Science Letters, 205, 13-24.

Darby, B.J., Ritts, B.D., Yue, Y.J., & Meng, Q.R. (2005). Did the Altyn Tagh fault extend beyond the Tibetan Plateau?. Earth and Planetary Science Letters, 240, 425-435.

Darby, B.J., & Ritts, B.D. (2007). Mesozoic structural architecture of the Lang Shan, North-Central China: Intraplate contraction, extension, and synorogenic sedimentation. Journal of Structural Geology, 29, 2006-2016.

Davis, G.A., Darby, B.J., Zheng, Y.D., & Spell, T.L. (2002).Geometric and temporal evolution of an extensional detachment fault, Hohhot metamorphic core complex, Inner Mongolia, China. Geology, 30, 1003-1006.

De Grave, J., Buslov, M.M., & Van den haute, P. (2007). Distant effects of India-Eurasia convergence and Mesozoic intracontinental deformation in Central Asia: constraints from apatite fission-track thermochronology. Journal of Asian Earth Sciences, 29, 188-204.

Ding, L., Xu, Q., Yue, Y.H., Wang, H.Q., Cai, F.L., & Li, S. (2014). The Andean-type Gangdese Mountains: paleoelevation record from the Paleocene–Eocene Linzhou Basin. Earth and Planetary Science Letters, 392, 250-264.

1146 Dong, S.W., Zhang, Y.Q., Zhang, F.Q., Cui, J.J., Chen, X.H., Zhang, S.H., Miao, L.C., Li, J.H., Shi, W., Li,
1147 Z.H., Huang, S.Q., & Li, H.L. (2015). Late Jurassic–Early Cretaceous continental convergence and
1148 intracontinental orogenesis in East Asia: A synthesis of the Yanshan Revolution. Journal of Asian
1149 Earth Sciences, 114, 750-770.
1150 Duvall, A.R., Clark, M.K., Van der Pluijm, B., & Li, C.Y. (2011). Direct dating of Eocene reverse faulting in
1151 northeastern Tibet using Ar-dating of fault clays and low-temperature thermochronometry. Earth and
1152 Planetary Science Letters, 304, 520-526.
1153 Edel, J.B., Schulmann, K., Hanžl, P., & Lexa, O. (2014). Palaeomagnetic and structural constraints on
1154 90° anticlockwise rotation in SW Mongolia during the Permo–Triassic: Implications for Altaid
1155 oroclinal bending. Preliminary palaeomagnetic results. Journal of Asian Earth Sciences, 94, 157-
1156 171.
1157 Faure, M. (1989). Pre-Eocene synmetamorphic structure in the Mindoro-Romblon-Palawan area, west
1158 Philippines, and implications for the history of Southeast Asia. Tectonics, 8, 963–979.
1159 Faure, M., Lin, W., & Chen, Y. (2012). Is the Jurassic (Yanshanian) intraplate tectonics of North China
1160 due to westward indentation of the North China block? Terra Nova, 24, 456-466.
1161 Feng, L.X., Brown, R.W., Han, B.F., Wang, Z.Z., Łuszczak, K., Liu, B., Zhang, Z.C., & Ji, J.Q. (2017).
1162 Thrusting and exhumation of the southern Mongolian Plateau: Joint thermochronological constraints
1163 from the Langshan Mountains, western Inner Mongolia, China. Journal of Asian Earth Sciences,
1164 144, 287-302.
1165 Feng, J.Y., Xiao, W.J., Windley, B., Han, C.M., Wan, Bo, Zhang, J.E., Ao, S.J., Zhang, Z.Y., & Lin, L.N.
1166 (2013). Field geology, geochronology and geochemistry of mafic–ultramafic rocks from Alxa, China:
1167 implications for late Permian accretionary tectonics in the southern Altaids. Journal of Asian Earth
1168 Sciences, 78, 114-142.
1169 Gao, J., Long, L., Klemd, R., Qian, Q., Liu, D., Xiong, X., Su, W., Liu, W., Wang, Y., & Yang, F. (2009).
1170 Tectonic evolution of the South Tianshan orogen and adjacent regions, NW China: Geochemical
1171 and age constraints of granitoid rocks. International Journal of Earth Sciences, 98, 1221-1238.
1172 Geng, Y.S., & Zhou, X.W. (2010). Early Neoproterozoic granite events in Alxa area of Inner Mongolia
1173 and their geological significance: evidence from geochronology. Acta Petrologica et Mineralogica,
1174 29, 779-795 (in Chinese with English abstract).
1175 Graham, S.A., Hendrix, M.S., Johnson, C.L., Badamgarav, D., Badarch, G., Amory, J., Porter, M.,
1176 Barsbold, R., Webb, L.E. & Hacker, B.R. (2001). Sedimentary record and tectonic implications of
1177 Mesozoic rifting in southeast Mongolia. Geological Society of America Bulletin, 113, 1560-1579.
1178 Gillespie, J., Glorie, S., Xiao, W.J., Zhang, Z.Y., Collins, A.S., Evans, N., McInnes, B., & De Grave, J.
1179 (2017). Mesozoic reactivation of the Beishan, southern Central Asian Orogenic Belt: insights from
1180 low-temperature thermochronology. Gondwana Research, 43, 107-122.
1181 Guy, A., Schulmann, K., Clauer, N., Hasalova, P., Seltmann, R., Armstrong, R., & Benedicto, A. (2014).
1182 Late Paleozoic–Mesozoic tectonic evolution of the Trans-Altai and South Gobi Zones in southern
1183 Mongolia based on structural and geochronological data. Gondwana Research, 25, 309-337.
1184 Hall, R., 2002. Cenozoic geological and plate tectonic evolution of SE Asia and the SW Pacific:
1185 computer-based reconstructions, model and animations. Journal of Asian Earth Sciences, 20, 353-
1186 431.
1187 Heumann, M.J., Johnson, C.L., Webb, L.E., Taylor, J.P., & Minjin, C. (2014). Total and incremental left-
1188 lateral displacement across the East Gobi Fault Zone, southern Mongolia: Implications for timing
1189 and modes of polyphase intracontinental deformation. Earth and Planetary Science Letters, 392, 1-

15.

Heumann, M.J., Johnson, C.L., & Webb, L.E. (2018). Plate interior polyphase fault systems and sedimentary basin evolution: A case study of the East Gobi Basin and East Gobi Fault Zone, southeastern Mongolia. Journal of Asian Earth Sciences, 151, 343-358.

Hu, J.M., Gong, W.B., Wu, S.J., Liu, M., & Liu, S.C. (2014). LA-ICP-MS zircon U-Pb dating of the Langshan Group in the northeast margin of the Alxa block, with tectonic implications. Precambrian Research, 255, 756-770.

Hu, X.M., Garzanti, E., Wang, J.G., Huang, W.T., An, W., & Webb, A. (2016). The timing of India-Asia collision onset – Facts, theories, controversies. Earth-Science Reviews, 160, 264-299

Huang, T.K., 1945. On the major tectonic forms of China. Geol. Mem. Ser. A 20, 1-165.

Huang, B.C., Yan, Y.G., Piper, J.D.A., Zhang, D.H., Yi, Z.Y., Yu, S., & Zhou, T.H. (2018). Paleomagnetic constraints on the paleogeography of the East Asian blocks during Late Paleozoic and Early Mesozoic times. Earth-Science Reviews, 186, 8–36.

Hui, J., Cheng, H.Y., Zhang, J., Zhang, K.J., Qu, J.F., & Zhang, B.H. (2020). Early Cretaceous continent basalts in the Alxa Block, NW China: Geochronology, geochemistry, and tectonic implications. International Geology Review, Doi:10.1080/00206814.2020.1734974.

Jahn, B.M., Windley, B., Natal'in, B., & Dobretsov, N. (2004). Phanerozoic continental growth in Central Asia. Journal of Asian Earth Sciences, 23, 599-603.

Jian, P., Liu, D.Y., Kröner, A., Windley, B.F., Shi, Y.R., Zhang, W., Zhang, F.Q., Miao, L.C., Zhang, L.Q., & Tomurhuu, D. (2010). Evolution of a Permian intraoceanic arc-trench system in the Solonker suture zone, Central Asian Orogenic Belt, China and Mongolia. Lithos, 118, 169-190.

Jiang, T., Gao, J., Klemd, R., Qian, Q., Zhang, X., Xiong, X., Wang, X., Tan, Z., & Chen, B. (2014). Paleozoic ophiolitic mélanges from the South Tianshan Orogen, NW China: Geological, geochemical and geochronological implications for the geodynamic setting. Tectonophysics, 612-613, 106-127.

Johnson, C.L. (2004). Polyphase evolution of the East Gobi basin: sedimentary and structural records of Mesozoic-Cenozoic intraplate deformation in Mongolia. Basin Research, 16, 79-99.

Johnson, C.L., Amory, J.A., Zinniker, D., Lamb, M.A., Graham, S.A., Affolter, M., & Badarch, G. (2008). Sedimentary response to arc-continent collision, Permian, southern Mongolia. Geological Society of America Special Paper, 436, 363-390.

Jolivet, M., Brunel, M., Seward, D., Xu, Z., Yang, J., Roger, F., Topponnier, P., Malavieille, J., Arnaud, N., & Wu, C. (2001). Mesozoic and Cenozoic tectonics of the northern edge of the Tibetan plateau: fission-track constraints. Tectonophysics, 343, 111-134.

Jolivet, M., Ritz, J.F., Vassallo, R., Larroque, C., Braucher, R., Todhileg, M., Chauvet, A., Sue, C., Arnaud, N., Vicente, R.D., Arzhanikova, A., & Arzhanikov, S. (2007). Mongolian summits: an uplifted, flat, old but still preserved erosion surface. Geology, 35, 871-874.

Jong, K., Wang, B., & Faure, M. (2009). New $^{40}Ar/^{39}Ar$ age constraints on the Late Palaeozoic tectonic evolution of the western Tianshan (Xinjiang, northwestern China), with emphasis on Permian fluid ingress. International Journal of Earth Sciences, 98, 1239-1258.

Kröner, A., Kovach, V., Belousova, E., Hegner, E., Armstrong, R., Dolgopolova, A., Seltmann, R., Alexeiev, D.V., Hoffmann, J.E., Wong, J. & Sun, M. (2014). Reassessment of continental growth during the accretionary history of the Central Asian Orogenic Belt. Gondwana Research, 25, 103-125.

Lamb, M.A., Hanson, A.D., Graham, S.A., Badarch, G., & Webb, L.E. (1999). Left-lateral sense offset of

upper Proterozoic to Paleozoic features across the Gobi Onon, Tost, and Zuunbayan faults in southern Mongolia and implications for other Central Asian faults. Earth and Planetary Science Letters, 173, 183-194.

Laurent-Charvet, S., Charvet, J., Shu, L.S., Ma, R.S., & Lu, H.F. (2002). Palaeozoic late collisional strike-slip deformations in Tianshan and Altay, Eastern Xinjiang, NW China. Terra Nova, 14, 249-256.

Laurent-Charvet, S., Charvet, J., Monie´, P., & Shu, L. S. (2003). Late Paleozoic strike-slip shear zones in eastern central Asia (NW China): New structural and geochronological data. Tectonics, 22, 1009-1034.

Lehmann, J., Schulmann, K., Lexa, O., Corsini, M., Kröner, A., Štípská, P., Tomurhuu, D., & Otgonbator, D. (2010). Structural constraints on the evolution of the Central Asian Orogenic Belt in SW Mongolia. American Journal of Science, 310, 575-628.

Leloup, P.H., Arnaud, N., Lacassin, R., Kienast, J.R., Harrison, T.M., Trong, T.P., Replumaz, A., & Tapponnier, P. (2001). New constraints on the structure, thermochronology, and timing of the Ailao Shan-Red River shear zone, SE Asia. Journal of Geophysical Research, 106, 6683-6732.

Li, J.Y. (2006). Permian geodynamic setting of Northeast China and adjacent regions: Closure of the Paleo-Asian Ocean and subduction of the Paleo-Pacific Plate. Journal of Asian Earth Sciences, 26,207-224

Lin, W., Wang, J., Liu, F., Ji, W.B., & Wang, Q.C. (2013). Late Mesozoic extension structures on the North China Craton and adjacent regions and its geodynamics. Acta Petrologica Sinica, 29, 1791-1810 (in Chinese with English abstract).

Lin, W., & Wei, W. (2018). Late Mesozoic extensional tectonics in the North China Craton and its adjacent regions: a review and synthesis. International Geology Review, DOI: 10.1080/00206814.2018.1477073.

Lin, L.N., Xiao, W.J., Wan, B., Windley, B.F., Ao, S.J., Han, C.M., & Feng, J.Y. (2014), Geochronologic and geochemical evidence for persistence of south-dipping subduction to Late Permian time, Langshan area, Inner Mongolia (China): significance for termination of accretionary orogenesis in the southern Altaids. American Journal of Science, 314, 679-703.

Liu, S.F. (1998). The coupling mechanism of basin and orogen in the western Ordos Basin and adjacent regions of China. Journal of Asian Earth Science, 16, 369-383.

Liu, J.H., Zhang, P.Z., Zheng, D.W., Wan, J.L., Wang, W.T., Du, P., & Lei, Q.Y. (2010). Pattern and timing of late Cenozoic rapid exhumation and uplift of the Helan Mountain, China. Science in China (Earth Science), 40, 50-60.

Liu, J., Xie, F. & Lv, Y. (2016). Seismic hazard assessments for the Ordos Block and its periphery in China. Soil Dynamics and Earthquake Engineering, 84, 70-82.

Liu, Y.J., Li, W.M., Feng, Z.Q., Wen, Q.B., Neubauer, F., & Liang, C.Y. (2017). A review of the Paleozoic tectonics in the eastern part of Central Asian Orogenic Belt. Gondwana Research, 43, 123-148.

Lu, H.J., Fu, B.H., Shi, P.L., Ma, Y.X., & Li, H.B. (2016). Constraints on the uplift mechanism of northern Tibet. Earth and Planetary Science Letters, 453, 108-118.

Ludwig, K.R. (2003). User's Manual for Isoplot 3.0: A Geochronological, Toolkit for Microsoft Excel: Berkeley, CA, Berkeley Geochronological Center, 1-71.

Marrett, R., & Allmendinger, R.W. (1990). Kinematic analysis of fault-slip data. Journal of Structural Geology, 12, 973–986.

Maruyama, S., Isozaki, Y., Kimura, G., & Terabayashi, M.C. (1997). Paleogeographic mapsof the

Japanese Islands: plate tectonic systhesis from 750 Ma to the present. Island Arc, 6,121-142.
Meng, Q., and Zhang, G. (1999). Timing of collision of the North and South China blocks: Controversy and reconciliation. Geology, 27, 123-126.
Meng, Q.R., Hu, J.M., Jin, J.Q., Zhang, Y., & Xu, D.F. (2003). Tectonics of the late Mesozoic wide extensional basin system in the China-Mongolia border region. Basin Research, 15, 397-416.
Miao, L., Zhang, F., Fan, W.M., & Liu, D.(2007). Phanerozoic evolution of the Inner Mongolia-Daxinganling orogenic belt in North China: Constraints from geochronology of ophiolites and associated formations. Geological Society London Special Publication, 280, 223-237.
Miao, L., Fan, W., Liu, D., Zhang, F., Shi, Y., & Guo, F. (2008). Geochronology and geochemistry of the Hegenshan ophiolitic complex: Implications for late-stage tectonic evolution of the Inner Mongolia-Daxinganling Orogenic Belt, China. Journal of Asian Earth Sciences, 32, 348-370
Molnar, P., Tapponnier, P. (1975). Cenozoic tectonics of Asia; effects of a continental collision. Science, 189, 419-426.
Molnar, P., England, P., & Martinod, J. (1993). Mantle dynamics, uplift of the Tibetan Plateau, and the Indian monsoon. Review of Geophysics, 31, 357-396.
Niu, P.F., Qu, J.F., Zhang, J., Zhang, B.H., & Zhao, H. (2019). Deformation study of the Diebusige complex in the Langshan area and its tectonics implication. Acta Geologica Sinica, 93, 1867-1884 (in Chinese with English abstract).
Northrup, C. J., Royden, L. H., Burchfiel, B. C. (1995). Motion of the Pacific plate relative to Eurasia and its potential relation to Cenozoic extension along the eastern margin of Eurasia. Geology, 23, 719-722.
Pullen, A., Kapp, P., Gehrels, G.E., DeCelles, P.G., Brown, E.H., Fabijanic, J.M., & Ding, L. (2008). Gangdese retroarc thrust belt and foreland basin deposits in the Damxung area, southern Tibet. Journal of Asian Earth Sciences, 33, 323-336.
Rao, G., Chen, P., Hu, J. M., Yu, Y. L., & Qiu, J. H. (2016). Timing of Holocene paleo-earthquakes along the Langshan Piedmont Fault in the western Hetao Graben, North China: Implications for seismic risk. Tectonophysics, 677, 115-124.
Ratschbacher, L., Hacker, B.R., Calvert, A., Webb, L.E., Grimmer, J.C., McWilliams, M. O., Trevor, I., Dong, S.W., & Hu, J.M. (2003). Tectonics of the Qinling (Central China). tectonostratigraphy, geochronology, and deformation history. Tectonophysics, 366, 1-53.
Ren, J.Y., Tamaki, K., Li. S.T., & Zhang, J.X. (2002). Late Mesozoic and Cenozoic rifting and its dynamic setting in eastern China and adjacent areas. Tectonophysics, 344, 175-205.
Şengör, A.M.C., Natal'in, B.A., & Burtman, V.S. (1993). Evolution of the Altaid tectonic collage and Palaeozoic crustal growth in Eurasia. Nature, 364, 299-307.
Şengör, A.M.C., Natal'in, B.A., Sunal, G., & van der Voo, R. (2018). The tectonics of the Altaids: Crustal growth during the construction of the continental lithosphere of Central Asia between ~750 and ~130 Ma ago. Annual Review of Earth and Planetary Science, 46, 439-494.
Şengör, A. M. C., & Natal'in, B.A. (1996). Paleotectonics of Asia: Fragments of a synthesis. Cambridge University Press, 486-640.
Shen, Q.H., Geng, Y.S., Wang, X.S., &Wu, C.M. (2005). Petrology, geochemistry, formation environment and ages of Precambrian amphibolites in Alxa region. Acta Petrologica et Mineralogica. 24, 21-31 (in Chinese with English abstract).
Shen, X.M., Zhang, H.X., Wang, Q., Saha, A., Ma, L., & Santosh, M. (2018). Zircon U-Pb geochronology and geochemistry of Devonian plagiogranites in the Kuerti area of southern Chinese Altay,

northwest China: Petrogenesis and tectonic evolution of late Paleozoic ophiolites. Geological Journal, 53, 1886-1905.

Shi, G.Z., Song, G.Z., Wang, H., Huang, C.Y., Zhang, L.D., & Tang, J.R. (2016). Late Paleozoic tectonics of the Solonker Zone in the Wuliji area, Inner Mongolia, China: Insights from stratigraphic sequence, chronology, and sandstone geochemistry. Journal of Asian Earth Sciences, 127, 100-118.

Shu, L.S., Charvet, J., & Ma, R.S. (1998). Study of a large scale Paleozoic dextral strike-slip dutile shear zone along the northern margin of the Central Tianshan, Xinjiang. Acta Geoligica Sinica, 16, 326-336 (in Chinese with English abstract).

Shu, L.S., Chavert, J., Guo, L.Z., & Lu, H.F. (1999). A large-scale Palaeozoic dextral ductile strike-slip zone: the Aqqikkudug-Weiya Zone along the Northern Margin of the Central Tianshan Belt, Xinjiang, NW China. Acta Geologica Sinica, 73, 148-162 (in Chinese with English abstract).

Song, S., Wang, M.M., Xu, X., Wang, C., Niu, Y., Allen, M. B., & Su, L. (2015). Ophiolites in the Xing'an-Inner Mongolia accretionary belt of the CAOB: Implications for two cycles of seafloor spreading and accretionary orogenic events. Tectonics, 34, 2221-2248.

Song, D., Xiao, W., Collins, A.S., Glorie, S., Han, C., & Li, Y. (2018a). Final Subduction Processes of the Paleo–Asian Ocean in the Alxa Tectonic Belt (NW China): Constraints from Field and Chronological Data of Permian Arc–Related Volcano–Sedimentary Rocks. Tectonic, 37, 1658-1687.

Song, D.F., Xiao, W.J., Han, C.M., Tian, Z.H., & Li, Y.C. (2018b). Accretionary processes of the central segment of Beishan: constraints from structural deformation and 40Ar/39Ar geochronology. Acta Petrologica Sinica 34(7), 2087-2098 (in Chinese with English abstract).

Sun, L.X., Zhao, F.Q., Wang, H.C., Ren, B.F., Peng, S.H., & Teng, F. (2013). Zircon U-Pb geochronology of metabase rocks from the Baoyintu Block in the Langshan area, Inner Mongolia, and its tectonic significance. Acta Geologica Sinica, 87, 197-207 (in Chinese with English abstract).

Tapponnier, P., Xu, Z.Q., Francoise, R., Meyer, B., Arnaud, N., Wittlinger, G., & Yang, J.S. (2001). Oblique stepwise rise and growth of the Tibet Plateau. Science, 294, 1671-1677.

The research group on “Active fault system around Ordos Massif”, State Seismological Bureau (TRGAFSOM, SSB). (1988). Active fault system around Ordos Massif. Seismological Press, 1-335.

Vassallo, R., Jolivet, M., Ritz, J.F., Braucher, R., Larroque, C., Sue, C., Todbileg, M., & Javkhlanbold, D. (2007). Uplift age and rates of the Gurvan Bogd system (Gobi-Altay) by apatite fission track analysis. Earth and Planetary Science Letters, 259, 333-346.

Vincent, S.J., & Allen, M.B. (1999). Evolution of the Minle and Chaoshui Basins, China: Implications for Mesozoic strike-slip basin formation in Central Asia. Geological Society of America Bulletin, 111, 725-742.

Wang, T.Y., Wang, J.R., Liu, J.K., Wang, S.Z., & Wu, J.H. (1994a). Igneous rock associations and geochemical characteristics of volcanic arc with continental crustal basement in Zongnaishan-Shalazhashan. Geochimica, 23, 162-172 (in Chinese with English abstract).

Wang, T.Y., Wang, S.Z., & Wang, J.R. (1994b). The Formation and Evolution of Paleozoic Continental Crust in Alxa Region. Lanzhou University Press, Lanzhou, 1–215.

Wang, T.Y., Gao, J.P., & Wang, J.R. (1998). Magmatism of collisional and post-orogenic period in Northern Alaxa Region in Inner Mongolia. Acta Geologica. Sinica, 72, 126-137(in Chinese with English abstract).

Wang, T., Zheng, Y., Gehrels, G., & Mu, Z. (2001). Geochronological evidence for existence of South Mongolian microcontinent: a zircon U-Pb age of grantoid gneisses from the Yagan-Onch Hayrhan metamorphic core complex. Chinese Science Bulletin, 46, 2005-2008.

Wang, T., Zheng, Y.D., Zhang, J.J., Zeng, L.S., Donskaya, T., Guo, L., & Li, J.B. (2011). Pattern and kinematic polarity of late Mesozoic extension in continental NE Asia: perspectives from metamorphic core complexes. Tectonics, 30, TC6007.

Wang, B., Chen, Y., Zhan, S., Shu, L.S., Faure, M., Cluzel, D., Charvet, J., & Laurent-Charvet, S. (2007). Primary Carboniferous and Permian paleomagnetic results from the Yili Block (NW China) and their implications on the geodynamic evolution of Chinese Tianshan Belt. Earth and Planetary Science Letters, 263, 288-308.

Wang, Y., Li, J.Y., & Sun, G.H. (2010). Postcollisional Eastward Extrusion and Tectonic Exhumation along the Eastern Tianshan Orogen, Central Asia: Constraints from Dextral Strike-Slip Motion and $^{40}Ar/^{39}Ar$ Geochronological Evidence. The Journal of Geology, 116, 599-618.

Wang, Z.H., & Wan, J.L. (2014). Collision-Induced Late Permian-Early Triassic transpressional deformation in the Yanshan Tectonic Belt, North China. The Journal of Geology, 122, 705-716.

Webb, L.E., & Johnson, C.L. (2006). Tertiary strike-slip faulting in southeastern Mongolia and implications for Asian tectonics. Earth and Planetary Science Letters, 241, 323-335.

Webb, L.E., Johnson, C.L., Minjin, C. (2010). Late Triassic sinistral shear in the East Gobi Fault Zone, Mongolia. Tectonophysics, 495, 246-255.

Wei, W., Dijin, W., Bin, Z., Yong, H., Caihong, Z., Kai, T., & Shaomin, Y. (2014). Horizontal crustal deformation in Chinese Mainland analyzed by CMONOC GPS data from 2009–2013. Geodesy and Geodynamics, 5, 41-45.

Wen, D.R., Liu, D.Y., Chung, S.L., Chu, M.F., Ji, J.Q., Zhang, Q., Song, B., Lee, T.Y., Yeh, M.W., & Lo, C.H. (2008). Zircon SHRIMP U–Pb ages of the Gangdese Batholith and implications for Neotethyan subduction in southern Tibet. Chemical Geology, 252, 191-201.

Wilde, S.A. (2015). Final amalgamation of the Central Asian Orogenic Belt in NE China: Paleo-Asian Ocean closure versus Paleo-Pacific plate subduction-A review of the evidence. Tectonophysics, 662, 345–362.

Wilhem, C., Windley, B.F., & Stampfli, G.M. (2012). The Altaids of Central Asia: A Tectonic and Evolutionary Innovative Review. Earth-Science Review, 113, 303-341.

Windley, B.F., Alexeiev, D., Xiao, W., Kroner, A., & Badarch, G. (2007). Tectonic models for accretion of the Central Asian Orogenic Belt. Journal of the Geological Society, London, 164, 31-47.

Wu, T.R., He, G.Q., & Zhang, C. (1998). The Paleozoic evolution of the Alxaa region, Inner Mongolia. Acta Geologica Sinica, 72, 286(in Chinese).

Wu, F.P., Zhang, W.J., & Wang, W. (2012). Discovery of the NNE ductile shear zone and its deformation age analysis of Tamusu Area, Inner Mongolia. Xinjiang Geology, 30, 216-220 (in Chinese with English abstract).

Xiao, W.J., Windley, B.F., Hao, J., & Zhai., M.G. (2003). Accretion leading to collision and the Permian Solonker suture, Inner Mongolia, China: Termination of the Central Asian Orogenic Belt. Tectonics, 22, 1069–1090.

Xiao, W.J., Windley, B.F., Huang, B.C., Han, C.M., Yuan, C., Chen, H.L., Sun, M., Sun, S., & Li, J.L. (2009). End-Permian to mid-Triassic termination of the accretionary processes of the southern Altaids: implications for the geodynamic evolution, Phanerozoic continental growth, and metallogeny of Central Asia. International Journal of Earth Sciences, 98, 1189-1217.

Xiao, W.J., Huang, B.C., Han, C.M., Sun, S., & Li, J.L. (2010). A review of the western part of the Altaids: A key to understanding the architecture of accretionary orogens. Gondwana Research, 18, 253-273.

Xiao, W.J., Windley, B.F., Sun, S., Li, J.L., Huang, B.C., Han, C.M., Yuan, C., Sun, M., & Chen, H.L.

(2015). A Tale of Amalgamation of Three Permo-Triassic Collage Systems in Central Asia: Oroclines, Sutures, and Terminal Accretion. Annual Review of Earth and Planetary Sciences. 43, 16.1-16.31.

Xie, L., Yin, H.Q., Zhou, H.R., & Zhang, W.J. (2014). Permian radiolarians from the Engeerwusu suture zone in Alxa area of Inner Mongolia and its geological significance. Geological Bulletin of China, 33, 691-697 (in Chinese with English abstract).

Xu, B., Charvet, J., Chen, Y., Zhao, P., & Shi, G.Z. (2013). Middle Paleozoic convergent orogenic belts in western Inner Mongolia (China): framework, kinematics, geochronology and implications for tectonic evolution of the Central Asian Orogenic Belt. Gondwana Research, 23, 1342–1364.

Xu, X., Li, X., Ma, Z.P., Xia, L., & Xia, Z. (2006). LA-ICPMS zircon U-Pb dating of gabbro from the bayingou ophiolite in the Northern Tianshan Mountains. Acta Geologica Sinica, 80, 1168-1176 (in Chinese with English abstract)

Yang, Y.T., Guo, Z.X. Song, C.C., Li, X.B., & He, S. (2015), A short-lived but significant Mongol–Okhotsk collisional orogeny in latest Jurassic–earliest Cretaceous. Gondwana Research, 28, 1096-1116.

Ye, X.T., Zhang, C.L., Zou, H.B., Yao, C.Y., & Dong, Y.G. (2017). Age and geochemistry of the Zhaheba ophiolite complex in eastern Junggar of the Central Asian Orogenic Belt (CAOB): Implications for the accretion process of the Junggar terrane. Geological Magazine, 154, 419-440

Yin, A., Rumelhart, P.E., Butler, R., Cowgill, E., Harrison, T.M., Foster, D.A., Ingersoll, R.V., Zhang, Q., Zhou, X.Q., Wang, X.F., Hanson, A., & Raza, A. (2002). Tectonic history of the Altyn Tagh fault system in northern Tibet inferred from Cenozoic sedimentation. Geological Society of America Bulletin, 114, 1257-1295.

Yuan, W. & Yang, Z.Y. (2015). The Alashan Terrane did not amalgamate with North China block by the Late Permian: Evidence from Carboniferous and Permian paleomagnetic results. Journal of Asian Earth Sciences, 104, 145-159.

Yue, Y.J., & Liou, J.G. (1999). Two-stage evolution model for the Altyn Tagh fault, China. Geology, 27, 227-230.

Yue, Y., Liou, J., & Graham, S. (2001a). Tectonic correlation of Beishan and Inner Mongolia orogens and its implications for the palinspastic reconstruction of north China. Geological Society of America Memoir, 194, 101-116.

Yue, Y.J., Ritts, B.D., & Graham, S.A. (2001b). Initiation and long-term slip history of the Altyn Tagh fault. International Geology Review, 43, 1087-1093.

Zhang, Y.Q., Mercier, J.L., & Vergely, P. (1998). Extension in the graben systems around the Ordos (China), and its contribution to the extrusion tectonics of south China with respect to Gobi-Mongolia. Tectonophysics, 285, 41-75.

Zhang, Y.Q., & Su, H.W. (2002). U-Pb single zircon ages of metamorphic basic volcanic rocks of Baoyintu Rock Group in Inner Mongolia. Progress in Precambrian Research, 25, 199-204 (in Chinese with English abstract).

Zhang, Y.Q. (2004). Ages, tectonic environment and geological significance of metabasic volcanic rocks of the Buyant Group-complex in the north of Bayan Obo, Inner Mongolia. Geological Bulletin of China, 23, 177-183 (in Chinese with English abstract).

Zhang, J., Li, J.Y., Liu, J.F., & Feng, Q.W. (2011). Detrital zircon U–Pb ages of Middle Ordovician flysch sandstones in the western ordos margin: New constraints on their provenances, and tectonic implications. Journal of Asian Earth Sciences, 42, 1030-1047.

Zhang, J., & Cunningham, D. (2012). Kilometer-scale refolded folds caused by strike-slip reversal and intraplate shortening in the Beishan region, China. Tectonics, 31, TC3009, 1-19.

Zhang, J., Li, J.Y., Xiao, W.X., Wang, Y.N., & Qi, W.H. (2013a). Kinematics and geochronology of multistage ductile deformation along the eastern Alxa block, NW China: New constraints on the relationship between the North China Plate and the Alxa block. Journal of Structural Geology, 57, 38-57.

Zhang, J.X., Gong, J.H., Yu, S.Y., Li, H.K., & Hou, K.J. (2013b). Neoarchean-Paleoproterozoic multiple tectonothermal events in the western Alxa block, North China Craton and their geological implication: Evidence from zircon U–Pb ages and Hf isotopic composition. Precambrian Research, 235, 36-57.

Zhang, J., Li, J.Y., Liu, J.F., Qu, J.F., Zhang, Y.P. (2013c). LA-ICP-MS U-Pb ages of pillow lava basalts in southwestern Langshan, Inner Mngolia and their implication. Geological Bulletin of China, 32, 287-296 (in Chinese with English abstract).

Zhang, W., Wu, T.R., Feng, J.C., Zheng, R.G., & He, Y.K. (2013d). Time constraints for the closing of the Paleo-Asian Ocean in the Northern Alxa Region: evidence fromWuliji granites. Science China: Earth Sciences, 56, 153-164.

Zhang, J., Li, J.Y., Li, Y.F., Qi, W.H., & Zhang, Y.P. (2014). Mesozoic-Cenozoic Multi-Stage Intraplate Deformation Events in the Langshan Region and their Tectonic Implications. Acta Geologica Sinica (English Edition), 88, 78-102.

Zhang, J., Zhang, Y.P., Xiao, W.X., & Wang, Y.N. (2015). Linking the Alxa Terrane to the eastern Gondwana during the Early Paleozoic: Constraints from detrital zircon U–Pb ages and Cambrian sedimentary records. Gondwana Research, 28, 1168-1182.

Zhang, J., Zhang, B.H., & Zhao, H. (2016a). Timing of amalgamation of the Alxa Block and the North China Block: Constraints based on detrital zircon U-Pb ages and sedimentologic and structural evidence. Tectonophysics, 668, 65-81.

Zhang, W., Pease, V., Meng, Q.P., Zheng, R.G., Thomsen, T.B., Wohlgemuth-Ueberwasser, C., & Wu, T.R. (2016b). Discovery of a Neoproterozoic granite in the Northern Alxa region, NW China: its age, petrogenesis and tectonic significance. Geological Magazine, 153, 512-523.

Zhang, B.H. (2019). The Paleozoic tectonic attribute of the Southern Alxa Block: Constrained by detrital zircon U-Pb ages and structural deformation analysis. p.1-165 (Doctoral dissertation), Beijing: Chinese Academy of Geological Sciences (in Chinese with English abstract).

Zhang, J., Qu, J.F., Zhang, B.H., Zhao, H., Niu, P.F., Zhao, S., Hui, J., Yun, L., Nie, F.J., & Wang, Y.N. (2020). Mesozoic intraplate deformation of the North China Craton: characteristics, timing, mechanism and tectonic settings. Journal of Asian Earth Sciences, 192, https://doi.org/10.1016/j.jseaes.2020.104269.

Zhao, G.C., Sun, M., Wilde, S.A., & Li, S.Z. (2005). Late Archean to Paleoproterozoic evolution of the North China Craton: key issues revisited. Precambrian Research, 136, 177-202.

Zhao, P., Y. Chen, B. Xu, M. Faure, Shi, G., & Choulet, F. (2013). Did the Paleo-Asian Ocean between North China Block and Mongolia Block exist during the late Paleozoic? First paleomagnetic evidence from central-eastern Inner Mongolia, China. Journal of Geophysical Research (Solid Earth), 118, 1873–1894.

Zhao, P., Faure, M., Chen, Y., Shi, G.Z., & Xu, B. (2015). A new Triassic shortening-extrusion tectonic model for Central-Eastern Asia: Structural, geochronological and paleomagnetic investigations in the Xilamulun Fault (North China). Earth and Planetary Science Letters, 426, 46-57.

Zhao, P., Xu, B., Tong, Q.L., Chen, Y., & Faure, M. (2016). Sedimentological and geochronological constraints on the Carboniferous evolution of central Inner Mongolia, southeastern Central Asian

Orogenic Belt: Inland sea deposition in a post-orogenic setting. Gondwana Research, 31, 253–270.
Zhao, B., Zhang, C., Wang, D., Huang, Y., Tan, K., Du, R., & Liu, J. (2017). Contemporary kinematics of the Ordos block, North China and its adjacent rift systems constrained by dense GPS observations. Journal of Asian Earth Sciences, 135, 257-267.
Zhao, G.C., Wang, Y.J., Huang, B.C., Dong, Y.P., Li, S.Z., Zhang, G.W., & Yu, S. (2018). Geological reconstructions of the East Asian blocks: From the breakup of Rodinia to the assembly of Pangea. Earth-Science Reviews, 186, 262–286.
Zhao, H., Zhang, J., Qu, J.F., Zhang, B.H., Niu, P.F., Hui, J., Yun, L., Li, Y.F., Wang, Y.N., & Zhang, Y.P. (2020). Characteristics and dynamic background of the Cenozoic compressive structures in the eastern margin of the Alxa Block. Earth Science, 45, doi:10.3799/dqkx.2019.126 (in Chinese with English abstract).
Zheng, R.G., Wu, T.R., Zhang, W., Xu, C., Meng, Q.P., & Zhang, Z.Y. (2014). Late Paleozoic subduction system in the northern margin of the Alxa block, Altaids: Geochronological and geochemical evidences from ophiolites. Gondwana Research, 25, 842-858.
Zheng, R.G., Li, J.Y., Xiao, W.J., Wang, L.J. (2018). A new ophiolitic mélange containing boninitic blocks in Alxa region: Implications for Permian subduction events in southern CAOB. Geoscience Frontiers, 9, 1355-1367.
Zheng, D.W., Zhang, P.Z., Wan, J.L., Yuan, D.Y., Li, C.Y., Yin, G.M., Zhang, G.L., Wang, Z. C., Min, W., & Chen, J. (2006). Rapid exhumation at 8 Ma on the Liupan Shan thrust fault from apatite fission-track thermochronology: implications for growth of the northeastern Tibetan Plateau margin. Earth and Planetary Science Letters, 248, 198-208.
Zheng, Y., Zhang, Q., Wang, Y., Liu, R., Wang, S.G., Zuo, G., Wang, S.Z., Lkaasuren, B., Badarch, G., & Badamgarav, Z. (1996). Great Jurassic thrust sheets in Beishan (North Mountains)–Gobi areas of China and southern Mongolia. Journal of Structural Geology, 18, 1111-1126.
Zhuang, G.S., Hourigan, J.K., Ritts, B.D., & Kent-Corson, M.L. (2011). Cenozoic multiple-phase tectonic evolution of the northern Tibetan Plateau: Constraints from sedimentary records from Qaidam basin, Hexi Corridor, and Subei basin, northwest China. American Journal of Science, 311, 116-152.
Zorin, Y. A. (1999). Geodynamics of the western part of the Mongolia-Okhotsk collisional belt, Trans-Baikal region (Russia) and Mongolia. Tectonophysics, 306, 33-56.

Figure captions

Fig. 1 Map of the Alxa Block and surrounding tectonic regions of northern China. Locations of Figs. 2 and 3 are also indicated. A. Location of the study area (rectangular box) in the context of major Asian cratons and smaller basement blocks. B. Physiographic map of the northern-central China region showing the locations of the Langshan and Helanshan study areas. Historical earthquake epicenters from Liu et al. (2016) and GPS vectors from Wei et al. (2014). C. Geological map of the study region. HG: Hetao Graben; DQS: Daqing Shan; DS: Dabashan; BS: Bayanwulashan; YS: Yabrai Shan; ZS: Zhuozishan; YG: Yinchuan Graben; WS: Weiningbeishan; XS: Xiangshan; LS: Liupan Shan; TS: Taihangshan.

Fig. 2 A. Geological map of the eastern Alxa Block. Yellow stars indicate the piercing points of the boundary between the Langshan Group and Permian granite.

Fig. 3 Geological map and cross-section of the Langshan region (1:25,000) and stratigraphic column of the Langshan Group; cross sections are shown in Fig. 4. Section c-c' shown in Fig. 8, d-d' in Fig. 14 and e-e' in Fig. 15.

Fig. 4 Tectonic division of the Langshan region, stereoplots of structural data and two geological cross-sections. I = Domain I. II = Domain II. III = Domain III. IV = Domain IV. The stereographic projections represent the major structures in the 4 major structural domains (lower hemisphere, equal area projections apply for all stereoplots in this paper). (a) Early late Paleozoic mylonitic foliations in the Langshan Group (n=68) and quartz stretching lineations (n=127, pink dots). (b) Poles to earlier late Paleozoic mylonitic foliation in the Langshan Group (n=68, blue dots) and fold hinges of the Langshan Group (black; n=193); the red square is the π axis of the mylonitic foliations. (c) Late Jurassic east-west-striking mylonitic foliations in the Langshan Group (n=65) and quartz stretching lineations (n=118, pink dots). (d) Fold hinges of the Langshan Group (n=193). (e) Poles to foliations of the Diebusige Complex (n=591); the red square is the π axis of foliations. (f) Fold hinges of the Diebusige Complex (n=38). (g) Poles to foliations/beddings of the Langshan Group (n=824). (h) Foliations of the Triassic mylonite (n=279) and quartz stretching lineations (n=553, pink dots). (i) Poles to Triassic mylonitic foliation (n=279, blue dots) and quartz stretching lineations (pink dots, n=553); the red square is the π axis of mylonitic foliations. (j) Fold hinges of Triassic granitic mylonite (n=22).

Fig. 5 Simplified geological map plotted on shaded relief map of Langshan region study area showing subhorizontal shortening or extension directions determined from fault data.

Fig. 6 Zircon U-Pb ages of samples from the mapped region. Detailed analytical data shown in Table 1.

Fig. 7 The first-stage deformation in the Langshan Group. A. Asymmetric structures of quartz vein boudins (XZ plane of strain ellipsoid shown, indicating sinistral shearing). B. Mica fish (XZ plane perspective, indicating sinistral shearing).

Fig. 8 Folds in the Langshan Group that formed in the second stage. A. Isoclinal fold of a granite dike (the star indicates the location of sample LS-16-3, 258.3±1.6). B. SE-vergent folds of thin-bedded sandstones within thick-bedded limestone of the Second Formation (hat in the circle for scale). C. Cleavage parallel to the axial surface in the Fourth Formation, black arrow indicates the plunge of fold hinge, white dash line indicates the bedding of sandstone. D. Cleavages caused by interlayer shearing in the Fourth

Formation. E. A cross-section showing detailed deformation characteristics of the Langshan Group in Domain I; see Fig. 3 for section c-c' location.

Fig. 9 Folds in the Langshan Group in Domain II. A. One folded granite dike intruding the Langshan Group and the sample location. B. A recumbent fold in sandstones of the Langshan Group.

Fig. 10 Structural features in the First Formation of the Langshan Group. A. Refolded folds in schist and the stereographic projection of fold hinges. B. Lineation of stretched pebbles in conglomerates and the stereographic projection of the stretched pebbles (blue) and quartz stretching lineation (pink). C. Small southeast-verging folds in thin-layered sandstone and siltstone. D. Small folds in thin-layered limestone.

Fig. 11 Field photos of structures associated with the boundary between the Second Formation of the Langshan Group in Domain I and the Permian granite in Domain II. A. Permian granitic mylonite (east) and the Langshan Group (west); (insets: quartz stretching lineations on foliations of granitic mylonite; the star indicates the location of Sample D15719-2, 258.9±1.3 Ma, and oblique normal fault between sandstone in the Second Formation and mylonite (hammer in circle for scale). B. δ-type feldspar porphyroclast in the XZ plane, indicating dextral shearing, feldspar is also dynamically recrystallized along grain margins, black great circles in the stereographic projection are mylonitic foliations, blue spots are quartz stretching lineations, blue great circles are later dextral transtensional faults, and red points are slickenlines of the dextral transtensional faults.

Fig. 12 East-west-trending shear zone and younger brittle fault in the Diebusige Complex. A. Mylonitized granite showing significant grain size comminution and reduction and asymmetric structures indicating dextral shearing (cross-polarized light) and stereographic projections of mylonitic foliations (red great circles) and quartz stretching lineations (blue dots). B. Dextral brittle fault zone overprinting older mylonite (hammer in the circle for scale).

Fig. 13 Deformation of magmatic dikes intruding the Langshan Group in Domain I. A. Cleavage in a granite dike. B. Crenulation cleavage in diorite dike.

Fig. 14 Deformation characteristics of the Diebusige Complex. A. Felsic mylonite showing quartz stretching lineation; stereographic projection of mylonitic foliations (great circles) and lineations (red dots). B. Folded felsic mylonite (measured fold axes are indicated by

pink dots). C. A southeast-trending section of the deformed Diebusige Complex; see Fig. 3 for the section location.

Fig. 15 Brittle top-to-the-southeast thrust faults. A. Thrust stack with internal duplex-like fault geometry and fan structure between the Third and Second Formations of the Langshan Group (yellow star indicates location of Sample D1151-1). B. Thrust between Proterozoic gneiss of the Diebusige Complex and carbonaceous shale of the Middle Jurassic Yanan Formation and the fault plane solution of the thrust. C. Cross-section showing imbricated thrust faults in the Diebusige Complex and Middle Jurassic Yanan Formation (see Fig. 3 for section location).

Fig. 16 Views looking NE of an early Cretaceous low-angle detachment fault in the Diebusige Basin. A. Close view. B. Distant view.

Fig. 17 Nearly north-south-trending sinistral faults in Domains I and III (**Dl-5**). A. Steep canyon along the **Dl-5** brittle fault zone and fault plane solution for the north-south-trending faults (Domain I). B. Fault core breccia in the **Dl-5** brittle fault zone (Domain I) (geologist in circle for scale). Blue great circles in the stereographic projection are fault planes, and yellow arrows indicate hanging wall movement directions. C. Fault in Lower Cretaceous sandstones (Domain III).

Fig. 18 Boundary fault between Domains II and III. A. Thick fault breccias (jeep in circle for scale); the blue great circles in the stereographic projection are fault planes, red arrows indicate the movement direction of the hanging wall, along with the fault plane solutions. B. Dextrally offset diabase dike and its fault plane solution.

Fig. 19 Northeast-southwest-trending sinistral strike-slip faults in the Diebusige Basin. A. Fault-controlled valley with sinistrally offset gneiss. B Three sets of slickenlines on the fault plane; white arrows indicate slickenlines associated with the youngest normal faults, yellow arrows indicate slickenlines associated with the oldest sinistral movement, and blue arrows indicate slickenlines associated with older dextral movement, with the fault plane solutions shown in the inset. C. Strike-slip fault cutting the Early Cretaceous conglomerates in the supradetachment basin in Domain III.

Fig. 20 Strike-slip faults and Cenozoic red beds in Domain IV. A. The Wulanbulage Formation on top of the Langshan Group (inset: fault valley in the central part of the Carboniferous granite; a blue map holder for scale). B. Northeast-southwest-trending sinistral strike-slip fault in the granitic mylonite overlain by the Wulanbulage Formation.

Fig. 21 Cenozoic thrust fault in the Diebusige Basin and fault plane solutions. Circled hammer for scale and stereographic projection of thrust faults.

Fig. 22 Mid-Cenozoic thrusts in the southeastern foothills of Langshan. A. Westward-directed thrust of Carboniferous granite over the Wulanbulage Formation. B. Carboniferous granite thrust westwards over the Cretaceous conglomerate. C. Cross-section showing imbricated thrust faults (GPS of the section is indicated in figure).

Fig. 23 Cenozoic faults along the Langshan range front. A. DigitalGlobe satellite image of the Dabashan footwall block looking NE. Locations of inset photos indicated in the figure. B. Close-up views of active high-angle normal faults.

Fig. 24 Tectonic evolution of the Alxa Block between the late Paleozoic and the Triassic. See Sections 7.2 – 7.4 for explanation. Different block colors indicate different paleogeographic and tectonic affinities: pink = Gondwana-related, gray = Siberian Craton-related, brown = no confirmed affinity. Locations of main cratons and blocks are adapted from Wilhem et al.(2012), Zhao P. et al. (2013), Huang et al. (2018), and Zhao G.C. et al. (2018).

Fig. 25 Evolutionary stages and inferred tectonic settings of eastern-central Asia during the late Mesozoic and Cenozoic. Note that during the Late Cretaceous and Paleogene, the N-S boundary between the Alxa Block and the Ordos Block (inset cartoon) experienced a reversal in shear sense driven by changes in distant plate boundary dynamics.

Table 1 LA-ICP-MS zircon U-Pb results for the samples

Table 2 Main structures, tectonic events, ages and tectonic settings of different domains in the Langshan region

SFig. 1 Representative images of the dated zircons from all samples (openly available in figshare at http://doi.org/10.6084/m9.figshare.12127176).

Figure 1.

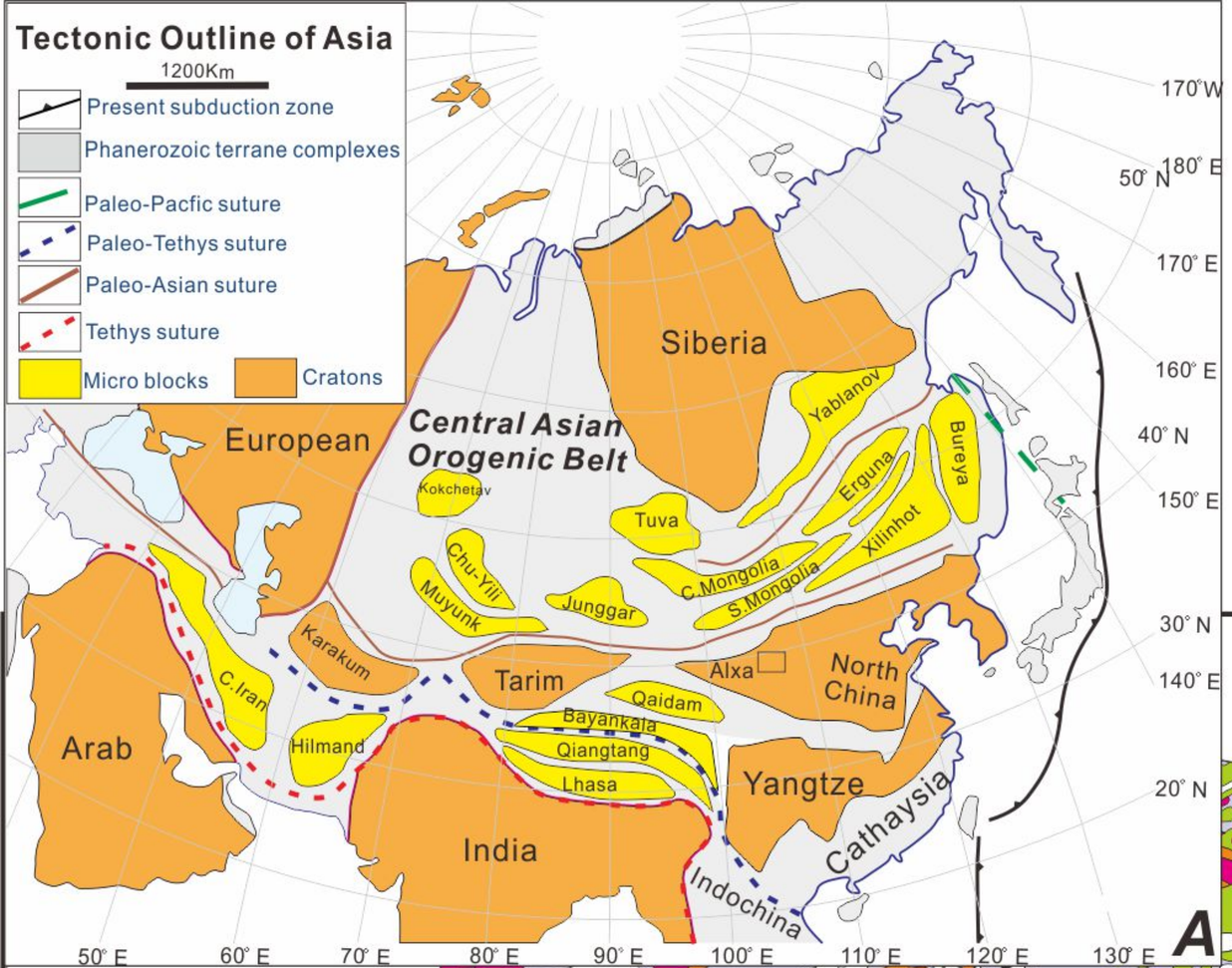
Tectonic Outline of Asia
1200Km
Present subduction zone
Phanerozoic terrane complexes
Paleo-Pacfic suture
Paleo-Tethys suture
Paleo-Asian suture
Tethys suture
Micro blocks
Cratons
Siberia
European
Central Asian Orogenic Belt
Kokchetav
Yablanov
Erguna
Bureya
Tuva
Xilinhot
Chu-Yili
Muyunk
Junggar
C.Mongolia
S.Mongolia
Karakum
C.Iran
Tarim
Alxa
North China
Qaidam
Bayankala
Qiangtang
Lhasa
Hilmand
Arab
Yangtze
India
Cathaysia
Indochina
50° N
30° N
20° N
40° N
170°W
180° E
170° E
160° E
150° E
140° E
50° E
60° E
70° E
80° E
90° E
100° E
110° E
120° E
130° E
A

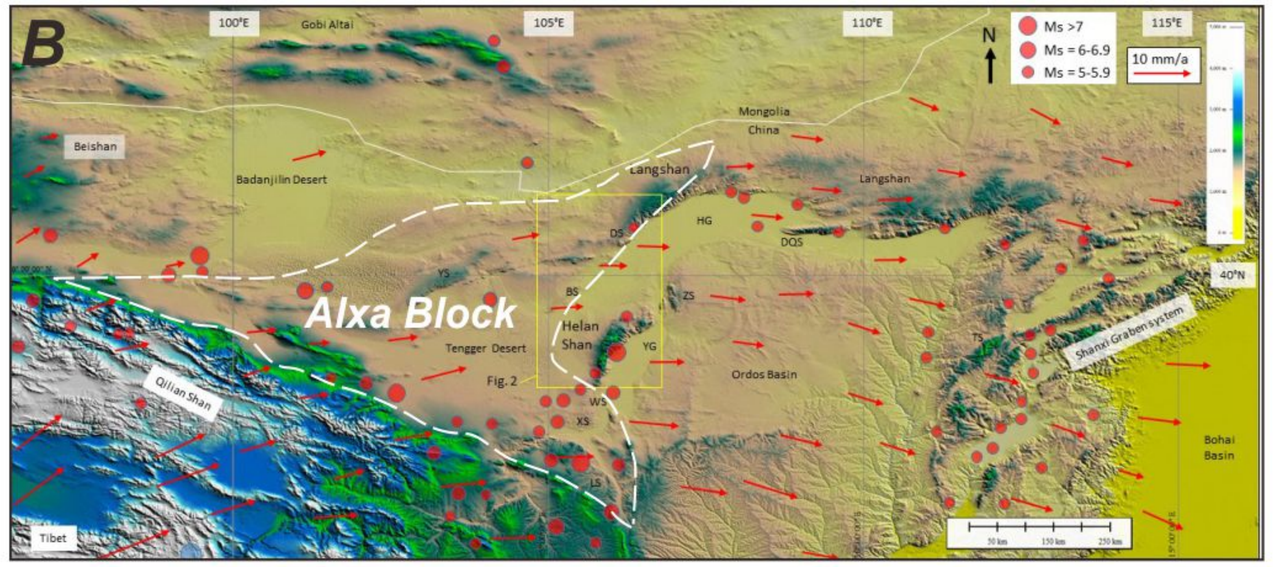
B
100°E
Gobi Altai
105°E
110°E
115°E
N
Ms >7
Ms = 6-6.9
Ms = 5-5.9
10 mm/a
Beishan
Mongolia
China
Badanjilin Desert
Langshan
HG
DS
DQS
YS
BS
ZS
Alxa Block
Helan Shan
YG
Tengger Desert
Fig. 2
Qilian Shan
WS
XS
LS
Ordos Basin
Shanxi Grabensystem
Bohai Basin
Tibet
40°N

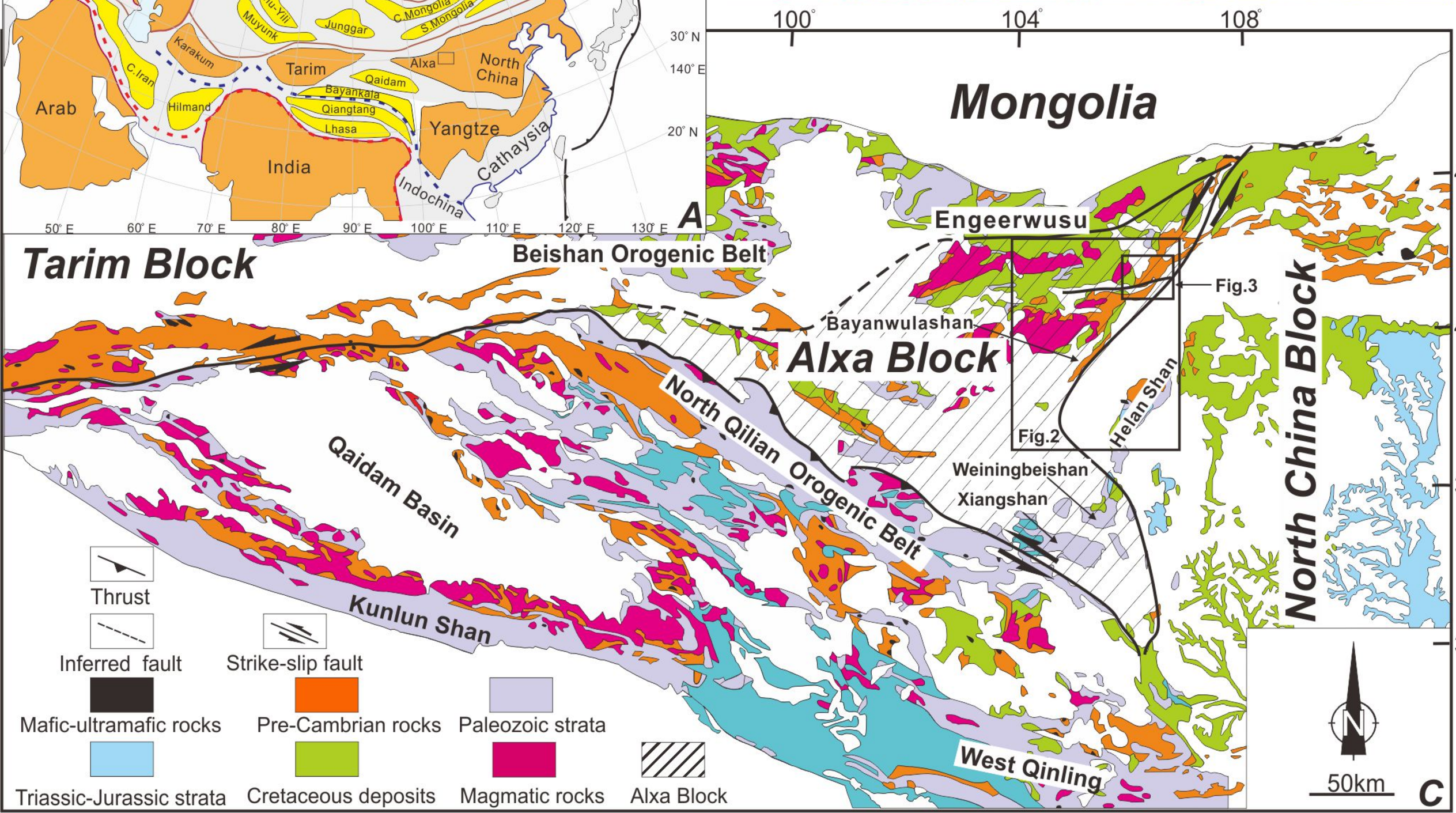
100°
104°
108°
Mongolia
42°
40°
38°
36°
Engeerwusu
Fig.3
Bayanwulashan
Alxa Block
Helan Shan
Fig.2
Weiningbeishan
Xiangshan
North China Block
Beishan Orogenic Belt
Tarim Block
North Qilian Orogenic Belt
Qaidam Basin
Kunlun Shan
West Qinling
Thrust
Inferred fault
Strike-slip fault
Mafic-ultramafic rocks
Pre-Cambrian rocks
Paleozoic strata
Triassic-Jurassic strata
Cretaceous deposits
Magmatic rocks
Alxa Block
N
50km
C

Figure 2.

Legend

- Triassic granite
- Permian granite
- Mylonitized Permian granite
- Permian gabbro
- Devonian-Carboniferous granite
- Neoproterozoic diorite
- Mylonitized Paleo-Meso proterozoic metamorphic rocks
- Paleo-Mesoproterozoic Metamorphic rocks
- No.4 Fm. Of Neoproterozoic Langshan Gp.
- No.3 Fm. of Neoproterozoic Langshan Gp.
- No.2 Fm. of Neoproterozoic Langshan Gp.
- No.1 Fm. of Neoproterozoic Langshan Gp.
- Late Paleozoic volcanic rocks

Langshan

277 ±3 Ma
(Dan et al., 2014)

~82 km

Permian granite

~45 km

~10 km

~20 km

Fig.3

344 ±5 Ma
(Dan et al., 2016)

269 ±2 Ma
(Dan et al., 2014)

276 ±2 Ma
(Dan et al., 2014)

284 ±3 Ma
(Dan et al., 2014b)

278±2 Ma
(Dan et al., 2014b)

Hetao Graben

Bayanwula Shan

345 ±4 Ma
(Dan et al., 2016)

Zhengyiguan Fault

Helan Shan

Alxa Block

30 km

- Jurassic strata
- Triassic strata
- Permian strata
- Carboniferous strata
- Ordovician strata
- Cambrian strata
- Cenozoic strata
- Cretaceous strata
- Sinistral strike-slip fault
- Dextral strike-slip fault
- Thrust

41°20′
41°00′
40°40′
40°20′
40°00′
39°40′
39°20′
39°00′
38°40′
104°30′
105°00′
105°30′
106°00′
106°30′
107°00′

Figure 3.

106° 07′ 30″E
106° 15′ 00″E
106° 22′ 30″E
40° 40′N
40° 35′N
40° 30′N

a
a′
b
b′
c
c′
d
d′
e
e′
Fig. 8E
I
II
III
IV
Djebusige Basin
Dabashan
Hetao Basin
N
0
4km
A

Cenozoic fault (D8-10)
Late Cretaceous fault (D7)
Early Cretaceous fault (D6)
Late Jurassic fault (D5)
Late Triassic shear zone(D4)
End Permian shear zone(D3)
Late Devonian shear zone (D1)

Legend

3000
2000
1000
0m
The Fourth Formation
The Third Formation
The Second Formation
The First Formation

B

Quartzose sandstone
Mica-quartz schist
Marble
Carbonaceous slate
Phyllite
Slate

Strike and dip of foliation, and trend, plunge of lineation
Strike and dip of gneissosity
High-angle normal fault and trend and plunge of slickenline
Thrust and trend and plunge of slickenline
Low-angle detachment and trend and plunge of slickenline
Strike and dip of bedding
Overturned strata
Mineral stretching lineation and plunge angle
Dextral strike-slip fault, trend andplunge of slickenline
Mylonite
Fault breccia
Sinistral strike-slip fault
Dextral strike-slip fault
Thrust fault
Low-angle detachment fault
High-angle normal fault
Inferred fault

Syncline
Anticline
Overturned anticline
Overturned syncline
Anticline and the plunge angle of hinge
Syncline and the plunge angle of hinge
Z type fold and the plunge angle of hinge
S type fold and plunge angle of hinge
M type fold and plunge angle of hinge
Sinistral strike-slip fault, dip angle and plunge angle of slickenline

iron ore layer (body)
Diopside marble
Coarse grained quartzite
Medium grained and thick-bedded quartzite
Medium grained and thin-bedded quartzite
Sandy and carbonaceous slate
Migmatized biotite plagioclase gneiss
Plagioclase amphibolite gneiss
Coarse calcareous sandstone
Limestone
Thick-bedded quartzite

Diabase
Quartz vein
Triassic syenogranite
Late Permian pillow lava
Permian biotite granite
Carboniferous monzonitic granite
Early Paleozoic diorite
Late Paleozoic gabbro
Neoproterozoic gabbro
Oligocene Sikouzi Fm.
Early Cretaceous Dashuigou Fm.
Middle Jurassic Yanan Fm.
Late Triassic Yanchang Fm.

Langshan Group
Fourth Formation
Third Formation
Second Formation
First Formation
Baoyintu Group
Diebusige Complex

Figure 4.

106°07′30″E
106°15′00″E
106°22′30″E
40°40′N
40°35′N
40°30′N
b
a
Baoyintu Gp.
Langshan Gp.
I
II
Late Paleozoic magmatic rocks
Shengen Basin
N
a′
Diebusige Complex
Diebusige Basin
III
IV
Dabashan
Hetao Basin
b′
0
4km

(a) (b) (c) (d) (e)
(f) (g) (h) (i) (j)

a
a′
I
II
III
Dabashan
Hetao Basin
0 2 km
b
灰岩
I
II
III
Diebusige Basin
Dabashan
IV
磁铁矿
b′
0 2 km

Figure 5.

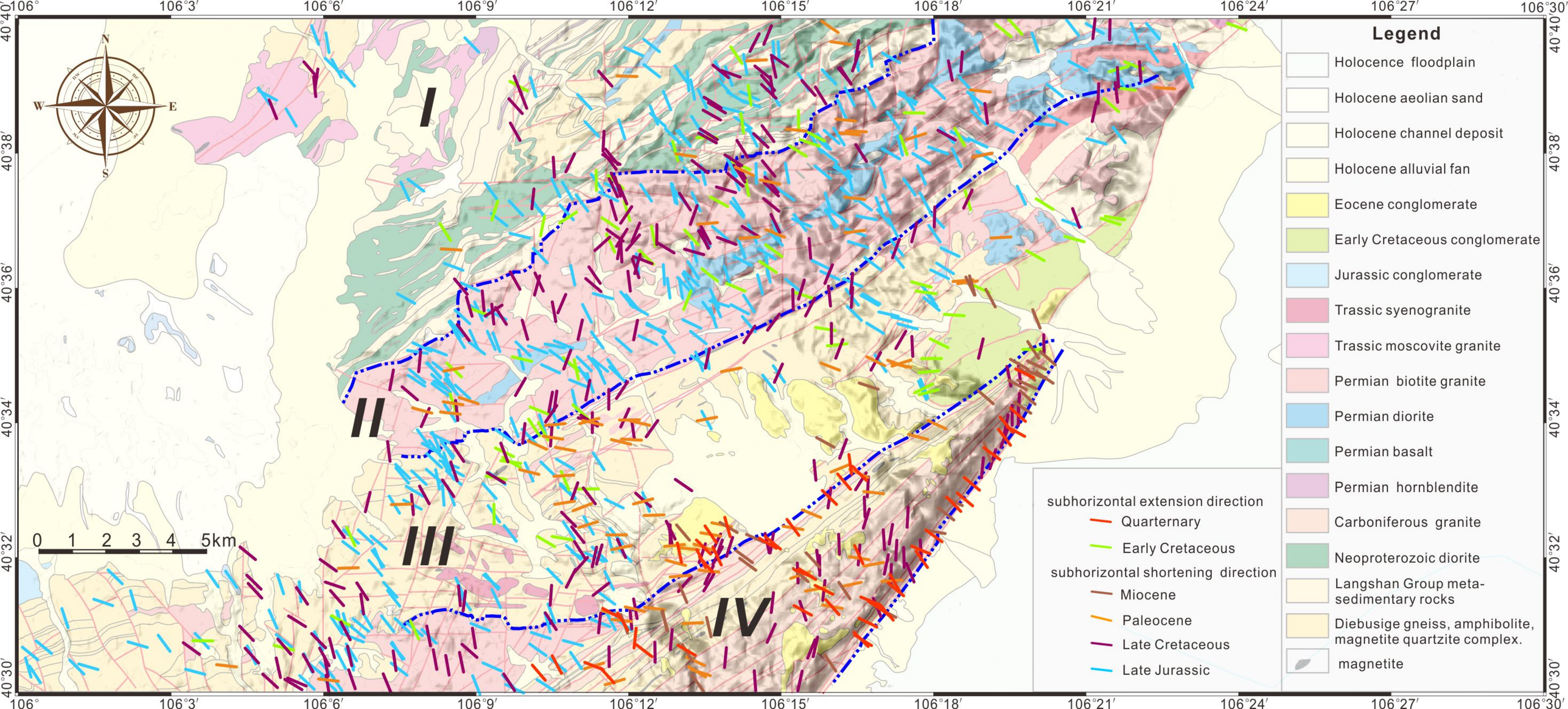
106°
106°3′
106°6′
106°9′
106°12′
106°15′
106°18′
106°21′
106°24′
106°27′
106°30′
40°40′
40°38′
40°36′
40°34′
40°32′
40°30′
N
W
E
S
I
II
III
IV
0 1 2 3 4 5km
Legend
Holocence floodplain
Holocene aeolian sand
Holocene channel deposit
Holocene alluvial fan
Eocene conglomerate
Early Cretaceous conglomerate
Jurassic conglomerate
Trassic syenogranite
Trassic moscovite granite
Permian biotite granite
Permian diorite
Permian basalt
Permian hornblendite
Carboniferous granite
Neoproterozoic diorite
Langshan Group meta-sedimentary rocks
Diebusige gneiss, amphibolite, magnetite quartzite complex.
magnetite
subhorizontal extension direction
Quarternary
Early Cretaceous
subhorizontal shortening direction
Miocene
Paleocene
Late Cretaceous
Late Jurassic

Figure 6.

Data-point error ellipses are 68.3% conf.

LS-16-3

Mean = 258.3±1.6 [0.61%] 95% conf.
Wtd by data-pt errs only, 0 of 46 rej.
MSWD = 0.31, probability = 1.000

D1148-1

Mean = 840.0±8.0 [0.96%] 95% conf.
Wtd by data-pt errs only, 0 of 18 rej.
MSWD = 0.018, probability = 1.000

D15739-1

Mean = 259.6±1.3 [0.49%] 95% conf.
Wtd by data-pt errs only, 0 of 25 rej.
MSWD = 0.017, probability = 1.000

D15109-1

Mean = 257.6±1.1 [0.43%] 95% conf.Wtd by data-pt errs only, 0 of 23 rej.MSWD = 0.44, probability = 0.99

D15719-2

Mean = 258.9±1.3 [0.49%] 95% conf.
Wtd by data-pt errs only, 0 of 22 rej.
MSWD = 0.23, probability = 1.000

LS-14-3

Mean = 1834±17 [0.94%] 95% conf.
Wtd by data-pt errs only, 0 of 29 rej.
MSWD = 3.0, probability = 0.000

D15090-1

Mean = 263.7±1.9 [0.73%] 95% conf.
Wtd by data-pt errs only, 0 of 28 rej.
MSWD = 0.037, probability = 1.000

D15040-1

Mean = 259.4±1.3 [0.50%] 95% conf.
Wtd by data-pt errs only, 0 of 20 rej.
MSWD = 1.06, probability = 0.38

LS-14-1

Mean = 344.7±1.2 [0.35%] 95% conf.
Wtd by data-pt errs only, 0 of 38 rej.
MSWD = 0.30, probability = 1.000

D15729-1

Mean = 272.2±2.3 [0.83%] 95% conf.
Wtd by data-pt errs only, 0 of 11 rej.
MSWD = 0.022, probability = 1.000

$^{206}Pb/^{238}U$

$^{207}Pb/^{235}U$

Figure 7.


20
A

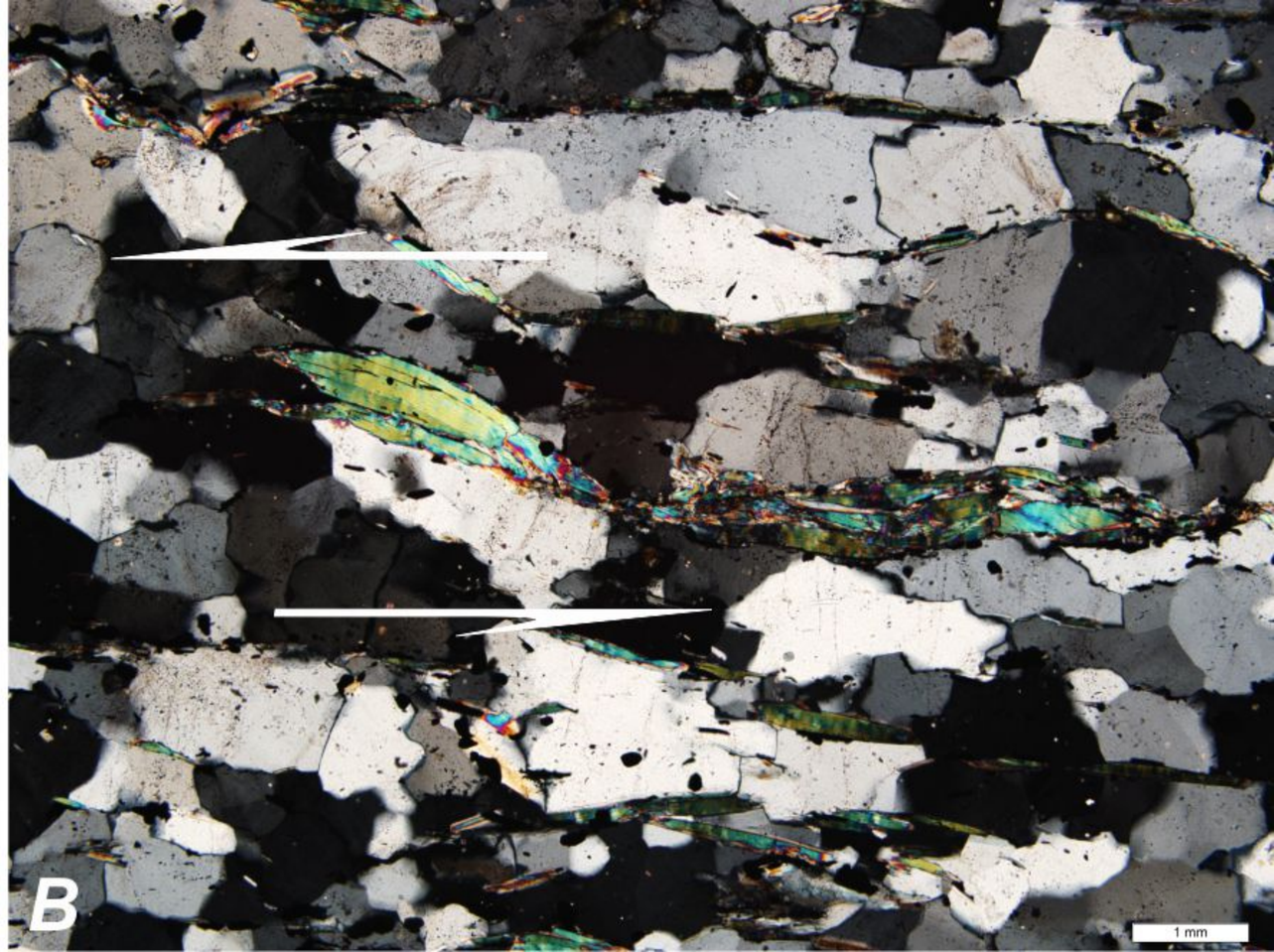
B
1 mm

Figure 8.


LS-16-3
2016/08/24 12:43
1.5m
A


310°
2015/08/07 16:07
B


20°
Hinge
2016/07/22
C


230°
2016/07/22 16:31
D

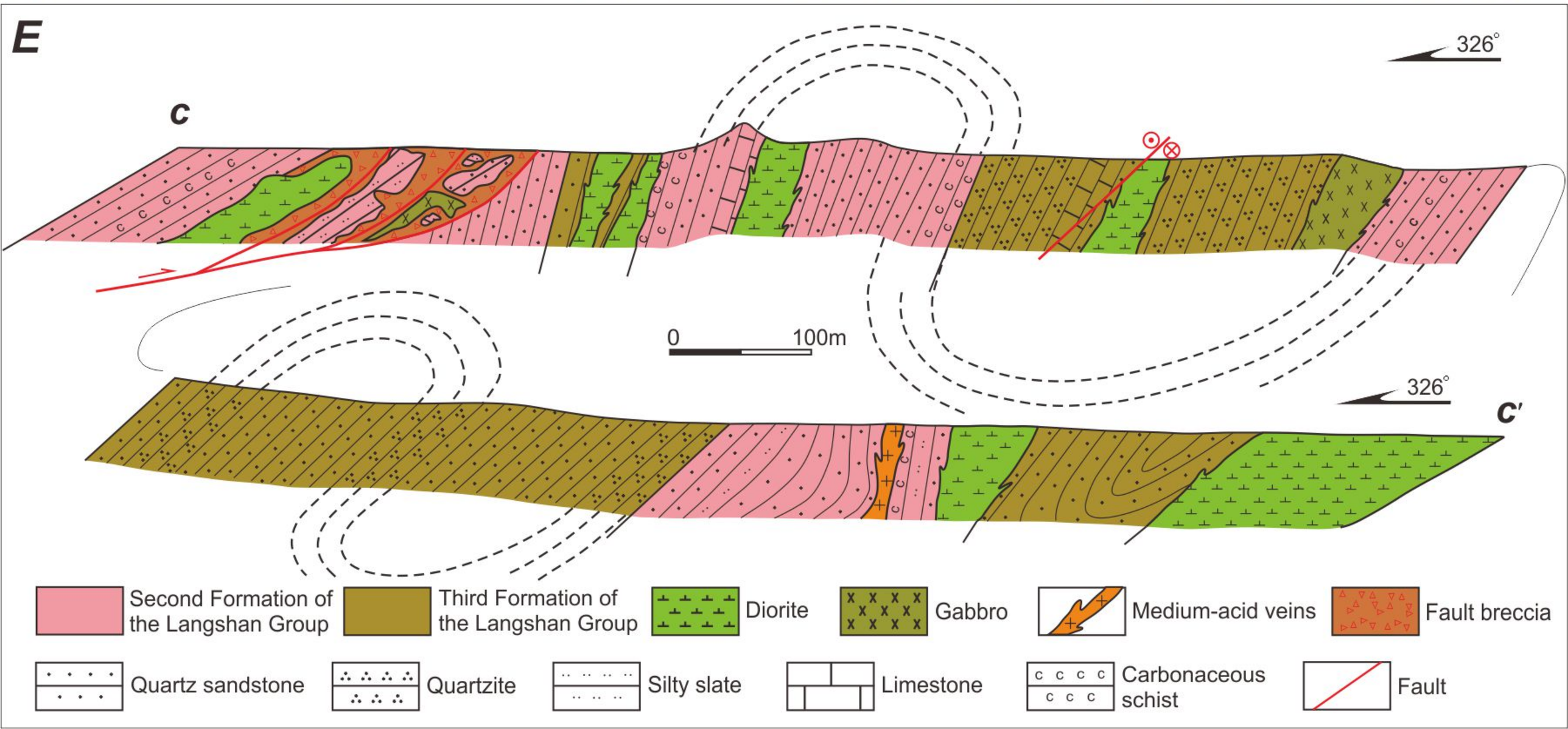
E
c
326°
0
100m
326°
c'
Second Formation of the Langshan Group
Third Formation of the Langshan Group
Diorite
Gabbro
Medium-acid veins
Fault breccia
Quartz sandstone
Quartzite
Silty slate
Limestone
Carbonaceous schist
Fault

Figure 9.


120°
Langshan Gp.
D15040-1
Granite dike
2015/08/01 15:57
A
80°
Langshan Gp.
2015/07/20 17:52
1m
B

Figure 10.

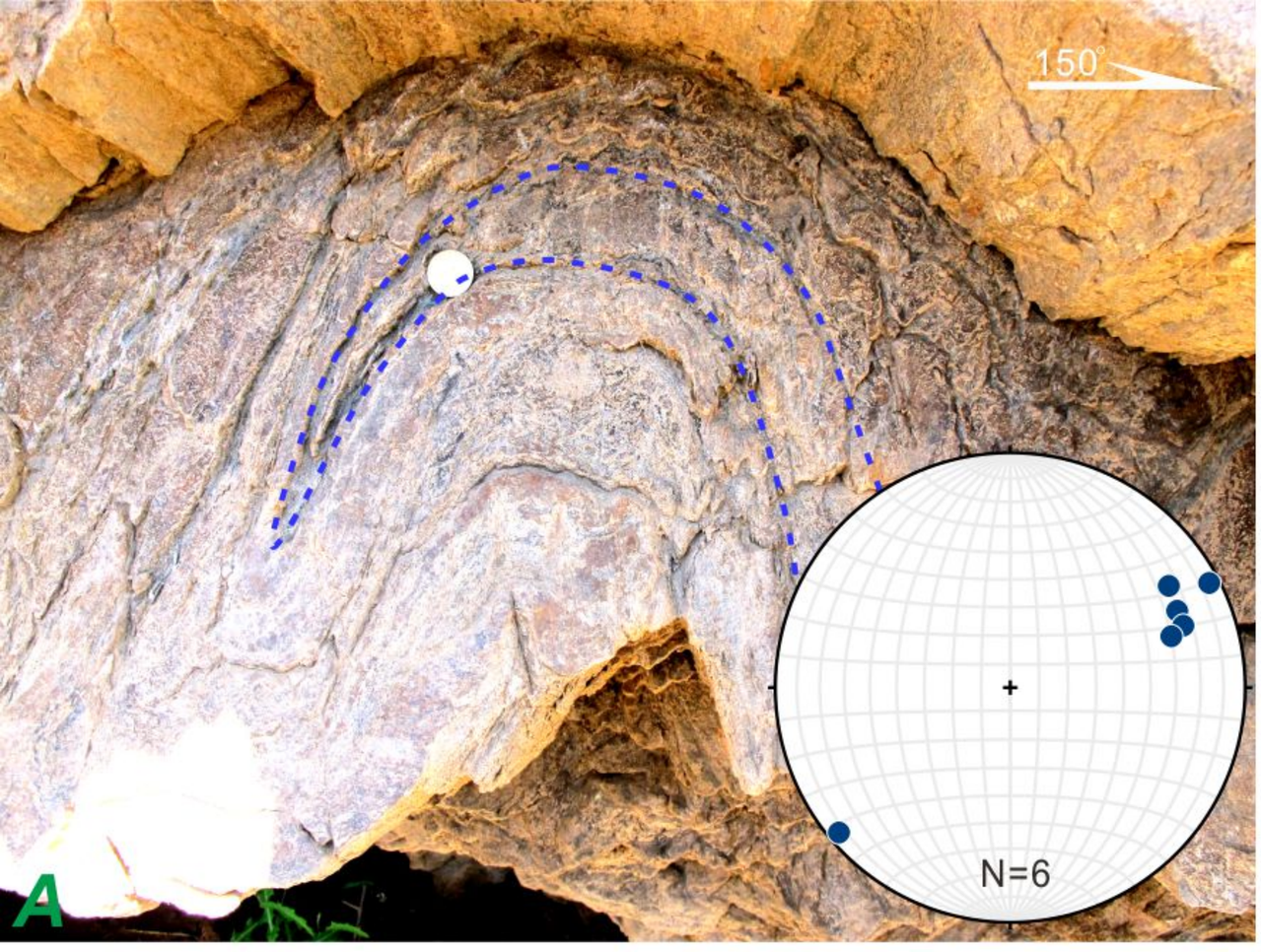
150°
N=6
A

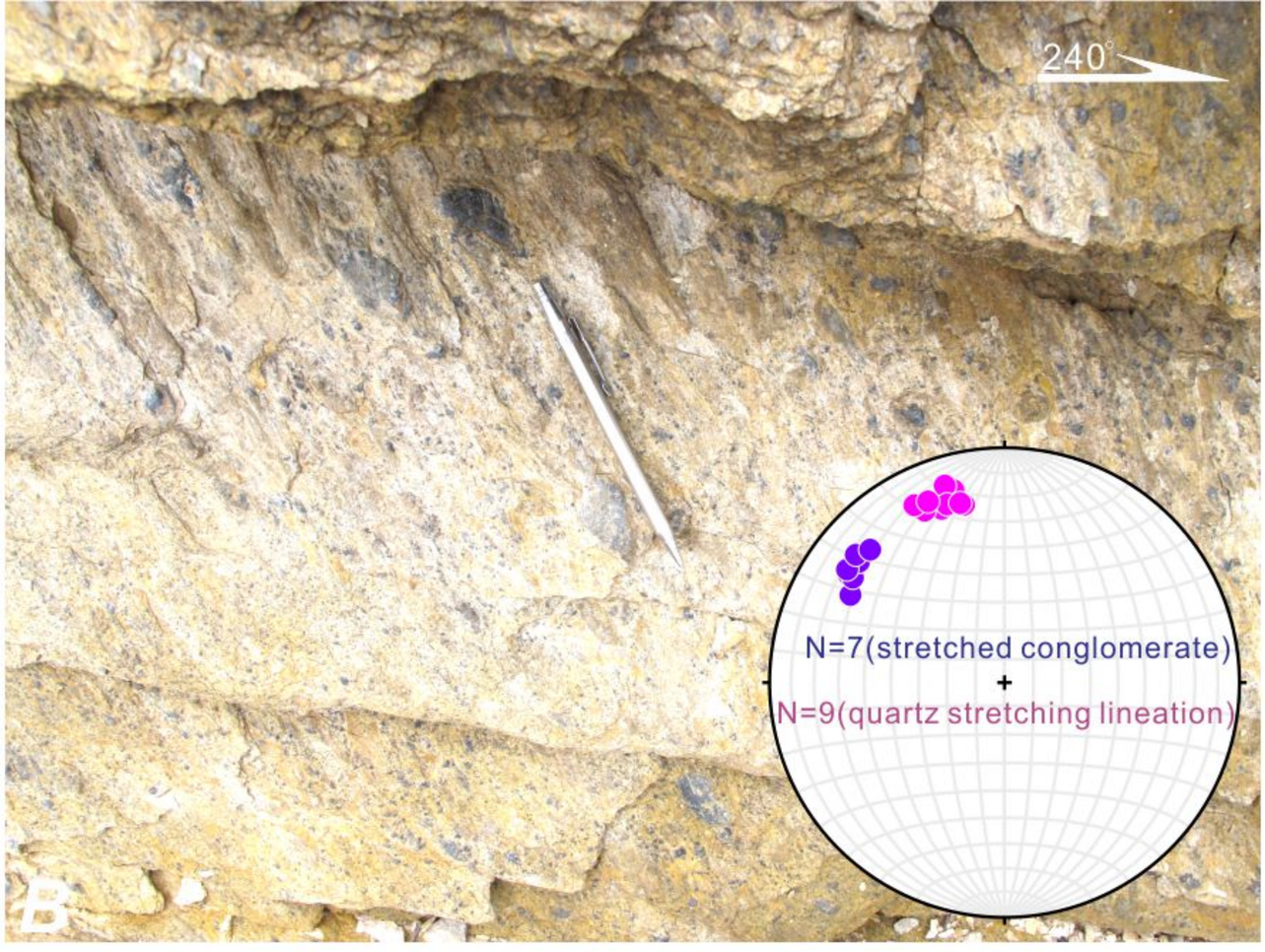
240°
N=7(stretched conglomerate)
N=9(quartz stretching lineation)
B


140°
2016/06/05 10:57
C


160°
D

Figure 11.

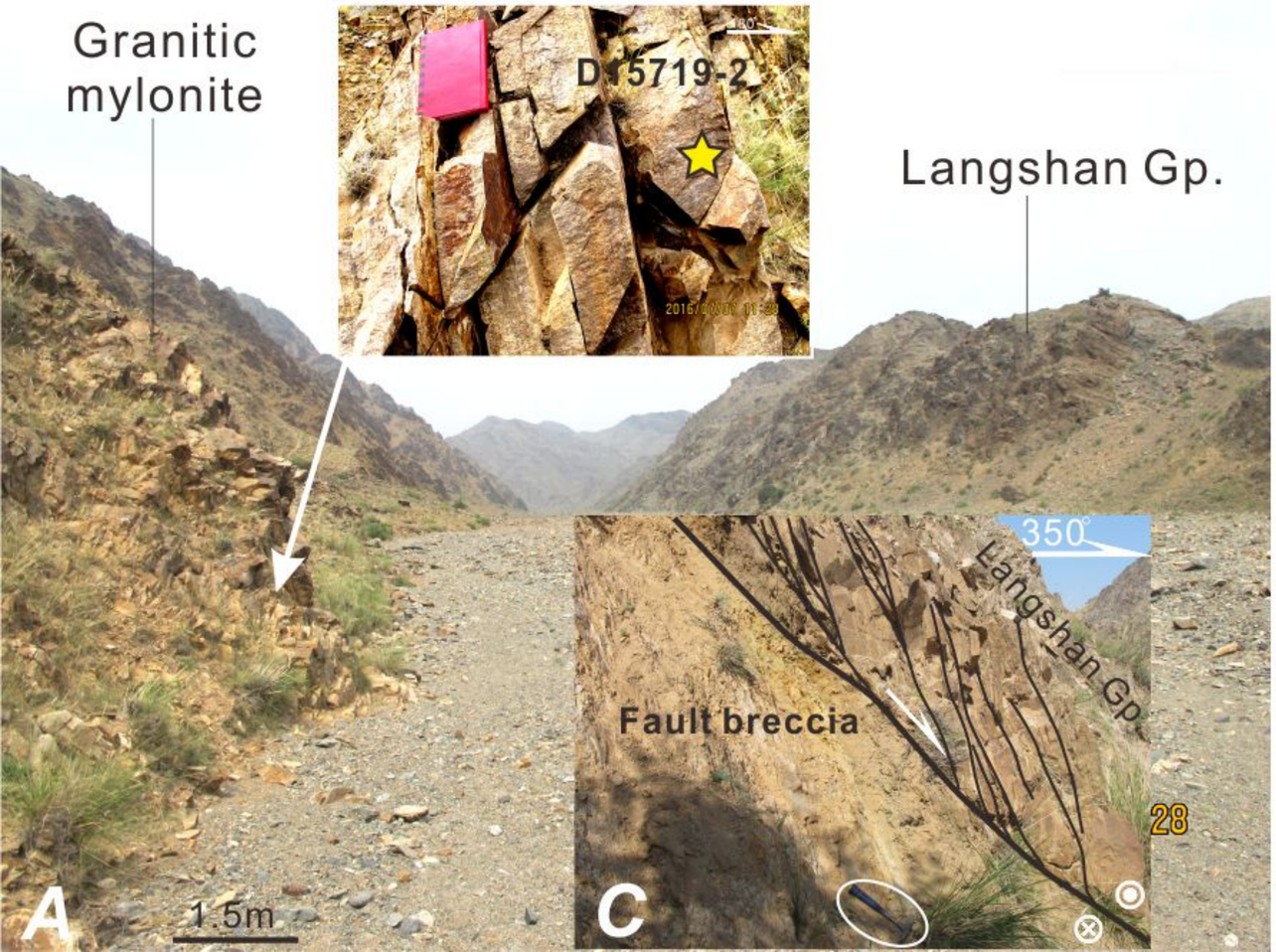
Granitic mylonite
D15719-2
Langshan Gp.
350°
Langshan Gp.
Fault breccia
28
A
1.5m
C

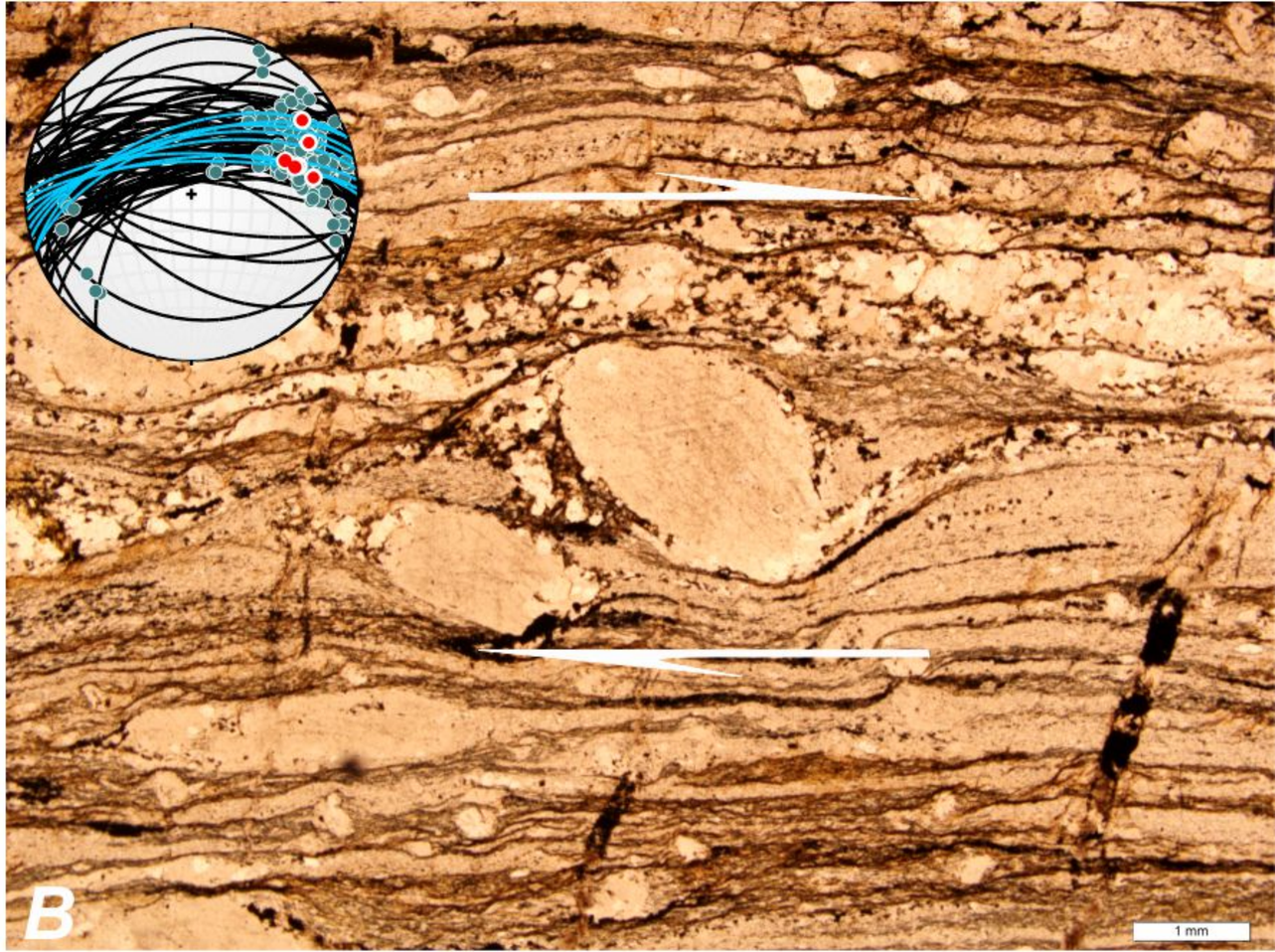
B
1 mm

Figure 12.

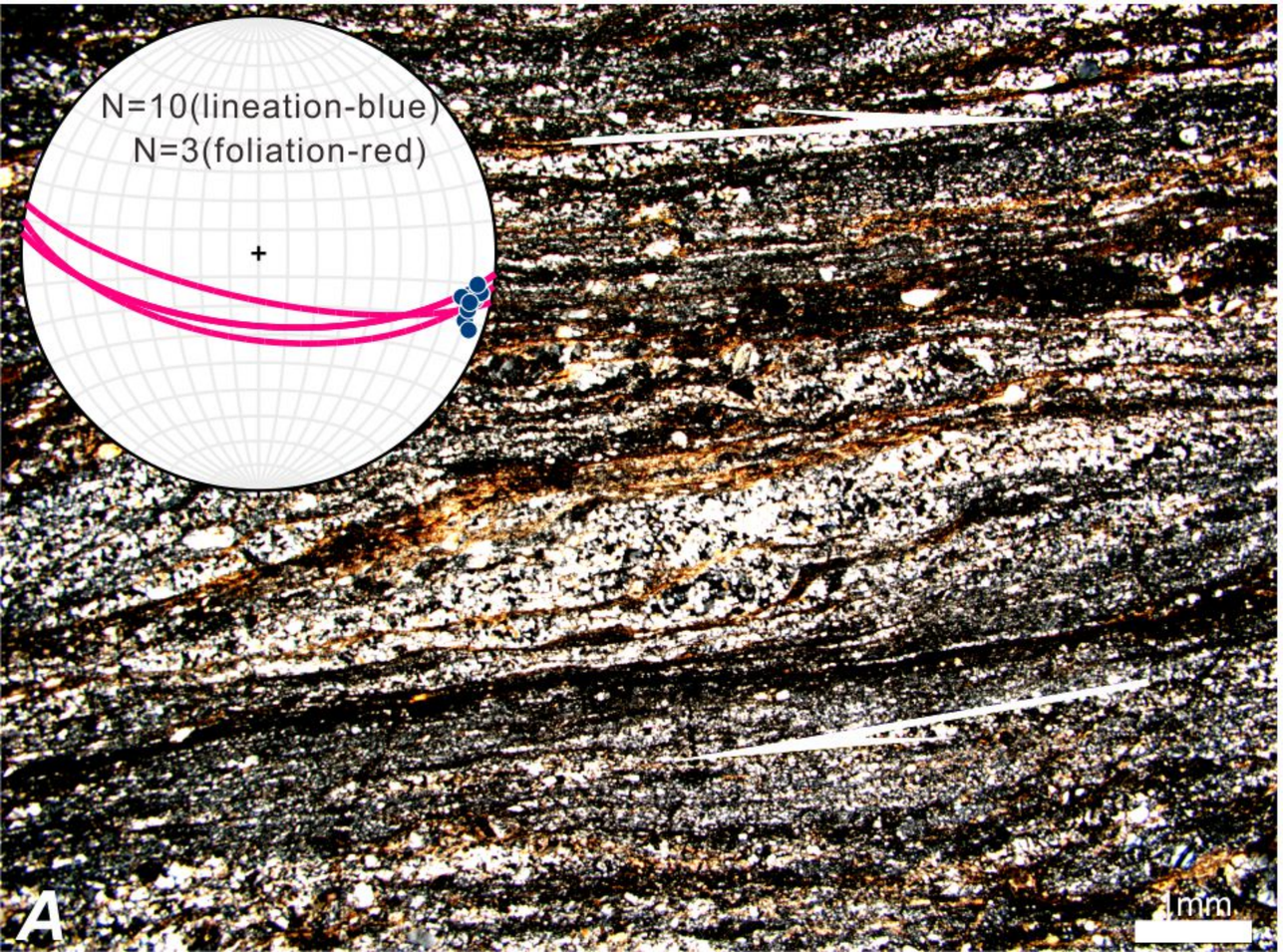
N=10(lineation-blue)
N=3(foliation-red)
1mm
A

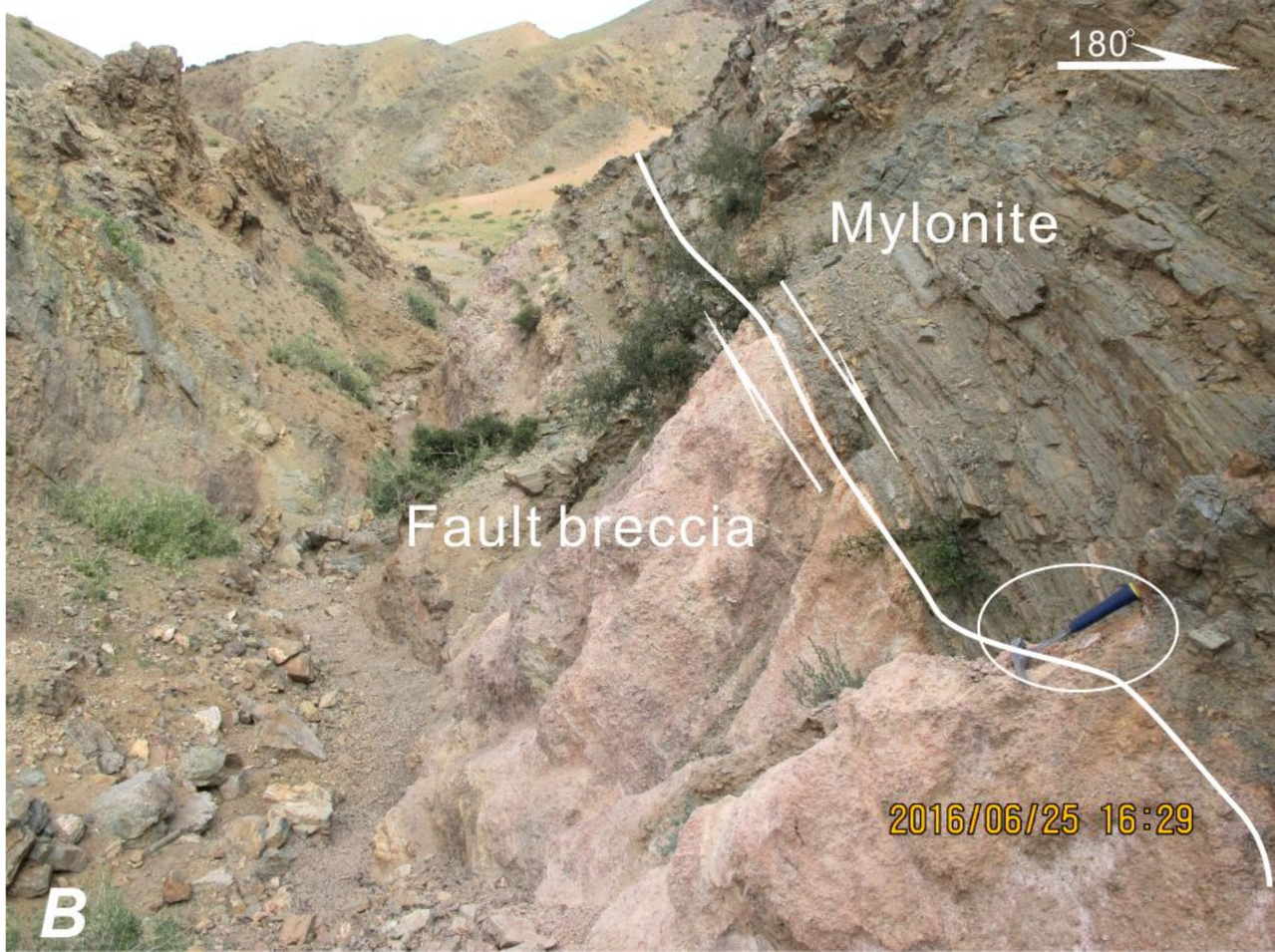
180°
Mylonite
Fault breccia
2016/06/25 16:29
B

Figure 13.

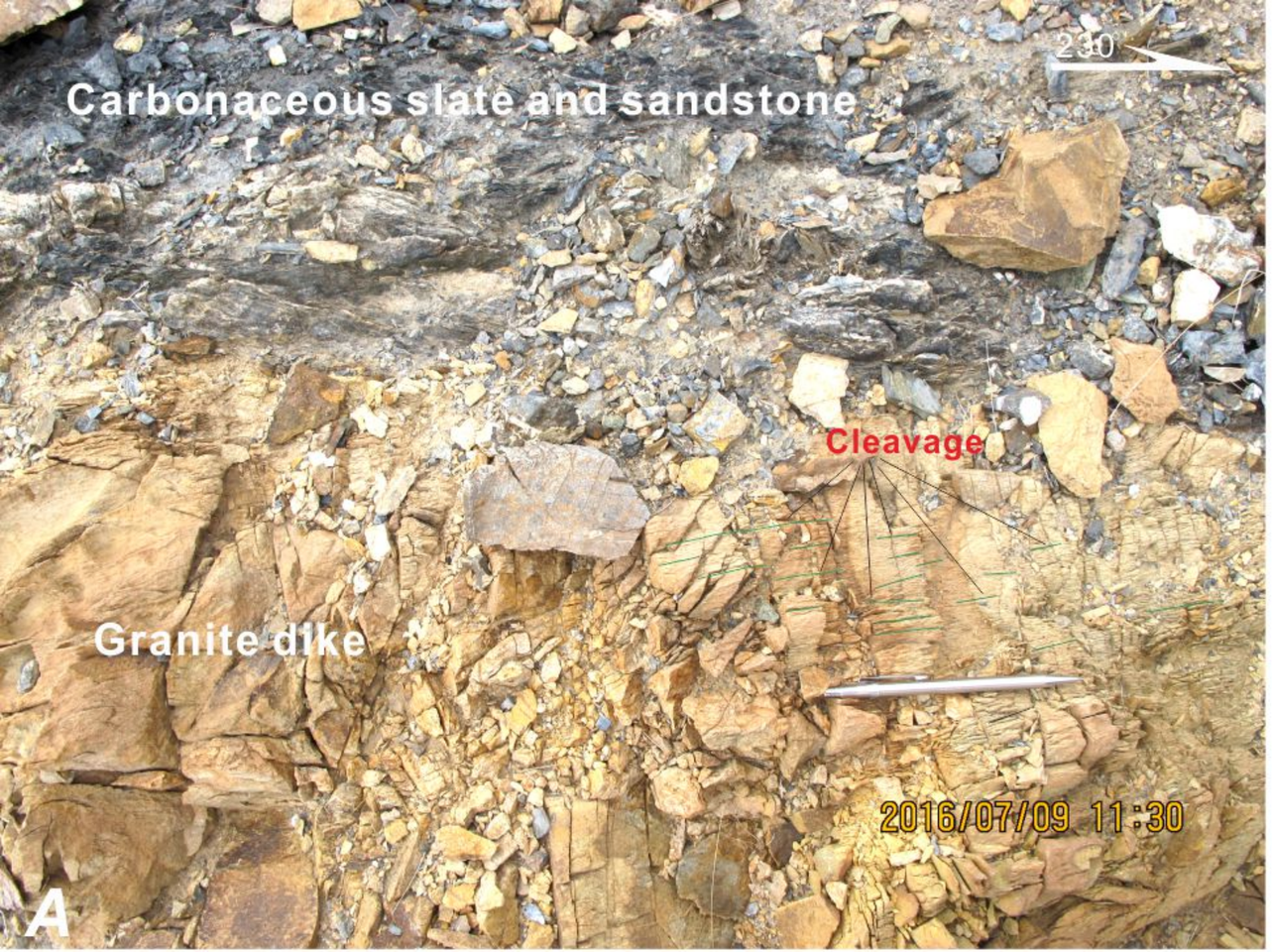
Carbonaceous slate and sandstone
Cleavage
Granite dike
2016/07/09 11:30
A


110°
Crenulation cleavage
Diorite dike
2016/08/14
B

Figure 14.

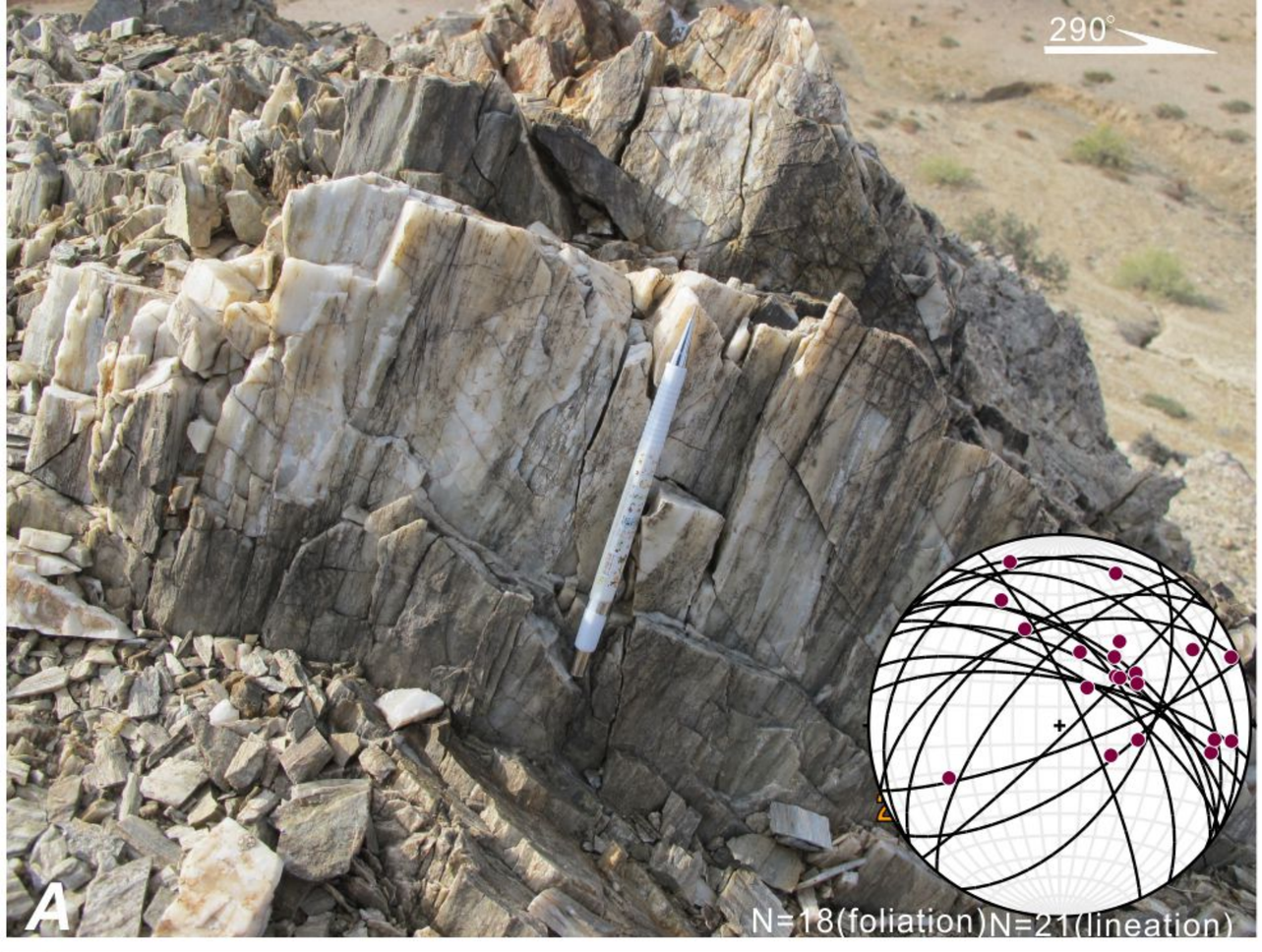
290°
N=18(foliation)N=21(lineation)
A

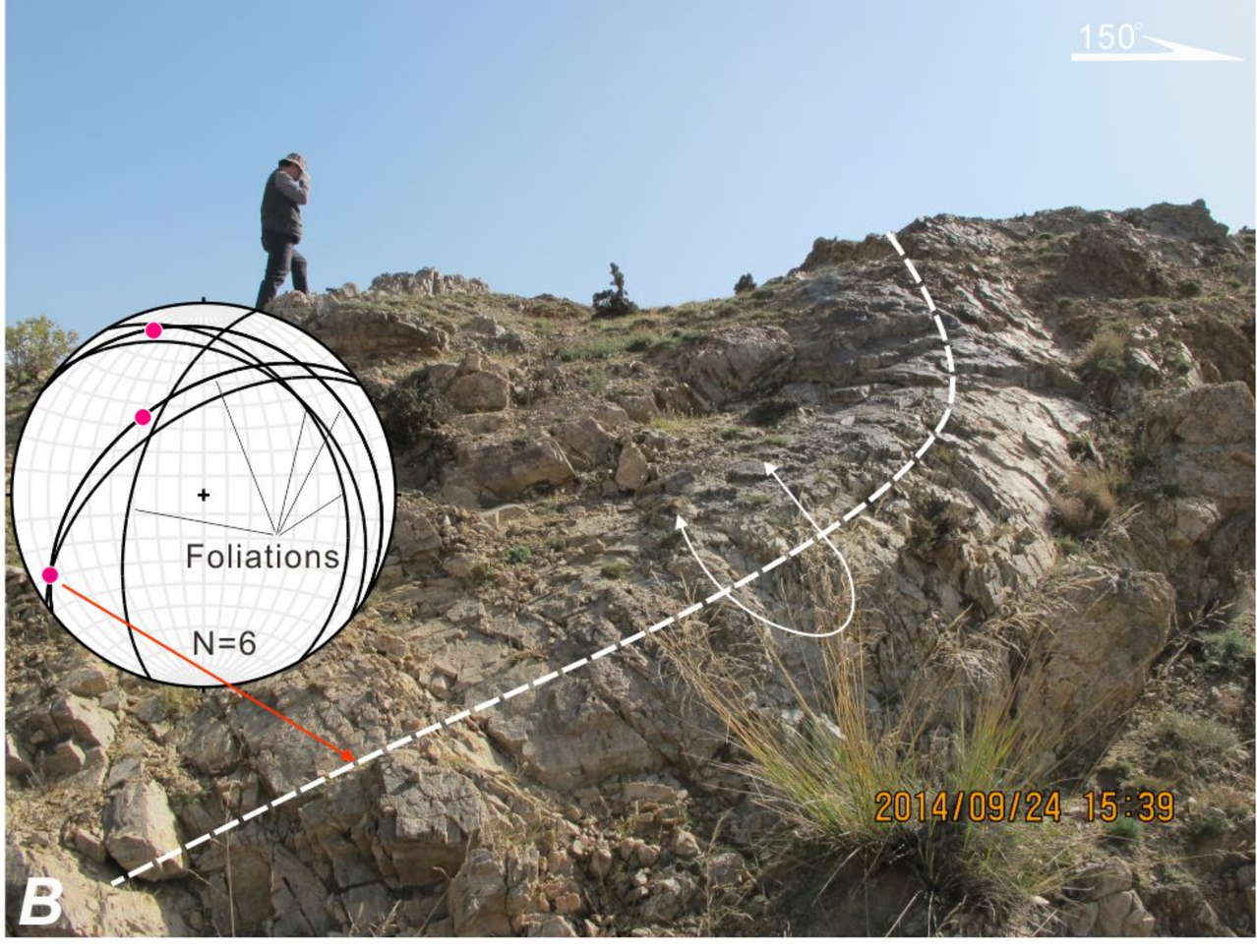
150°
Foliations
N=6
2014/09/24 15:39
B

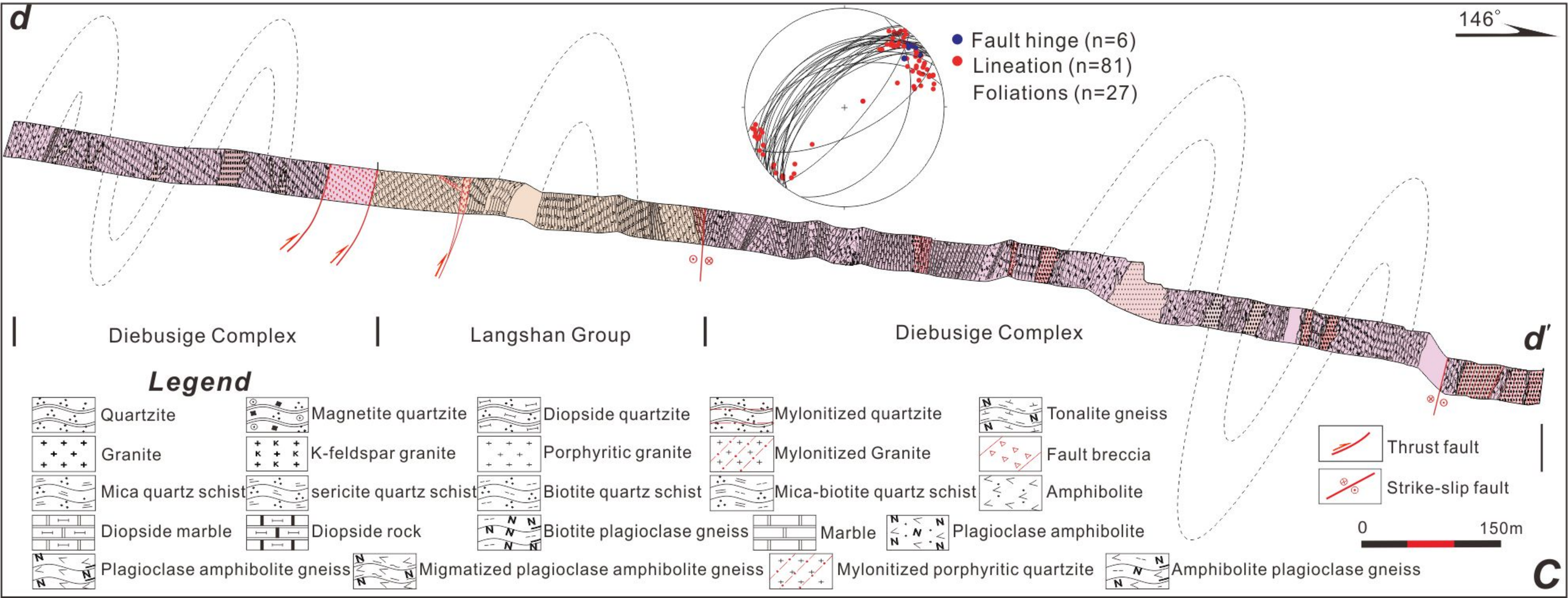
d
146°
Fault hinge (n=6)
Lineation (n=81)
Foliations (n=27)
Diebusige Complex
Langshan Group
Diebusige Complex
d'
Legend
Quartzite
Magnetite quartzite
Diopside quartzite
Mylonitized quartzite
Tonalite gneiss
Granite
K-feldspar granite
Porphyritic granite
Mylonitized Granite
Fault breccia
Mica quartz schist
sericite quartz schist
Biotite quartz schist
Mica-biotite quartz schist
Amphibolite
Diopside marble
Diopside rock
Biotite plagioclase gneiss
Marble
Plagioclase amphibolite
Plagioclase amphibolite gneiss
Migmatized plagioclase amphibolite gneiss
Mylonitized porphyritic quartzite
Amphibolite plagioclase gneiss
Thrust fault
Strike-slip fault
0
150m
C

Figure 15.

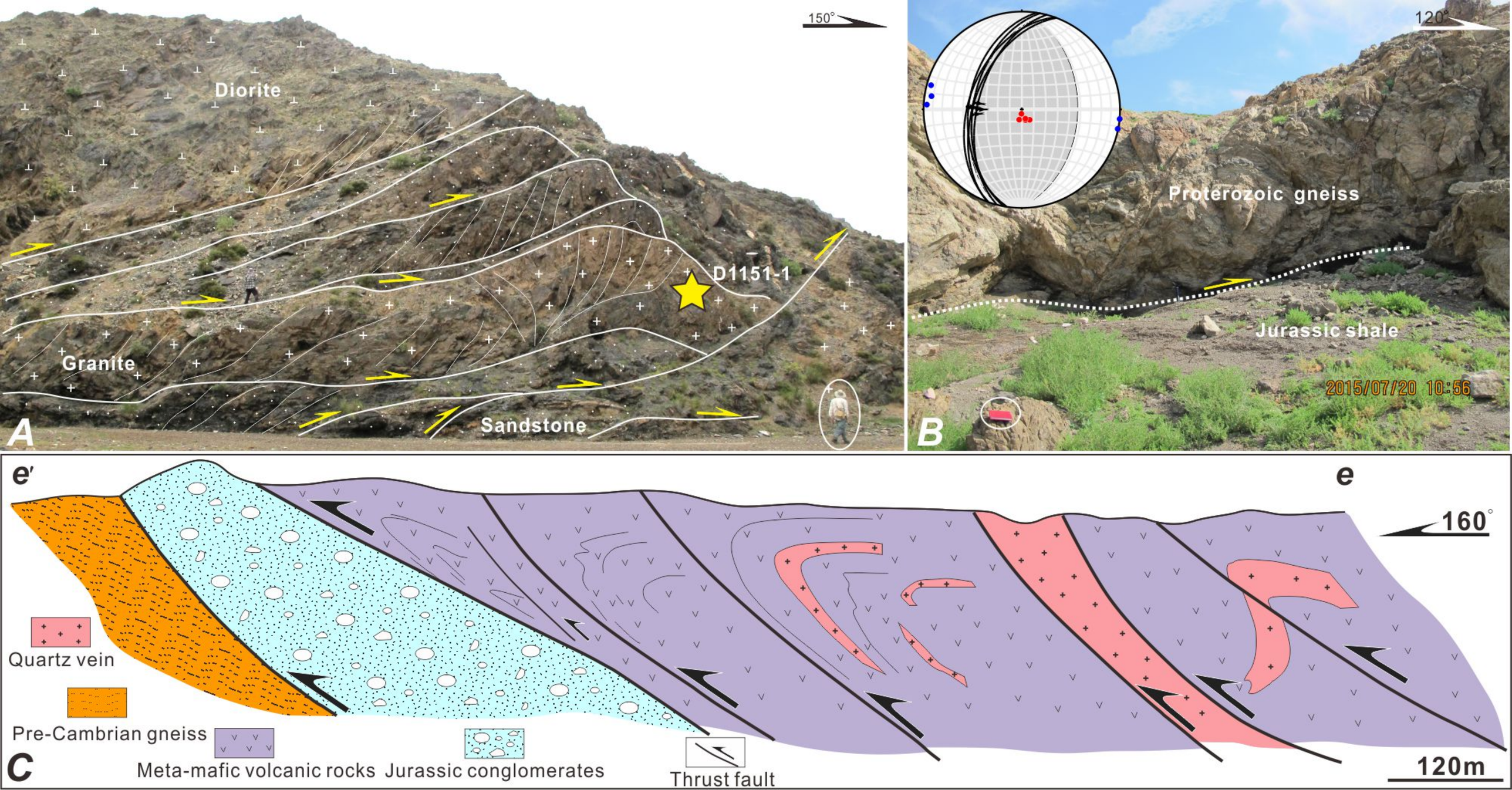
150°
Diorite
D1151-1
Granite
Sandstone
A
120°
Proterozoic gneiss
Jurassic shale
2015/07/20 10:56
B
e′
e
160°
Quartz vein
Pre-Cambrian gneiss
Meta-mafic volcanic rocks
Jurassic conglomerates
Thrust fault
C
120m

Figure 16.


310°
N
N=11
Lower Cretaceous conglomerate
Green fault breccia
Proterozoic gneiss
2015/07/18 18:06
A


126°
Oligocene
Oligocene
Bedding
Lower Cretaceous
Proterozoic gneiss
Oligocene
Proterozoic gneiss
B

Figure 17.


P-axis
T-axis
N=215
270°
Permian gabbro
Fault core
2015/08/08 11:29
60 cm
A
Permian granite
90
Permian granite
Fault core
201
N=215
B
85°
Bag
Early Cretaceous sandstone
Fault
C

Figure 18.

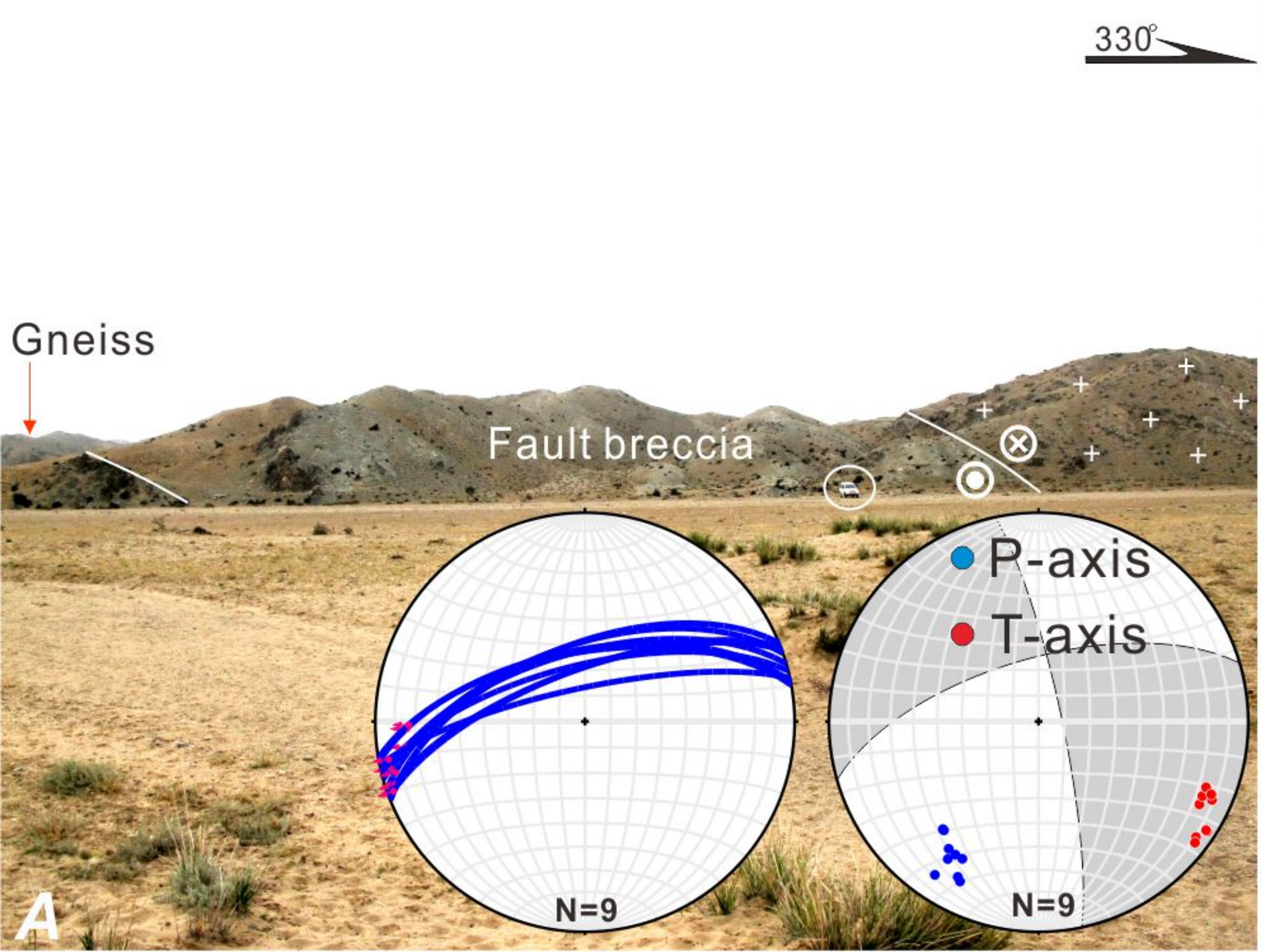
330°
Gneiss
Fault breccia
P-axis
T-axis
N=9
N=9
A

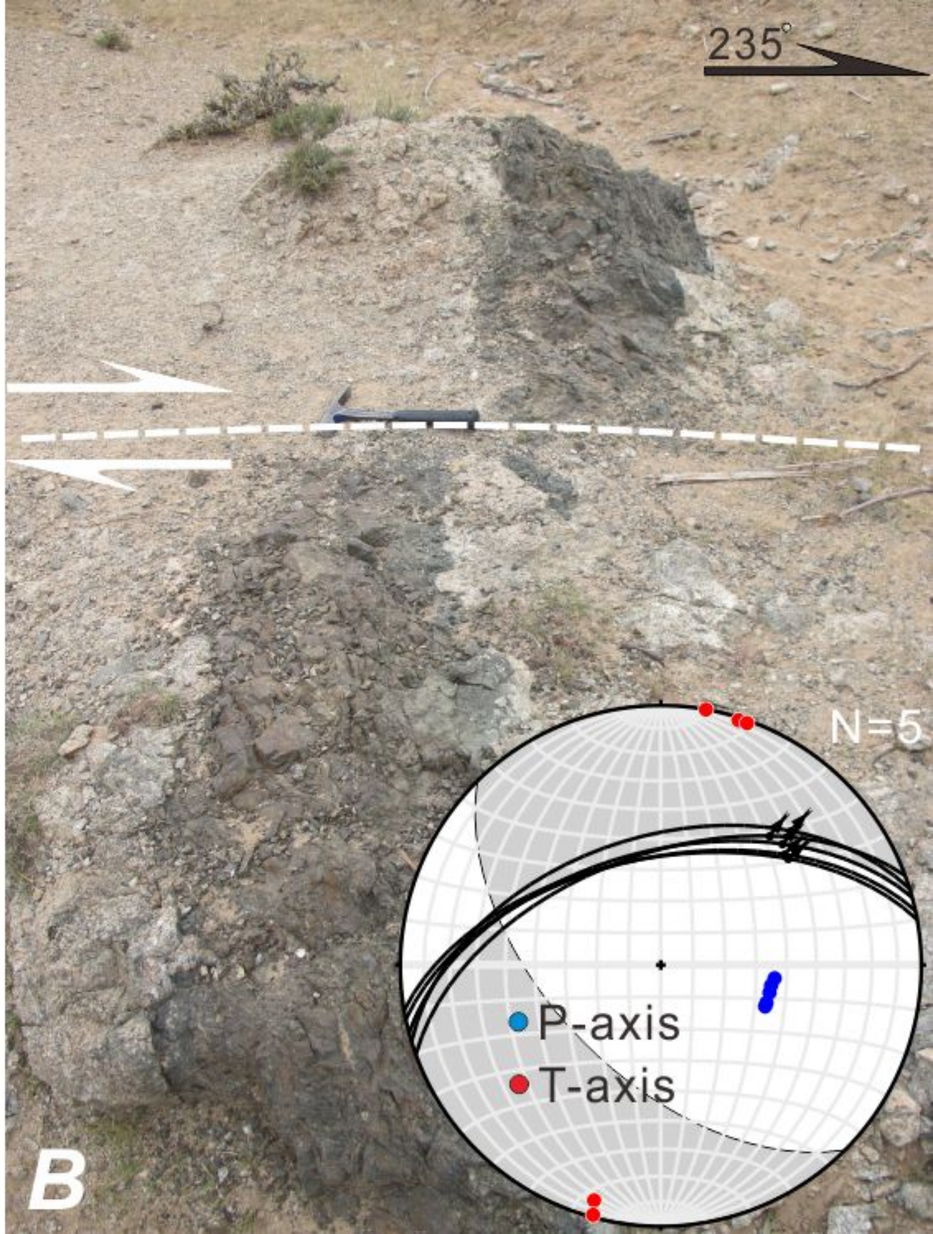
235°
N=5
P-axis
T-axis
B

Figure 19.

290°

Proterozoic gneiss

Proterozoic gneiss

Proterozoic gneiss

Oligocene sediments
(Wulanbulage Fm.)

2014/10/04 16:39

40 cm

A

230°

2014/10/04 17:16

B

300°

Bedding

Bedding

Lower Cretaceous

Lower Cretaceous
conglomerate

C

Figure 20.

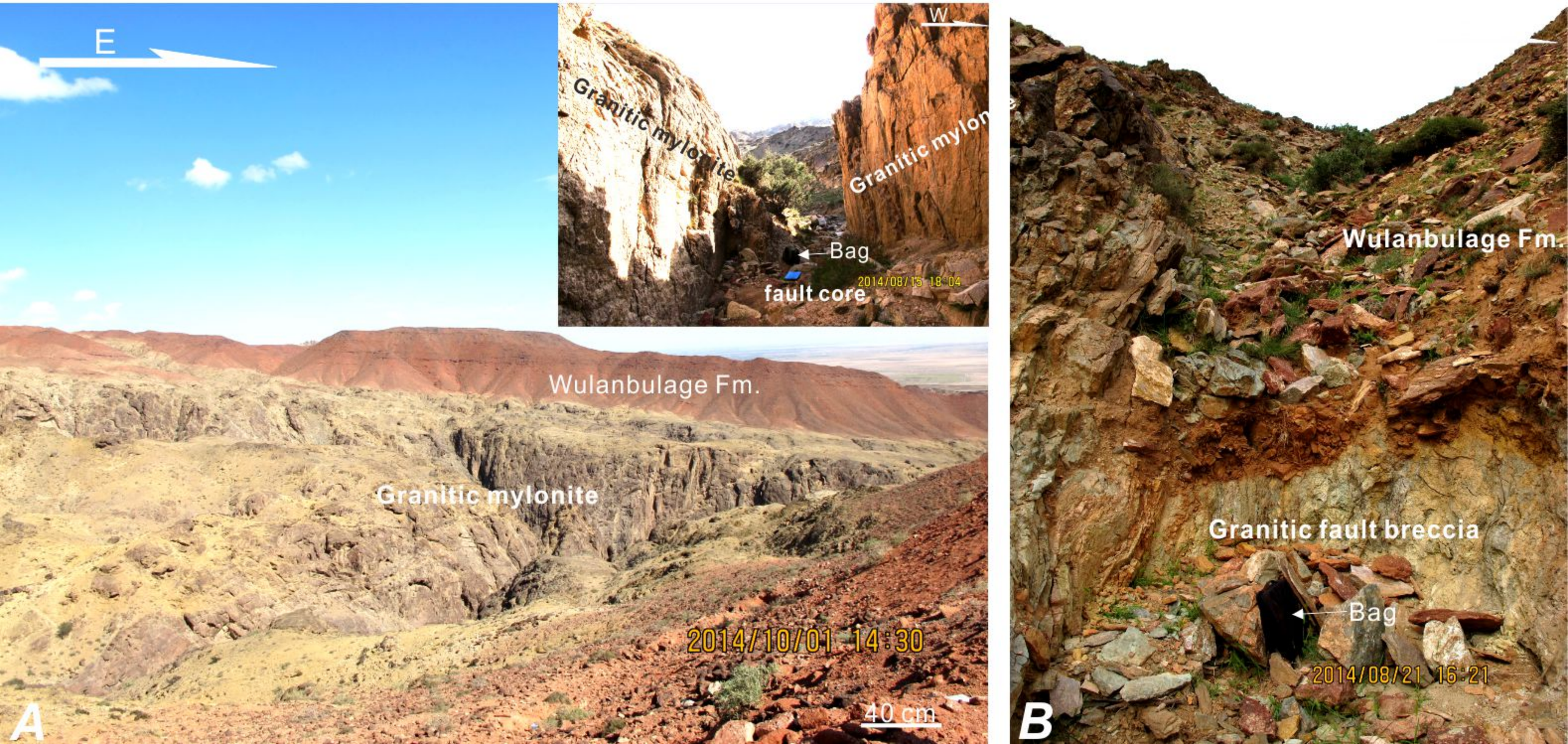
E
W
Granitic mylonite
Granitic mylon
Bag
fault core
2014/08/15 18:04
Wulanbulage Fm.
Granitic mylonite
2014/10/01 14:30
40 cm
A
Wulanbulage Fm.
Granitic fault breccia
Bag
2014/08/21 16:21
B

Figure 21.

120°

Wulanbulage Fm. (Oligocene)

Proterozoic gneiss

20

Figure 22.

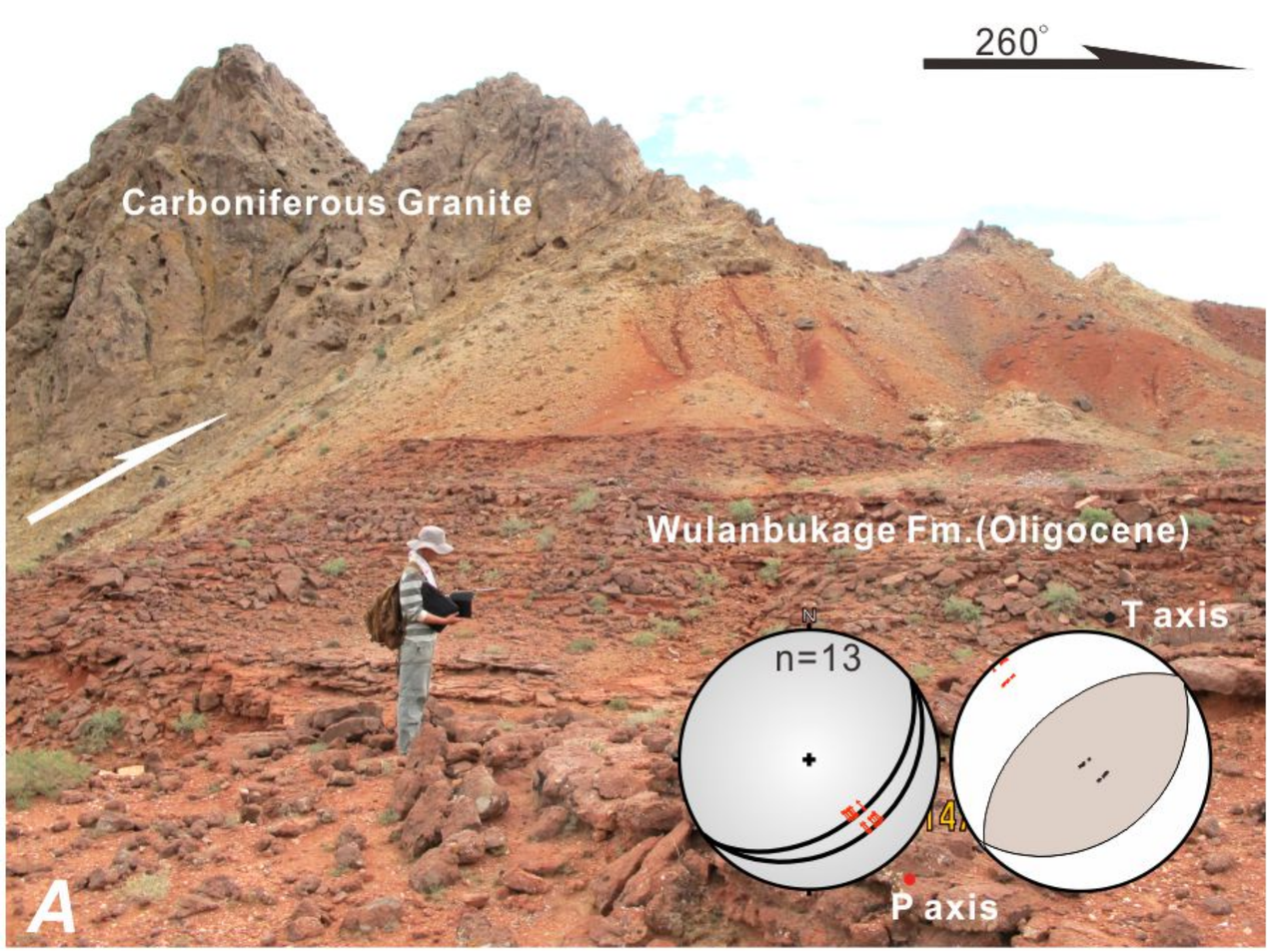
260°
Carboniferous Granite
Wulanbukage Fm.(Oligocene)
N
n=13
T axis
P axis
A

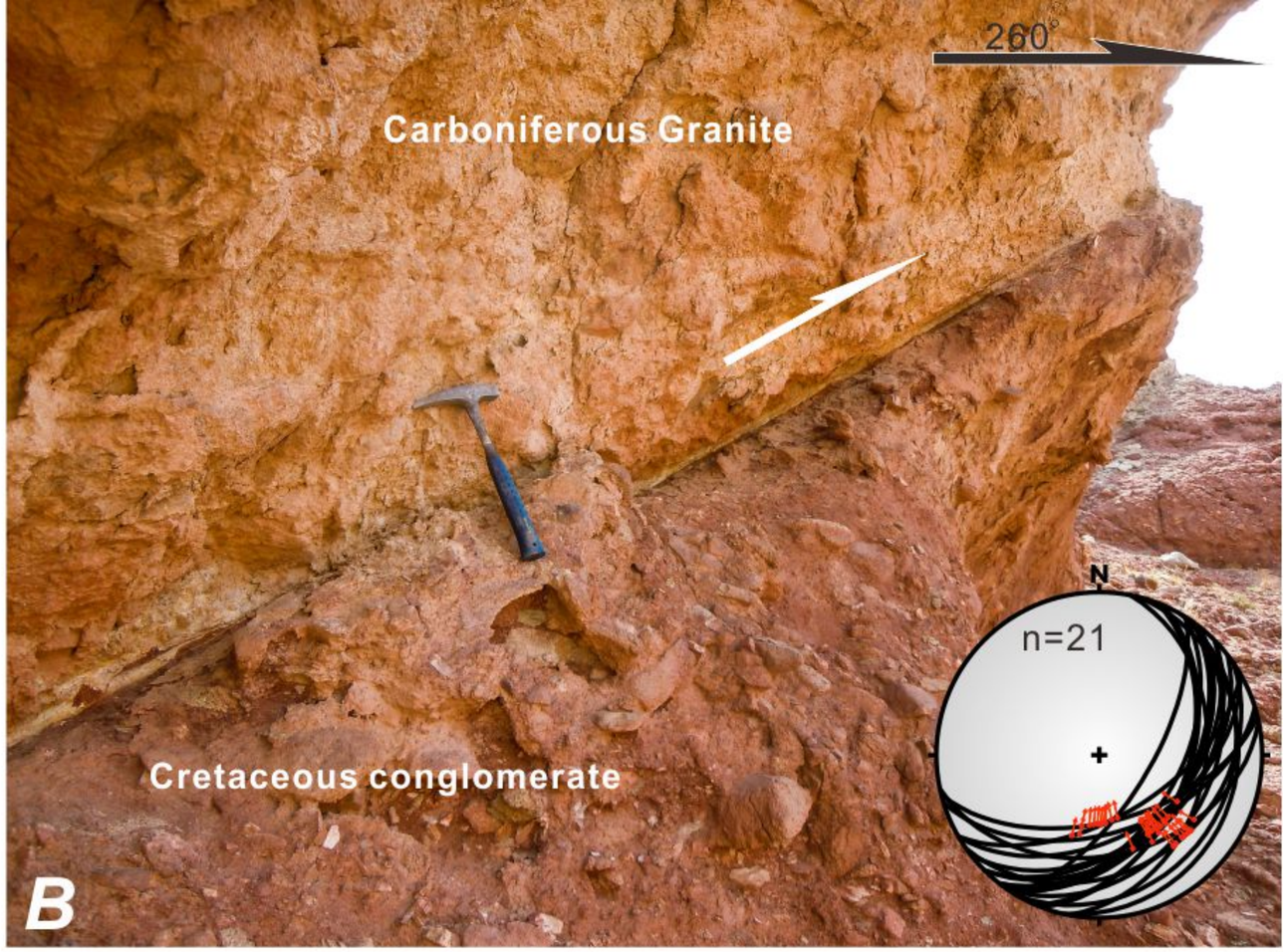
260°
Carboniferous Granite
Cretaceous conglomerate
N
n=21
B

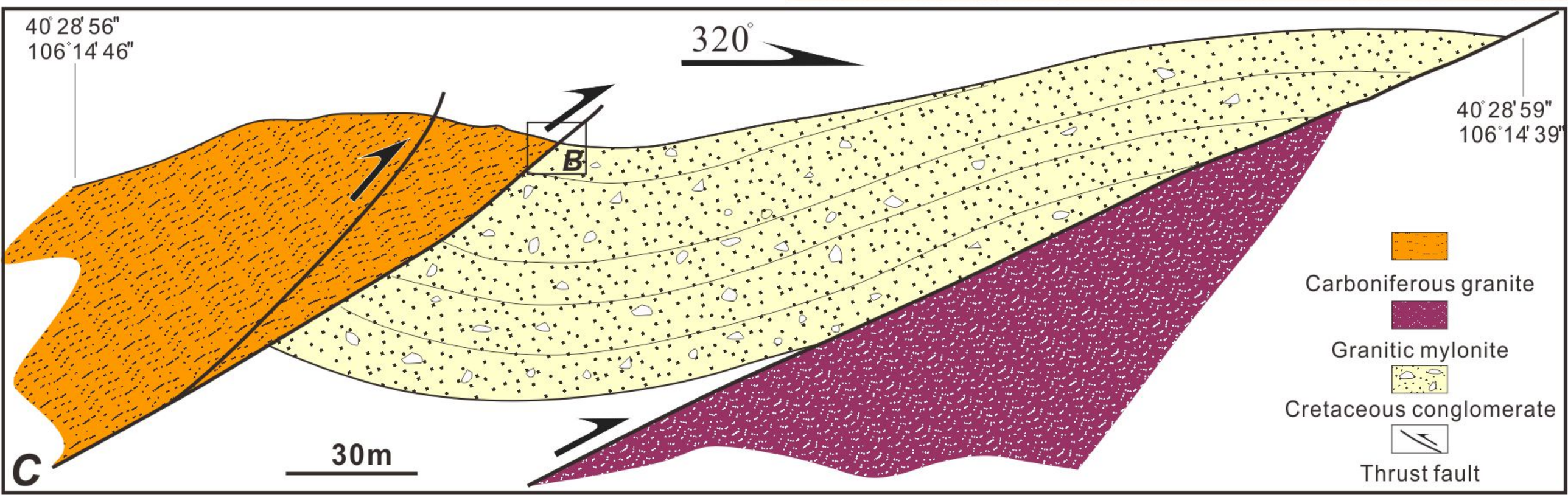
40° 28′ 56"
106° 14′ 46"
320°
B
40° 28′ 59"
106° 14′ 39"
30m
C
Carboniferous granite
Granitic mylonite
Cretaceous conglomerate
Thrust fault

Figure 23.

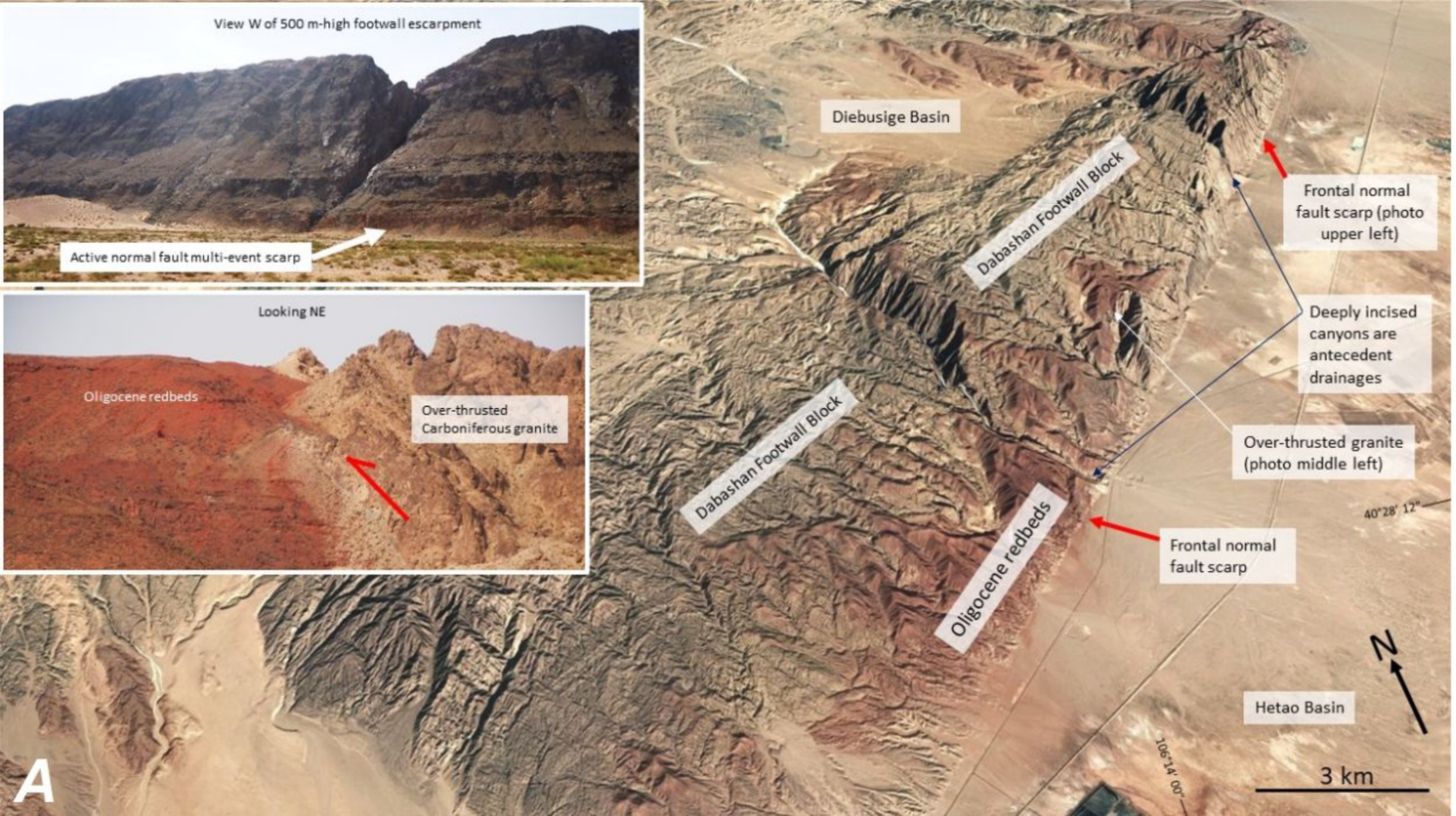
View W of 500 m-high footwall escarpment
Active normal fault multi-event scarp
Looking NE
Oligocene redbeds
Over-thrusted Carboniferous granite
Diebusige Basin
Dabashan Footwall Block
Dabashan Footwall Block
Oligocene redbeds
Frontal normal fault scarp (photo upper left)
Deeply incised canyons are antecedent drainages
Over-thrusted granite (photo middle left)
Frontal normal fault scarp
Hetao Basin
40°28' 12"
106°14' 00"
N
3 km
A

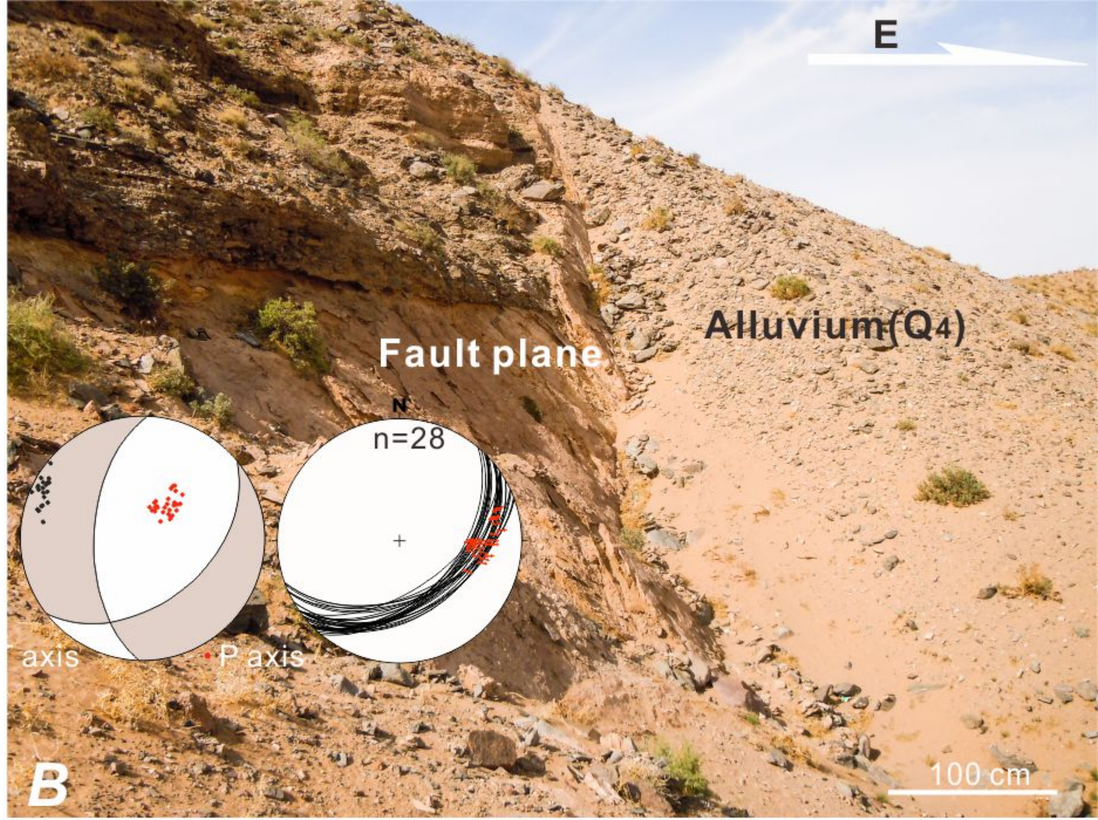
E
Fault plane
Alluvium(Q4)
N
n=28
axis
P axis
100 cm
B

Figure 24.

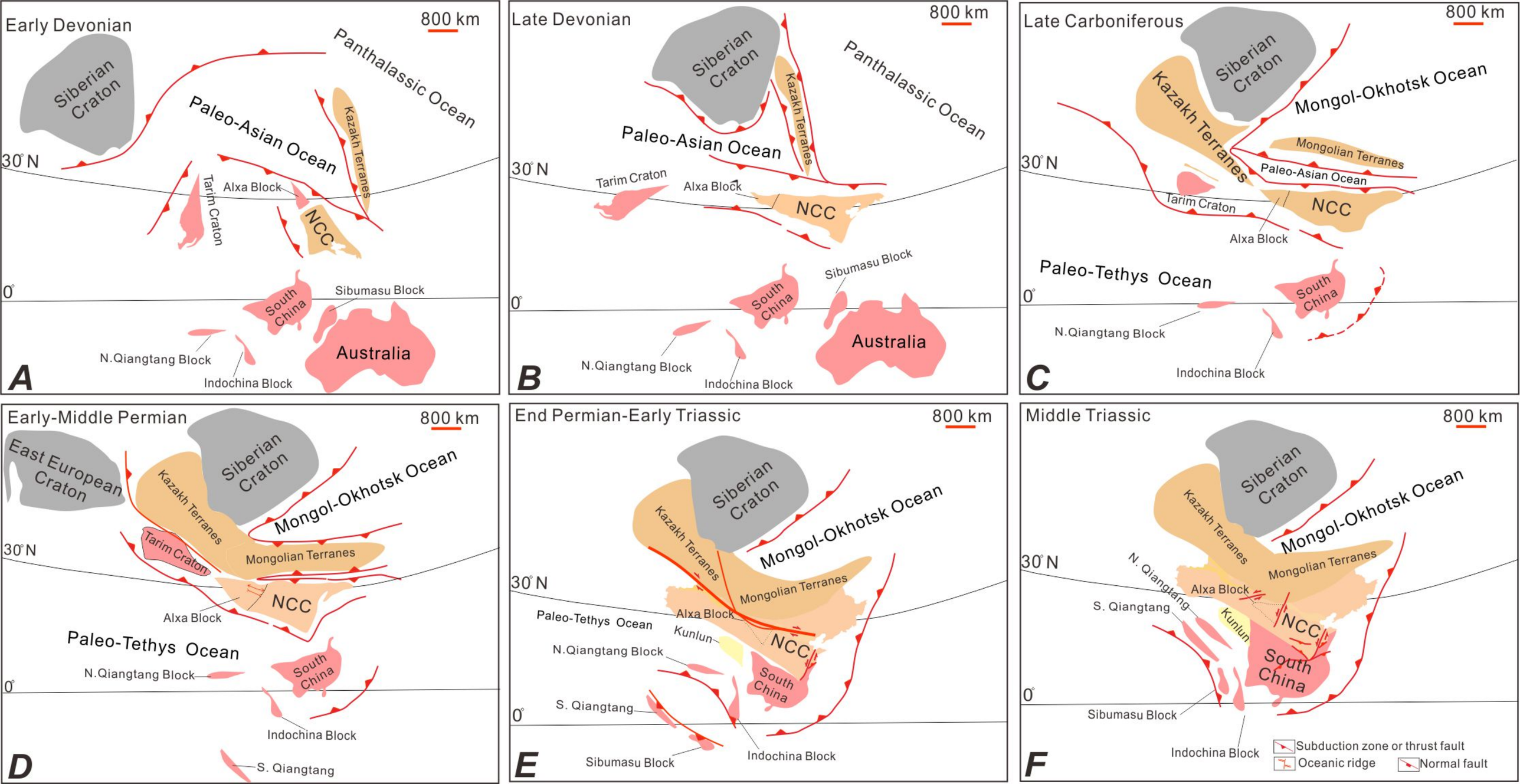
Early Devonian
800 km
Siberian Craton
Panthalassic Ocean
Paleo-Asian Ocean
Kazakh Terranes
30°N
Tarim Craton
Alxa Block
NCC
0°
South China
Sibumasu Block
Australia
N.Qiangtang Block
Indochina Block
A
Late Devonian
800 km
Siberian Craton
Kazakh Terranes
Panthalassic Ocean
Paleo-Asian Ocean
30°N
Tarim Craton
Alxa Block
NCC
Sibumasu Block
0°
South China
Australia
N.Qiangtang Block
Indochina Block
B
Late Carboniferous
800 km
Siberian Craton
Kazakh Terranes
Mongol-Okhotsk Ocean
Mongolian Terranes
Paleo-Asian Ocean
30°N
Tarim Craton
NCC
Alxa Block
Paleo-Tethys Ocean
0°
South China
N.Qiangtang Block
Indochina Block
C
Early-Middle Permian
800 km
East European Craton
Siberian Craton
Kazakh Terranes
Mongol-Okhotsk Ocean
Tarim Craton
Mongolian Terranes
30°N
NCC
Alxa Block
Paleo-Tethys Ocean
N.Qiangtang Block
South China
0°
Indochina Block
S. Qiangtang
D
End Permian-Early Triassic
800 km
Siberian Craton
Kazakh Terranes
Mongol-Okhotsk Ocean
Mongolian Terranes
30°N
Alxa Block
Paleo-Tethys Ocean
Kunlun
NCC
N.Qiangtang Block
South China
0°
S. Qiangtang
Sibumasu Block
Indochina Block
E
Middle Triassic
800 km
Siberian Craton
Kazakh Terranes
Mongol-Okhotsk Ocean
Mongolian Terranes
30°N
N. Qiangtang
Alxa Block
S. Qiangtang
Kunlun
NCC
South China
0°
Sibumasu Block
Indochina Block
Subduction zone or thrust fault
Oceanic ridge
Normal fault
F

Figure 25.

Late Jurassic

Siberia

Mongolia-Okhotsk suture

Tienshan

Tarim

Alxa

Ordos

Qaidam

Qinling

Sichuan

Lhasa block

South China

Neotethys

Indochina

Paleo-Pacific subduction

Thrust fault

Sedimentary basin

Luliangshan

Taihangshan

Helanshan

E

Ordos basin

0km

Crust

100

Lithosphere

200

Paleo-Pacific Plate

A

Early Cretaceous

Siberia

Songneng basin

Tienshan

Tarim

Alxa

Ordos

Qaidam

Qiangtang

Qinling

Sichuan

Lhasa block

South China

Neotethys

Indochina

Paleo-Pacific subduction

Normal fault

Volcanic rocks

Sedimentary basin

Metamorphic core complex

Luliangshan

Taihangshan

Helanshan

E

Ordos basin

North China basin

0km

Crust

100

Lithosphere

200

Asthenosphere

Paleo-Pacific Plate

B

Late Cretaceous

Siberia

Songneng basin

Tienshan

Tarim

Alxa

Ordos

Qaidam

Qiangtang

Qinling

Lhasa block

South China

Neotethys

India

Indochina

Palawan Block

Paleo-Pacific subduction

Alxa Block

Ordos Block

Sinistral strike-slip fault

C

Paleogene (ca.60-40Ma)

Siberia

Tienshan

Tarim

Alxa

Ordos

Qaidam

Qiangtang

Qinling

Lhasa block

South China

India

Indochina

Alxa Block

Ordos Block

Dextral strike-slip fault

Sedimentary basin

D

Table 1 LA-ICP-MS zircon U-Pb analytical results for the samples

Sample	Coordinate	Sample location	lithology	Age (mineral, method)	Nature of age	Domain
LS-16-3	40°38′17.48″, 106°15′1.61″	Intruding limestone in the Second Fm. of the Langshan Gp.	granite	258.3±1.6 Ma (zircon, LA-ICP-MS)	protolith	I
D1148-1	40°38′10.11″, 106°12′13.26″	Bedding-parallel intruding the Third Fm. of the Langshan Gp.	Blue medium grained diorite	840±8 Ma (zircon, LA-ICP-MS)	protolith	
D15719-2	40°39′7.09″, 106°17′6.48″	Boundary between the granite and the Third Fm. of the Langshan Gp.	granitic mylonite	258.9±1.3 Ma (zircon, LA-ICP-MS)	Protolith	
D15109-1	40°38′25.53″, 106°15′19.38″	Intruding the Langshan Group (the Third Fm.)	boudinaged diorite	257.6±1.1 Ma (zircon, LA-ICP-MS)	protolith	
D15090-1	40°37′21.36″, 106°16′33.08″	diorite	diorite	263.7±1.9 Ma (zircon, LA-ICP-MS)	protolith	II
D15040-1	40°36′13.22″, 106°16′12.28″	Intruding the Langshan Group	Folded granite intruding along the bedding of the Langshan Group	259.4±1.3 Ma (zircon, LA-ICP-MS)	protolith	
D15729-1	40°38′20.43″, 106°18′18.40″	Permian granite	Permian granite	272.2±2.3 Ma (zircon, LA-ICP-MS)	protolith	
LS-14-3	40°34′2.37″, 106°11′36.69″	Intruding the Diebusige Complex	K-feldspar granite	1834±17 Ma (zircon, LA-ICP-MS)	protolith	III
D15739-1	40°37′6.30″, 106°20′23.86″	Permian granite	Permian granite	259.6±1.3 Ma (zircon, LA-ICP-MS)	protolith	
LS-14-1	40°28′57.20″, 106°14′45.10″	granite	granite	344.7±1.2 Ma (zircon, LA-ICP-MS)	protolith	IV

Table 2 Main structures, tectonic events, ages and tectonic settings of different domains in the Langshan region

Tectonic stage	Domain I	Domain II	Domain III	Domain IV	Main structure	age	Tectonic setting
D1	**DI-1**				Nearly east-west-striking, ductile sinistral strike-slip shear zone (after structural reconstruction)	Late Devonian (ca.350 Ma)	Interaction between blocks in Paleo-Asian Ocean and the Alxa Block
D2	**DI-2**	**DII-1**	**DIII-1**		Nearly east-west-striking, top-to-the-south thrust and Isoclinal folds (after structural reconstruction)	Late Permian (ca.270-250 Ma)	Closure of the Paleo-Asian Ocean
D3	**DI-3**	**DII-2**	**DIII-2**		east-west-trending ductile dextral shearing	End Permian-Early Triassic (ca. 250 - 230 Ma)	Eastern extrusion of the Yili Block and Junggar Basin in the western CAOB
D4	**DI-4**		**DIII-3**	**DIV-1**	Northeast-southwest-trending ductile sinistral shearing, northwest-southeast-striking folds in the Langshan Group	Mid-Late Triassic (ca. 210 Ma)	Collision between the North China and the Yangtze cratons
D5	**DI-5**	**DII-3**	**DIII-4**		Top-to-the-southeast thrust and related folds; east-west-trending brittle dextral shearing	Late Jurassic	(1) subduction of the Paleo-Pacific Ocean? (2) collision between the Qiangtang and Lhasa blocks? (3) closure of the Mongol-Okhotsk Ocean?
D6			**DIII-5**		Low-angle detachment fault	Early Cretaceous	Regional extension across eastern Asia, and/or retreating subduction of the Paleo-Pacific Ocean?
D7	**DI-6**	**DII-4**	**DIII-6**	**DIV-2**	Northeast-southwest-trending sinistral strike-slip faults; nearly south-north-trending	Late Cretaceous	East Asian margin and Western Philippine Block convergence?

					sinistral strike-slip faults		
D8		**DII-5**	**DIII-7**	**DIV-3**	Northeast-southwest-trending dextral strike-slip faults	Paleogene (ca.60-40 Ma)	Collision between the Indian and Eurasian plates
D9			**DIII-8**	**DIV-4**	Top-to-the-northwest thrusts	Miocene (ca. 25 Ma)	Compression between the Indian and Eurasian plates and eastward displacement of Alxa Block
D10			**DIII-9**	**DIV-5**	Active high angle normal faults	Neogene	Compression between the Indian and Eurasian plates